The Pennsylvania State University

The Graduate School

SOLID-STATE NANOPORE CRISPR-ASSISTED DIAGNOSTIC SYSTEMS TOWARD DIGITAL NUCLEIC ACID TESTING

A Dissertation in

Electrical Engineering

by

Reza Nouri

Submitted in Partial Fulfillment
of the Requirements
for the Degree of
Doctor of Philosophy

May 2023

The dissertation of Reza Nouri was reviewed and approved by the following:

Weihua Guan

Associate Professor of Electrical Engineering

Dissertation Advisor

Chair of Committee

Aida Ebrahimi

Assistant Professor of Electrical Engineering

Shengxi Huang

Assistant Professor of Electrical Engineering

Xiaojun Lance Lian

Associate Professor of Biomedical Engineering

Thomas La Porta

Professor of Computer Science and Engineering and Electrical Engineering

Head of the Department of Electrical Engineering and Computer Science

ABSTRACT

Whether caring for an individual patient with an infectious disease or responding to a worldwide pandemic, the accurate diagnosis of a pathogen is fundamental to quality care. While different techniques, such as enzyme-linked immunosorbent assay and cell culture, have been introduced for diagnostics, Nucleic Acid Test (NAT) is the most sensitive and specific method. In the majority of NAT systems, an amplification step is utilized for detecting the target RNA or DNA in a sample. In the conventional amplification-based NAT quantification method, the absolute concentration of target templates remains unknown until calibrated with standard samples. However, utilizing digital assays where samples are partitioned into numerous and separated reaction chambers provides a platform for calibration-free quantification of targets in a sample. Therefore, exploring digital diagnostic platforms is strongly needed to optimize clinical care and guide infection control to limit disease spread.

This thesis mainly focuses on exploring the digital quantification of target nucleic acids using solid-state nanopores and CRISPR towards rapid, label-free nucleic acid testing. We studied the experiment-relevant parameters and their effects on molecular transport dynamics through the nanopore, which would help us to design an experimental setup with higher throughput and accuracy. We further developed a calibration-free model for concentration estimation to address the pore-to-pore variations issues of nanopores. Afterward, we combined the high specificity offered by the CRISPR Cas technology and the high sensitivity offered by the nanopore sensor towards an electronic sensing platform for sequence-specific HIV-1 and SARS-COV-2 detection.

Furthermore, we developed a quantitative CRISPR sensing figure of merit and explored performance improvement strategies to improve CRISPR diagnostic systems. Based on our model

which was validated by 57 existing CRISPR systems, digitalization was the most promising amplification-free method for achieving comparable performances. Therefore, we finally developed a self-digitalization through an automated membrane-based partitioning technique to digitalize the CRISPR-Cas13 assay for amplification-free and absolute quantification of HIV-1 viral RNAs. The results showed that the samples spanning 4 orders of dynamic range between 100 aM to 1 pM could be quantified using our system. We also obtain the limit of detection 100 aM within 30 min of reaction. We envision that the nanopore-based and digital CRISPR platform provided in this work will provide accurate, sensitive, and specific diagnostic systems for different types of pathogens.

TABLE OF CONTENTS

LIST OF FIGURES

LIST OF TABLES

ACKNOWLEDGEMENTS

First and foremost, I am extremely grateful to my supervisor, Professor Weihua Guan. for his invaluable advice, continuous support, and patience during my Ph.D. study. His immense knowledge and plentiful experience have encouraged me throughout my academic research and daily life. Working with him was a great honor, and I am incredibly thankful for what he has offered me.

For this dissertation, I would like to thank my defense committee members: Prof. Aida Ebrahimi, Prof. Shengxi Huang, and Prof. Xiaojun Lance Lian, for their time, guidance, and constructive comments. I would like to thank all my lab members. Their kind help and support have made my study and life in the USA a wonderful time.

The work presented in this dissertation was partly supported by the National Institutes of Health (NIH) under Grant R6AI147419 and National Science Foundation (NSF) under grants No. 1902503, 1912410 and 1710831. The views and opinions of the author expressed herein do not state or reflect those of federal funding and shall not be used for advertising or product endorsement purposes.

Finally, I am incredibly grateful to my parents. Even though I didn't see them in the past 4 years, I always felt them in my heart. Without them, this day would not have been possible.

Reza Nouri

CHAPTER 1 INTRODUCTION AND OVERVIEW

1.1. Background

Unlike other conventional diseases, infectious disease is a kind of disease caused by live pathogens such as bacteria, viruses, and parasites, which is capable of rapid transmission and infection among human or animal vectors by inoculation, airborne or waterborne transmission [1]. Infectious diseases have for centuries ranked with wars and famine as major challenges to human progress and survival [2]. Noteworthy examples of the latest infectious diseases outbreaks include ongoing pandemics COVID-19 [3] and HIV [4], Ebola (2013- 2015), Zika virus (2013-2015), H1N1 Influenza (2009-2010), MERS (2007) [5], and other ongoing challenges including respiratory diseases (Tuberculosis, Measles, etc.), diarrheal diseases (Rotavirus, E. coli, etc.), mosquito-borne pathogens (Malaria, West Nile Virus, etc.). Whether caring for an individual patient with an infectious disease or responding to a worldwide pandemic, the accurate diagnostic of a microbial cause is fundamental to quality care [6]. In case of an outbreak, rapid, reliable, and accessible testing is required for effective containment of the disease [7].

Infectious disease diagnostics can be achieved by indirect or direct techniques. In indirect techniques such as enzyme-linked immunosorbent assay (ELISA) [8], antibodies developed by the patients would be detected. On the other hand, the pathogens could be detected directly by observing the pathogen nucleic acids or the antigens from the pathogen. Some examples of direct diagnostics are cell culture [9], lateral-flow immunoassay (LFA) [10], and nucleic acid testing (NAT) [11]. One of the earliest developed diagnostic techniques is cell culture which requires well-equipped laboratories and long incubation times of up to days, which is not suitable for fast

response. ELISA has rapidly found various applications in food quality, environmental, biotechnological, and chemical disciplines, among others. In spite of its many advantages, ELISA has certain limitations such as tedious/laborious assay procedure, and non-specific protein adsorption, which leads to low specificity [12]. Among these approaches, NAT is perhaps the most powerful method due to its relatively short time to result, high sensitivity, and specificity. For many pathogens, NAT is the preferred gold-standard testing method [13].

In NAT techniques, usually a molecular amplification method such as Polymerase Chain Reaction (PCR) is utilized for detecting the target RNA or DNA in the sample. If the pathogen is present, many DNA copies will be generated. The amplified DNAs are typically detected by an optical method. Conventional real-time PCR (qPCR) based on quantification cycles (Cq) is a relative quantification method, and the absolute concentration of target templates remains unknown until calibrated with standard samples [14].

In contrast to qPCR, samples for digital assay quantification are first partitioned into numerous and separated reaction chambers [15]. Each chamber may contain one or more than one (positive chamber) and no target molecule (negative chamber). This “digital format” eliminates the kinetic variations of molecular amplification rates, therefore enabling precise, ultrasensitive, and rapid counting of target molecules [16]. Meanwhile, digital assays also reduce device complexity since only end-point readout is required [17].

So far, various digitalization techniques have been introduced. For instance, water in oil droplets generated by T-junction [18], flow focusing [19, 20], and centrifugation [21] have been used for digitalization. Furthermore, digital assays have been performed inside numerous microchambers fabricated by polydimethylsiloxane (PDMS) or glass chambers. Partitioning of the assay inside these chambers has been achieved using vacuum [22, 23], pressure [24], SlipChip [25], hydrophilic

patterns [26, 27], or self-digitization [28]. While these techniques have been optimized and improved considerably, complicated fluidic control systems and complex micro and nanofabrication processes are required for them. Therefore, developing a platform to eliminate complicated fluidic control and fabrication processes would be desirable for highly accessible digital assay systems.

This thesis mainly focuses on exploring the simple digital quantification of target nucleic acids using partition-free solid-state nanopores and CRISPR towards rapid, label-free nucleic acid testing. The main contribution of this thesis is as follows.

First, we systematically studied the experimental factors beyond the intrinsic analyte concentration and electrophoretic mobility that affect the event rate in glass nanopore sensors. The synergistic effects of these factors on the event rates were investigated with the aim of finding the optimized experimental conditions for operating the glass nanopore sensor from the response time standpoint. In addition, we proposed and validated a calibration-free nanopore single molecule digital counting method for isolated molecule quantification. With the background ions as the in-situ references, the molecule translocation rates can be normalized to the ion translocation rates (baseline current). In recognition of this effect, we developed a quantitative model for molecule quantification without the need for prior knowledge of experimental conditions such as nanopore geometry, size, and applied voltage. This model was experimentally validated for different nanopores and DNA molecules with different sizes.

Second, we demonstrate the use of the glass nanopore for highly sensitive quantification of single-stranded circular DNAs (reporters), which could be degraded under the trans-cleavage activity of the target-specific CRISPR-Cas12a. We validated the concept of the solid-state CRISPR-Cas12a-assisted nanopores (SCAN) to specifically detect the HIV-1 DNAs. We found that SCAN can detect

target DNA concentrations above 10 nM within 1 hour. Afterward, we utilized the SCAN sensing strategy for the specific detection of SARS-CoV-2. We introduced a nanopore-sized counting method to measure the cleavage ratio of reporters, which is used as a criterion for positive/negative classification. With a preamplification and 30 min of CRISPR Cas12a assay, we achieved excellent specificity against other common human coronaviruses and a limit of detection of 13.5 copies/μl (22.5 aM) of viral RNA at the 95% confidence level.

Third, we developed a quantitative CRISPR sensing figure of merit (FOM) to compare different CRISPR methods and explore performance improvement strategies. The CRISPR sensing FOM is defined as the product of the limit of detection and the associated CRISPR reaction time. With the proposed CRISPR sensing FOM, we evaluated five strategies to improve CRISPR-based sensing: preamplification, enzymes of higher catalytic efficiency, multiple crRNAs, digitalization, and sensitive readout systems. In particular, we found that digitalization is the most promising amplification-free method for achieving comparable FOM performances (~ 1 fM·min) as those using preamplification. Afterward, we report the development of a self-digitalization through automated membrane-based partitioning (STAMP) technique to digitalize the CRISPR-Cas13 assay (dCRISPR) for amplification-free and absolute quantification of HIV-1 viral RNAs. The analytical performances of STAMP-dCRISPR were evaluated with synthetic HIV-1 RNA, and it was found samples spanning 4 orders of dynamic range between 100 aM to 1 pM can be quantified as fast as 30 min.

1.2. Overview of work presented

The first part of the thesis (chapter 2 and chapter 3) discusses the efforts to improve the glass nanopore sensor from the response time standpoint and demonstrates the glass nanopore as a calibration-free digital counter. Chapter 2 presents a quantitative study on the effect of intrinsic

nanopore properties and experimental configurations (surface charge, geometry, salt concentration, and translocation direction) on the event rates in the glass nanopore sensors. Chapter 3 demonstrates a calibration-free nanopore single molecule counting method for isolated molecule quantification. In the second part of the thesis (chapter 4 and chapter 5), we combined the high specificity offered by the Cas12a and the high sensitivity offered by the glass nanopore sensor towards an electronic sensing platform for sequence-specific nucleic acid detection. In chapter 4, the capabilities of solid-state CRISPR-Cas12a-assisted nanopores for HIV-1 DNA detection were demonstrated without a preamplification step. In addition, the sized counting method for nanopores-assisted CRISPR-Cas12a-based detection of SARS-CoV-2 was demonstrated in chapter 5. In the last part of the thesis (chapter 6 and chapter 7), we explored different techniques to improve CRISPR reaction performance and showed the digitalization technique as an alternative to preamplification for CRISPR diagnostic systems. A figure of merit was proposed in chapter 6 for CRISPR-based nucleic acid-sensing systems to quantitatively benchmark different methods and explore performance improvement strategies. In addition, chapter 7 presents a self-digitalization through automated membrane-based partitioning (STAMP) technique to digitalize the CRISPR-Cas13 assay (dCRISPR) for amplification-free and absolute quantification of HIV-1 viral RNAs. Finally, chapter 8 offers conclusions based on the work presented in the preceding chapters and perspectives for future development.

CHAPTER 2 QUANTITATIVE ANALYSIS OF FACTORS AFFECTING THE EVENT RATE IN GLASS NANOPORE SENSORS

In this chapter, we systematically studied the experimental factors beyond the intrinsic analyte concentration and electrophoretic mobility that affect the event rate in glass nanopore sensors. We developed a quantitative model to capture the impact of nanopore surface charge density, ionic strength, nanopore geometry, and translocation direction on the event rate. The synergistic effects of these factors on the event rates were investigated with the aim to find the optimized experimental conditions for operating the glass nanopore sensor from the response time standpoint. The findings in the study would provide useful and practical insight to enhance the device response time and achieve a lower detection limit for various glass nanopore sensing experiments.

2.1 Introduction

Solid-state nanopores made with silicon nitride[29-31], glass[32-34], and graphene[35], have become a versatile single-molecule analytical tool for label-free analysis of individual nucleic acids and protein molecules[36-39]. The nanopore sensor is usually operated by applying a small voltage bias across the nanometer-sized pore separating two chambers filled with electrolyte, the resulting ionic current through the pore (~0.01-100 nA) represents the readout signal[40, 41]. As the charged biomolecule is electrophoretically driven through the nanopore, the transient change in the ionic current indicates the passage of an analyte (often called an event). The shape, duration, magnitude, and frequency of these translocation events provide information about the molecule of interest (*e.g.*, size[42], charge[30], and concentration[43]). Although the nanopore sensor itself has single molecule sensitivity and resolution, a significant challenge in nanopore sensing is the prolonged

sense response time when analyte concentration decreases[44]. This issue stems from the diffusion-limited mass transport in nanopore sensors, resulting in the lack of efficiency for sampling sufficient numbers of molecules from the analyte solution[45]. Freedman *et al.* estimated that if the solution concentration is sub-picomolar, then there would only be 0.03 molecules in the capture volume, requiring more than 1-hour measurement time to observe a single event[46]. In our previous study of using glass nanopore as a digital single molecule counter, we have shown the relative uncertainty (δ) of inferring the event rate is $n^{-1/2}$, where n is the number of events. From the practical perspective, if one can only tolerate a maximal uncertainty percentage of δ_{max} and a maximal experimental time T_{max}, then a minimal event rate of $1/(\delta_{max}^2 T_{max})$ would be necessary. As a result, the event rate is of significant importance for achieving quicker sensor response and lower detection limits[47-49].

While molecular transport through nanopores has been studied extensively previously by examining the effect of applied voltage[42, 50], temperature, salt concentration[51], translocation direction[51], and the surface charge[52], only a few works were dedicated to addressing the event rate issue. For instance, to increase the flux of DNA to the nanopore, Wanunu *et al.* [42] applied asymmetric electrolyte solutions on both sides the nanopore to increase the electric field, focusing more molecules into the pore. Freedman *et al.* [46] employed single-molecule dielectrophoretic trapping to overcome the diffusion-limited motion of DNA towards the nanopore. In another study, localized optical heating of the plasmonic nanostructures at the nanopore was used to precisely control the temperature near the nanopore [53], which could be used to enhance the DNA event rate [54]. Most of these studies used external apparatus and components to enhance the translation rate. It remains less explored how the intrinsic nanopore properties and experimental configurations (surface charge, geometry, salt concentration, and translocation direction) affect the event rate in a synergistic study.

In this work, we performed a quantitative study on the effect of these experiment-relevant parameters on the event rates in the glass nanopore sensors. We developed a numerical model to evaluate the DNA event rate through the glass nanopore, which was validated by the experimental results. We systematically elucidated the effect of nanopore surface charge and ionic strength on the event rate of DNA through the conical shape nanopores. We examined the impact of various nanopore geometries (asymmetric nanopipette-based and symmetric membrane-based) on the event rate and their sensitivity to the change of surface charge and ionic strength. The event rate was found to be highly dependent on the direction of translation for asymmetric nanopores. We anticipate this event rate-focused study would provide useful and practical insight to enhance the device response time and achieve a lower detection limit for various glass nanopore sensing experiments.

2.2 Mathematical Model

Conceptually, the nanopore event rate is controlled by the slowest processes in the following three steps: (1) the DNA moves from the bulk toward the pore entrance by a combination of diffusion and drift forces; (2) the DNA is captured at the entrance of the nanopore; and (3) the DNA overcomes an entropy energy barrier and goes through the nanopore, causing a detectable ionic current blockade. Depending on the experimental conditions, the voltage-driven translocation of DNA molecules can be diffusion-limited or barrier-limited[50]. Since most of the glass nanopores used in the experiments were with size at least 10 nm in diameter and the voltage applied is less than 500 mV, the diffusion-limited mechanism is dominant in most of the glass nanopore experiments. As a result, our model will focus on the diffusion-limited regime without considering the nanopore-molecular interactions.

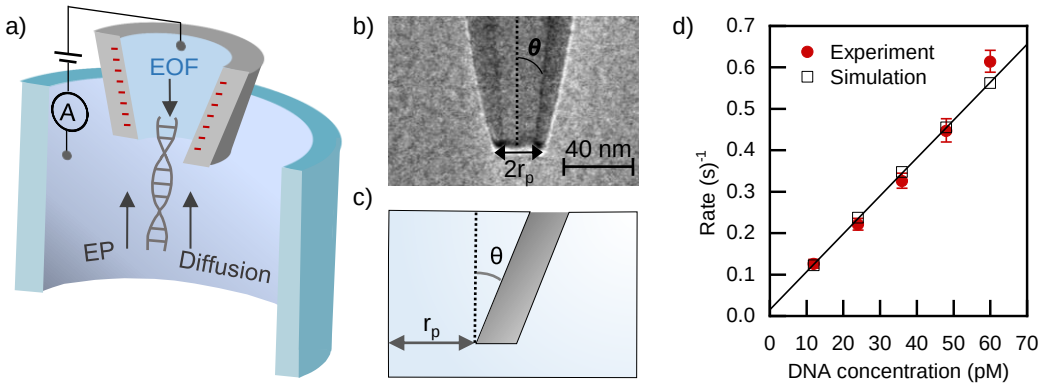

Figure 2-1. a) Interplay between diffusion, electrophoresis, and electroosmotic flow determines the molecule transportation through nanopores. b) TEM image of a typical conical-shaped glass nanopore. c) Schematic view of the nanopipette tip in the computational domain. Nanopipette geometry was defined by its diameter (2rp) and angle (θ). d) Validation of the model by comparing the simulation and experiment results, using 5 kb DNA at 1 M KCl under 400 mV bias. The diameter of the nanopore is 12 nm.

In the diffusion-limited regime, the molecular translocation through the nanopore is determined by the interplay between three motions: diffusion, electrophoresis, and electroosmotic flow (**Figure 2-1a**). The event rate is the outcome of these three forces. The Poisson-Nernst-Planck (Eq. 2.1 and Eq. 2.2), Navier-Stokes and continuity (Eq. 2.3 and Eq. 2.4) equations were used to capture the electric field, ionic and molecules concentration, and electroosmotic velocity distribution as follows:

$$\nabla^2 V = -\rho_e/\varepsilon_0\varepsilon_r \qquad (2.1)$$

$$\nabla \cdot J_i = 0 \qquad (2.2)$$

$$v\nabla^2 u - \nabla p - \rho_e \nabla V = 0 \qquad (2.3)$$

$$\nabla \cdot u = 0 \qquad (2.4)$$

in which V is the electric potential; $\rho_e = eN_A(\sum_i z_i c_i)$ is the charge density of mobile ions. ε_0, and ε_r is the vacuum and relative permittivity respectively. Note that the DNA charge density was not

taken into consideration for calculating the potential distribution since their concentration (~pM-nM) is negligible as compared to that of ions (~mM). In addition, the intermolecular interaction was not taken into consideration since the average distance between molecules will be a few microns when the concentration is less than 100. The molecular and ionic flux density J_i is given by:

$$J_i = -D_i \nabla c_i + c_i(u - z_i \mu_i \nabla V) \qquad (2.5)$$

where D_i, μ_i z_i and c_i are the diffusivity, mobility, valance, and concentration of each species. In Navier-Stokes and continuity equations (Eq. 2.3 and Eq. 2.4), u, p, and ν are velocity, pressure, and viscosity of the fluid. The molecular event rate R (s^{-1}) was obtained by integrating the molecules flux over the pore entrance area as:

$$R = N_A \int_S J_{molecules}\, dS \qquad (2.6)$$

where S is the surface area spanning the cross-section of the pore entrance.

The strongly coupled mathematical model was numerically solved with COMSOL Multiphysics. A two-dimensional axisymmetric computational domain was used to study the effect of surface charge, ionic strength, and nanopore geometry on the event rate (

Figure 2-2). The nanopore geometry was modeled after a typical conical-shaped glass nanopore (**Figure 2-1b**) by its radius r_p and angle θ (**Figure 2-1c**). The reservoir and glass nanopore was assumed to be large enough such that the ionic concentration far away from the pore is the bulk value. A voltage bias is applied between the two electrodes positioned far away from the pore.

a)

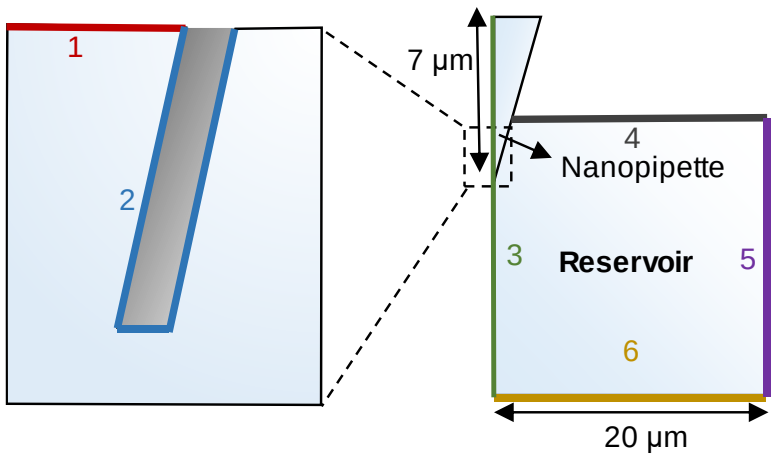

b)

Boundary \ Equation	Poisson	Navier–Stokes	Nernst–Planck for ions	Nernst–Planck for molecules
1	Voltage = V_0	Pressure = 0	Concentration = C_{ion}	Concentration = 0
2	Surface charge density	No-slip	Zero flux	Zero flux
3	Axial symmetry	Axial symmetry	Axial symmetry	Axial symmetry
4	Zero flux	Pressure = 0	Zero flux	Zero flux
5	Zero flux	No-slip	Zero flux	Zero flux
6	Ground	No-slip	Concentration = C_{ion}	Concentration = $C_{molecule}$

Figure 2-2. a) A two-dimensional axisymmetric computational domain used for our numerical platform. The reservoir (20 μm ×20 μm) and nanopipette were assumed large enough (7 μm) for the ionic concentration far away from the pore to maintain its bulk value Cion. b) The boundary condition for each set of equations: Poisson, Navier–Stokes, and Nernst-Planck for ions and molecules (DNA).

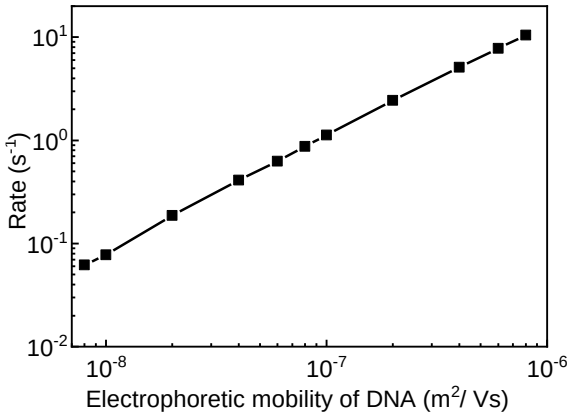

Figure 2-3. Calculated rates of 100 pM DNAs with different electrophoretic mobilities through a conical-shaped nanopore (12 nm diameter) at an ionic strength of 1 M and surface charge density of -20 mC/m2 .

In order to validate the model, we computed the event rate of 5 kb DNA at five different concentrations through a glass nanopore (r_p =6 nm and $\theta = 4°$) at 1 M KCl under 400 mV bias voltage. The numerical results were benchmarked to our previous experimental study[43]. In the simulation, we assumed the nanopore wall surface charge density of -20 mC/m^2 and the DNA mobility of 8×10^{-8} m^2/Vs, which is close to these derived from the experimental measurement [55, 56]. As shown in **Figure 2-1d**, an excellent agreement between the experimental and simulation results was obtained, confirming the validity of the mathematical model for evaluating the event rate. Note that the molecule electrophoretic mobility could also affect the event rate. Our numerical results (**Figure 2-3**) as well as previous analytical results [50] show that the event rate is linearly dependent on the molecular mobility in the diffusion-limited regime. In this work, we aim to study the factors affecting the event rates beyond the intrinsic analyte concentration and electrophoretic mobility.

2.3 Results and discussion

2.3.1 Impact of Surface Charge and Ionic Strength

The nanopore surface charge affects the translocation process through the electroosmotic flow (EOF)[52], which arises from the electrostatic interaction between the electric field and mobile ions in the electric double layer (EDL)[57]. For the applied electric field, as shown in **Figure 2-1a**, the EOF would always oppose the motion of the negatively charged molecules (e.g., DNAs) if the nanopore walls are negatively charged[58]. Another factor affecting the EOF is the ionic strength since the Debye length in the EDL is strongly salt concentration dependent. It has been previously observed in the experiment that DNA translocation in the glass nanopore is strongly salt-dependent[51].

To study the synergistic effect of both surface charge and ionic strength, we calculated the event rate of 100 pM DNA through a conical-shaped nanopore with a diameter of 12 nm and angle of θ = 4°. **Figure 2-4a** plots the event rate heatmap, which clearly shows the rate strongly depends on the ionic strength and surface charge density. We observed a few interesting features. First, for each specific ionic strength, the event rate reduces when the surface charge becomes more negative due to the increased retardation EOF. **Figure 2-4b** shows the event rate as a function of surface charge for various ionic strength conditions. The event rate was found to be exponentially increased when decreasing the surface charge. Second, at a specific surface charge density, working at higher ionic strength conditions would help to increase the event rate. This is because the EOF becomes less significant at higher salt concentrations. **Figure 2-4c** illustrates the event rate as a function of ionic strength for various surface charge conditions. The effect of ionic strength on the rate becomes less significant when the surface charge density reduces. In the case of zero surface charge, the ionic strength does not affect the event rate at all. Finally, **Figure 2-4a** also shows that working at low

salt concentrations with a highly negatively charged nanopore would result in a very low event rate. The empty area in **Figure 2-4a** shows the region where the translation rate is less than 10^{-3}/s. This rate is impractical for gathering sufficient events to build robust statistics within a reasonable amount of time. For instance, with a rate of 0.001 s^{-1} and an experiment time of 1 hour, we can only expect to count less than 4 events.

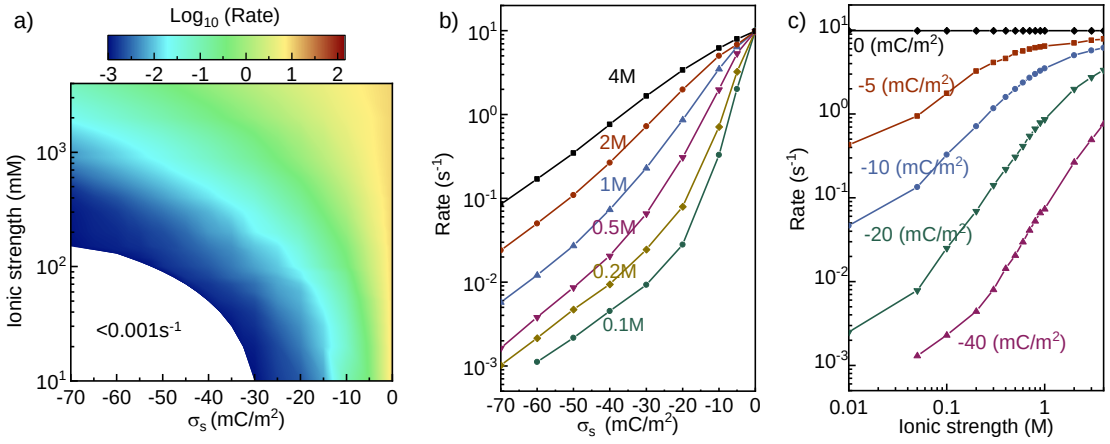

Figure 2-4. a) Event rate of 100 pM DNA through a conical-shaped nanopore (12 nm diameter) for a different range of ionic strength (10 mM to 4 M) and surface charge density (0 to -70 mC/m^2). b) Effect of surface charge density on the event rate at various ionic strengths. c) Effect of ionic strength on the event rate at various surface charge densities.

These results have a few implications for the nanopore experiments. From the fast sensor response time perspective, working at higher ionic strengths with a nanopore of a lower surface charge would be favorable. Nevertheless, various bioassays have an upbound for the salt concentration[59]. For example, the usual 1-4 Molar salt concentration used in a typical nanopore experiment might be detrimental for assays such as polymerase chain reaction (PCR) and loop-mediated isothermal amplification (LAMP) [60]. As a result, a neutral (or close to neutral) nanopore surface would be preferred for experiments that require a specific salt condition.

2.3.2 Impact of Nanopore Geometry

It was previously found that the electric field and electroosmotic flow strongly depend on the nanopore geometry[61]. This suggests that alternation of the nanopore geometry is of potential use for enhancing the event rate. To this end, we examined the event rate of 100 pM DNA at an ionic strength of 1 M and a surface charge density of -20 mC/m^2 through nanopores of varying angles and diameters. **Figure 2-5a** illustrates the event rate heatmap, which clearly shows the rate strongly depends on the nanopore diameters and angles.

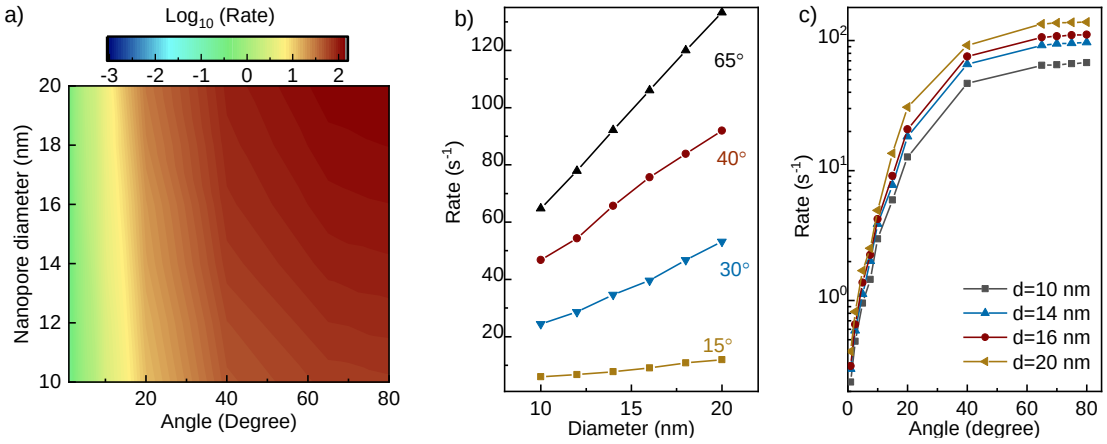

Figure 2-5 a) Event rate for 100 pM DNA through the nanopore at an ionic strength of 1 M and surface charge density of -20 mC/m^2 with different diameters and angles. b) Effect of nanopore diameter on the event rate at different angles. c) Effect of nanopore angle on the event rate at different sizes.

Figure 2-5b shows the event rate as a function of nanopore diameters for four different angles. For a specific angle, the event rate increases linearly with the nanopore size. This is not surprising at first glance since a larger pore would be less resistant for translocation. A detailed calculation reveals the nanopore conductance is approximately linearly to r_p. However, there is another factor that contributes to the enhanced rate. As the nanopore size increases, the effective electric field

across the nanopore region would be reduced, which in turn reduces the opposing EOF flow. This result means a larger nanopore would be preferred from the response time perspective. However, the nanopore diameter needs to be comparable to the size of the analyte molecule to ensure single molecule sensitivity and thus cannot be scaled up arbitrarily.

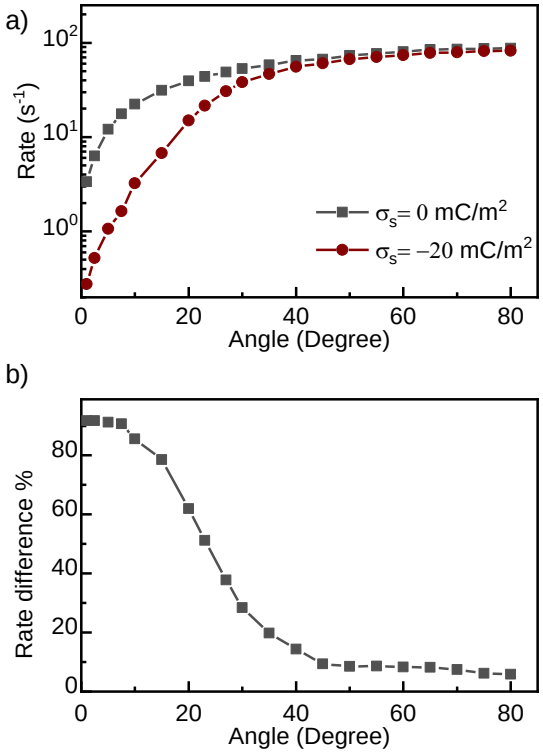

Figure 2-6 a) 100 pM DNA event rate at different angles for surface charge density of 0 (Without EOF) and -20 mC/m^2 (With EOF),with nanopore diameter of 12 nm and ionic strength of 1 M, and b) The rate difference percentage for different angles with and without EOF, defined as (R_{woEOF}-R_{wEOF})/R_{woEOF}.

Figure 2-5c plots the event rate as a function of nanopore angles for four diameters. A clear enhancement of the rate was observed when increasing the nanopore angle (nanopore become more flattened). This effect was also due to the contributions of two factors. The first is the increase of the nanopore conductance. The second is the reduced impact of EOF. To examine the impact of

EOF, we calculated two representative cases: no surface charge (without EOF), and -20 mC/m^2 surface charge (with EOF). As shown in **Figure 2-6a**, the impact of nanopore angles on the rate is less significant for the case without the EOF. Moreover, the rates with the EOF is much less than that without the EOF, and the reduction is angle dependent. As shown **Figure 2-6b**, the EOF induced rate reduction is much more significant at smaller angles.

2.3.3 Silicon Nitride vs. Glass Nanopores

The results shown in **Figure 2-6** implies that a more widely opened nanopore would be preferred from the event rate perspective. For typical laser-pulled glass nanopores, the range of the angle is limited to be within 2-12 degrees[62, 63]. On the other hand, membrane-based silicon nitride (SiNx) nanopores represent another very important nanopore geometry with an angle equal to 90 degrees[64]. We set out to compare the event rate between the typical glass nanopore (**Figure 2-7**) and SiN_x nanopores (**Figure 2-7b**). Both pores are assumed to have the same diameter of 12 nm. The glass nanopore is assumed to have an angle of $\theta = 4°$. The heatmap in **Figure 2-7a** and **b** show the event rate as a function of ionic strength and surface charge. To quantitatively evaluate the rate difference, **Figure 2-7c** plots the rate ratio between the SiN_x nanopore and the glass nanopore. It was found that the rate in the SiN_x nanopore is always higher than that in the glass nanopore under the same ionic strength and surface charge condition (note that an equal rate will have the log ratio of 0). This rate enhancement in the SiN_x nanopore is because of not only the less resistive molecule transport path but also, the less impact of the opposing EOF flow. The difference in the rate between the glass and SiN_x becomes more pronounced at low salt concentration and high surface charges, an expected feature that comes from the EOF dependence on the salt concentrations and surface charges. This result means that the membrane-based SiNx nanopore is favorable to achieve a fast event rate as compared to the conical-shaped glass nanopore, giving everything else the same.

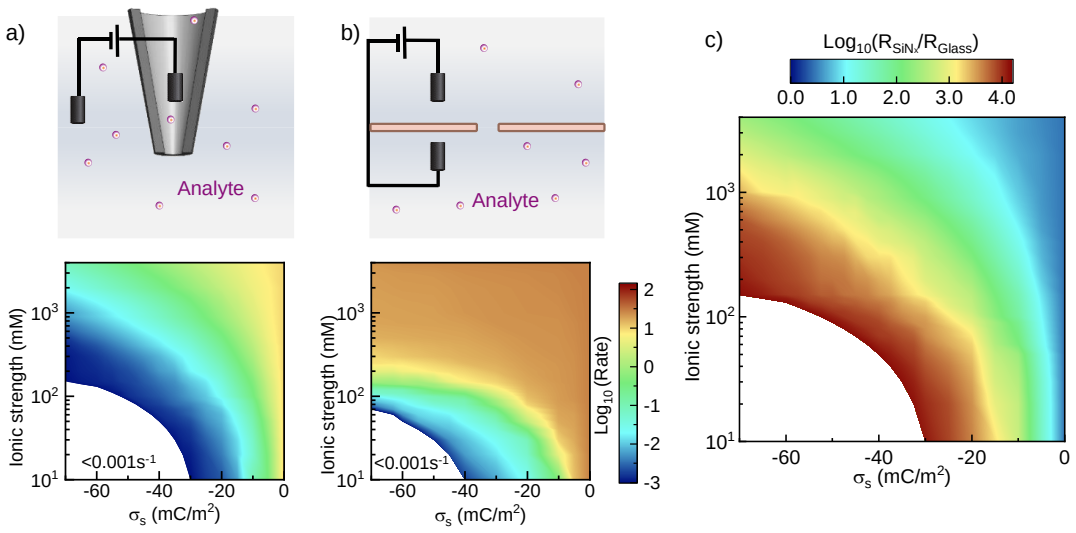

Figure 2-7. Event rate of 100 pM DNA through a) conical-shaped glass nanopore, and b) SiN_x nanopore, both with a diameter of 12 nm. c) The translocation ratio between the SiN_x and glass nanopores as a function of surface charge density and the ionic strength.

2.3.4 Impact of Direction

It was previously reported that DNA translocation in the glass nanopore is strongly salt- and direction-dependent[51], consistent with our own observations (**Figure 2-8**). While the asymmetric ionic transport behavior in nanofluidic diodes was well established and the underlying physical mechanism was well understood (broken symmetry)[65]. The impact of EOF on the transport process was neglected in most studies[66], although EOF would oppose the electrophoretic motion. In addition, it was previously shown that EOF itself is asymmetric which can lead to the electroosmotic flow rectification in conical nanopores[67].

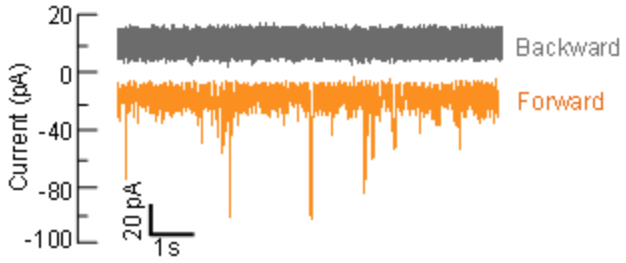

Figure 2-8 Translocation recording of λ-DNA through glass nanopore at 0.1M KCl under 400 mV bias for backward (a) and forward (b) configurations. For the forward case, no translocation events occur in the duration of the recording. However, in the backward configuration, many events are detected. Note that the sole current change during the backward translocation was an increase, as previously observed for conical pores at low salt concentrations[68]. Hence, the data clearly illustrates that DNA event rate in the glass nanopore is strongly direction-dependent.

Therefore, the electrophoretic flow and EOF should be considered to understand the experimentally observed molecular rectification. To make the following discussion clear, we define the translocation out from and into the glass nanopore as forward and backward direction, respectively (**Figure 2-9a** and **b**). Note this definition is opposite to that of Keyser *et al* [51]. **Figure 2-9c** and **d** plot the event rate under the influence of EOF as a function of ionic strength and surface charge for forward and backward configurations, respectively. It is noteworthy that regardless of the translocation direction, EOF is *always* an opposing force against the DNA movement if the surface charge is negative, which means the DNA event rate with EOF is always lower than that without the EOF.

Figure 2-9e illustrates the ratio of $R_{forward}$ /$R_{backward}$ (rate rectification ratio) at different surface charges and ionic strengths. It was clear that the rate in the forward direction is always larger than that in the reserve direction.

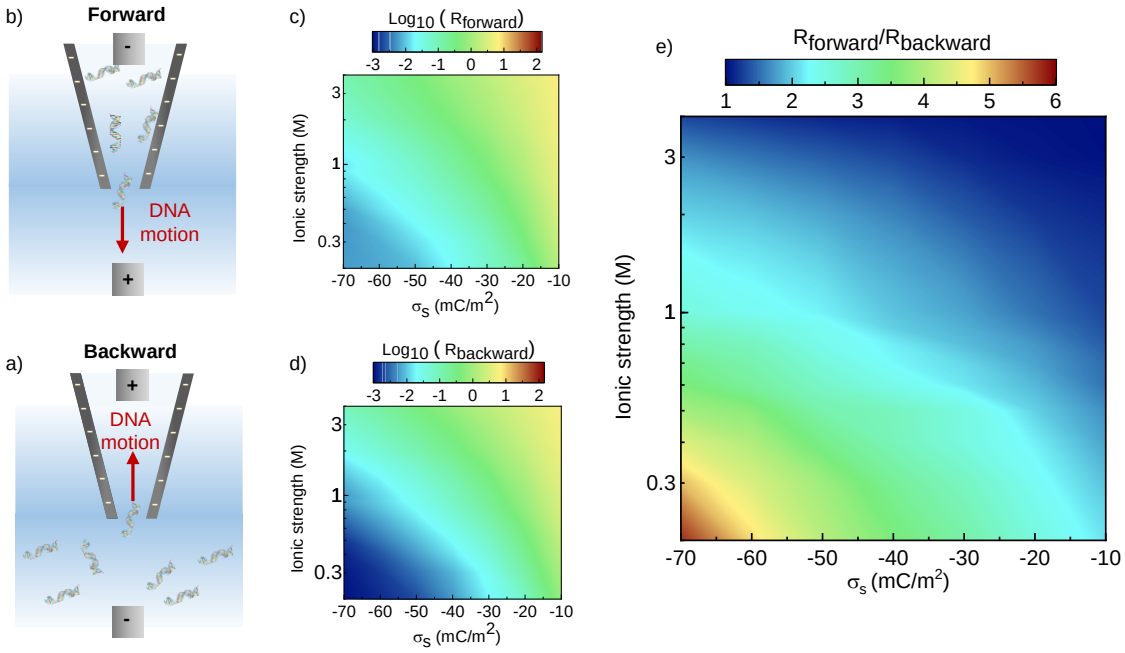

Figure 2-9. Schematic of DNA translocation in a) forward and b) backward direction, as well as the event rate of the 100 pM DNA through the 12 nm conical shape nanopore in the c) forward and d) backward configuration. e) The event rate ratio between the forward and backward configurations. The translocation rectification effect is more pronounced in the low salt and high surface charge region.

In addition, the rate rectification ratio is more pronounced (ratio away from unity) when working at low ionic strengths with a highly charged nanopore surface due to the enhanced electroosmotic flow rectification ratio in these regions[67].

These results elucidate the importance of EOF in molecule transport through the glass nanopore and provide experimental Insights for enhancing the event rate. For example, if one can reverse the surface charge polarity through surface functionalization, the resulting EOF will always enhance the DNA event rate. In addition, loading the analyte molecules into the glass nanopore for analysis would be preferred from the rate enhancement perspective.

2.1. Summary

In summary, we presented a comprehensive study of factors affecting the event rate in glass nanopore sensors. This event rate-focused study aims to provide useful and practical insight to enhance the device response time for various glass nanopore sensing experiments. We found that while the event rate intrinsically depends on the analyte concentration and mobility (linearly), factors such as nanopore surface charge density, geometry, ionic strength, and the translocation direction could impact the event rate non-linearly by orders of magnitude. From the standpoint of enhancing the response time in glass nanopore sensors, higher ionic strength, lower nanopore surface charge (neutral surface is ideal), and less vertical nanopore walls would be desirable due to the reduced impact of the opposing electroosmotic flow. Due to the negative surface charge in glass nanopores, translocation from the glass nanopore could be orders of magnitude faster than that into the nanopore at low salt concentrations and higher surface charges. Therefore, attention should be paid when setting up the translocation direction in the glass nanopore due to the electroosmotic flow rectification. In addition, we found SiNx membrane-based nanopores are generally favorable over glass nanopores for achieving a fast response, especially when working with low ionic strength and higher surface charge densities. We anticipate these findings would provide insight for future glass nanopore sensing experiments towards ultrasensitive sensing applications where the device response time is of significant importance.

CHAPTER 3 CALIBRATION-FREE NANOPORE DIGITAL COUNTING OF SINGLE MOLECULES

In this chapter, we proposed and validated a calibration-free nanopore single molecule digital counting method for isolated molecule quantification. With the background ions as the in-situ references, the molecule translocation rates can be normalized to the ion translocation rates (baseline current). This in-situ reference alleviates the requirement for knowing the nanopore geometry and size or generating a calibration curve. In recognition of this effect, we developed a quantitative model for molecule quantification without the need for prior knowledge of experimental conditions such as nanopore geometry, size, and applied voltage. This model was experimentally validated for different nanopores and DNA molecules with different sizes. We anticipate this calibration-free digital counting approach would provide a new avenue for nanopore-based molecule sensing.

3.1 Introduction

Quantification of isolated biomolecules such as DNAs, RNAs, and proteins is of critical importance for various applications in environmental, medical, and food science studies[69, 70]. This process is routinely accomplished by bulk-based optical sensing methods such as UV-VIS spectrophotometry[71] or dye-based fluorimetry[72]. The resulting analog readout signal is proportional to the bulk sample concentration, the value of which can be determined with a reference curve (**Figure 3-1a**). In contrast to the analog sensing method, digital assays have emerged as a highly sensitive approach for concentration quantification[73]. Notable examples include digital PCR[74-76], digital ELISA (enzyme-linked immunosorbent assay)[77-79], and digital ELOHA (enzyme-linked oligonucleotide hybridization assay)[80].

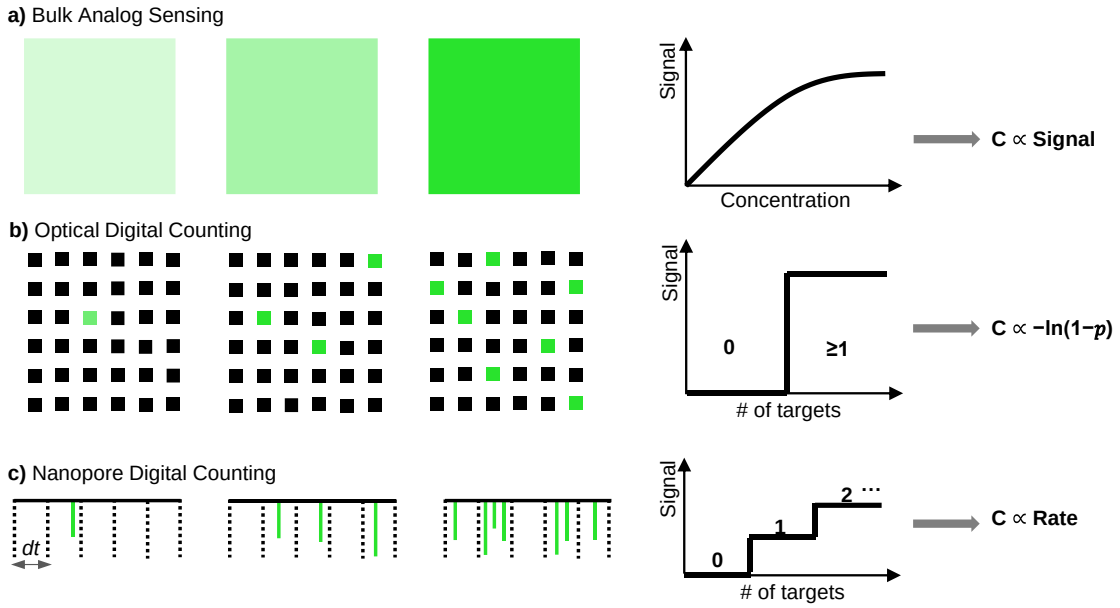

Figure 3-1. Comparisons for different quantification methods. a) Analog sensing generates a signal proportional to the bulk sample concentration. b) In the optical digital counting, the sample is partitioned into many small containers such that each partition contains a discrete number of biological entities. The sample concentration is determined by Poisson statistics (p is the positive ratios). c) In nanopore digital counting, the sample concentration is proportional to the single molecule translocation rates.

The general concept of the digital assays is that the sample is physically partitioned into many small chambers such that each partition contains a discrete number of molecules (0, 1, 2, …). Each partition gives a binary 0 and 1 signal corresponding to the case of no molecule presented and at least one molecule presented, respectively. Note that the digital assay does not necessarily mean each partition has either zero or one molecule. With Poisson statistics, the sample concentration can be estimated by -ln(1-*p*), where *p* is the ratio of the positive partitions over total partitions (**Figure 3-1b**).

The digital assays so far are predominated by physical partitioning and optical detection methods to generate the binary signal. Nanopore-based sensors[34, 81-93] allow single molecules to be analyzed electronically without the need for labeling and partitioning. Conceptually, nanopore

sensor represents an ideal single molecule counting device due to its unique features of label-free electronic sensing, single-molecule sensitivity, and potential reusability. When a single molecule is electrophoretically driven through the nanopore, a detectable ionic current blockade generates a digital '1' signal, the rate of which is proportional to the sample concentration (**Figure 3-1c**). Resolving this digital event itself is much easier than analyzing its analog features such as magnitude and duration of the current dip.

Existing theories[83, 94, 95] and experiments[34, 96, 97] have shown that when interactions between molecules are negligible, the molecule molar concentration (mol/m^3) is linearly related to the translocation rate (s^{-1}) as $R=\alpha N_A C$, where N_A is the Avogadro constant, and α is usually referred to as the capture rate[94, 98]. Wanunu *et al.* successfully applied this principle to quantify the isolated miR122a electronically[99]. Since capture rate α strongly depends on experimental parameters such as nanopore geometry[94, 100], temperature[96, 101], molecule size[83], and applied voltage[102, 103], a calibration curve of the rate versus concentration was necessary to infer the unknown sample concentration[99]. Moreover, the calibration curve must be obtained under the same experimental conditions for comparable capture rate α. Unfortunately, generating this calibration curve is often time-consuming and challenging due to nanopore clogging issues[104, 105].

In this work, we set out to develop a calibration-free nanopore single molecule counting method for isolated molecule quantification. We first studied the statistics of the molecule translocation rate and developed an experimentally practical method to measure the rate. We developed a quantitative model for molecule quantification without the need for prior knowledge of experimental conditions such as nanopore geometry, size, and applied voltage. This is achieved by using the background ions as the *in-situ* reference such that the molecule translocation rates can be normalized to the ion translocation rates (baseline current). This model was experimentally

validated for different nanopores and DNA molecules with different sizes. While the results presented in this work were from glass nanopores and DNA molecules, the principle could be well extended to other nanopore types and other charged molecules.

3.2 Methods

3.2.1 Materials and chemicals**.**

0.2 mm Ag wires (Warner Instruments, Hamden, USA) were used to fabricate the Ag/AgCl electrodes in house. Microinjectors of 34 gauge was purchased from World Precision Instruments. Potassium chloride and Tris-EDTA-buffer solution (10 mM Tris-HCl and 1 mM EDTA) were purchased from Sigma-Aldrich. Piranha solution was made by mixing concentrated sulfuric acid (H_2SO_4) with hydrogen peroxide (H_2O_2). Quartz capillaries with inner and outer diameter of 0.5 mm and 1 mm were purchased from Sutter Instrument. We filtered the testing solutions with a 0.2 μm syringe filter (Whatman). DNA templates (λ-DNA, 10 kbp and 5 kbp DNA with the concentration of 0.5 μg/μl) were purchased from ThermoFisher.

3.2.2 Glass nanopore fabrication.

The quartz capillaries were firstly cleaned in Piranha solution for 30 minutes to remove organic residues, then rinsed with DI water, and dried in an oven at 120 ℃ for 15 min. A two-line recipe, (1) Heat 750, Filament 5, Velocity 50, Delay140, and Pull 50; (2) Heat 710, Filament 4, Velocity 30, Delay 155, and Pull 215, were used to pull the capillaries with a laser pipette puller (P-2000, Sutter Instruments, USA). This recipe typically produces nanopore size around 10 nm. Despite

known batch-to-batch variations in size, the method presented in this work is valid as long as the nanopore can resolve the single molecule translocation (rather than multiple molecules).

3.2.3 Glass nanopore characterization with I-V, SEM, and TEM.

Glass nanopore characterization was performed by standard I-V measurement, SEM, and TEM imaging. For I-V characterization, the glass nanopore was filled with 1M KCl in Tris-EDTA buffer by a microinjector and then immersed in the testing solution. Home-made Ag/AgCl electrodes were used for interfacing the electrical measurement (**Figure 3-2a**), and the I-V curve was recorded for nanopore size estimation (**Figure 3-2b**). For SEM imaging (**Figure 3-2c**), the glass nanopore was coated with 5 nm thick of Iridium to avoid the charging effect. TEM characterization was also performed to obtain detailed information for the nanopore geometry and size (**Figure 3-2d**).

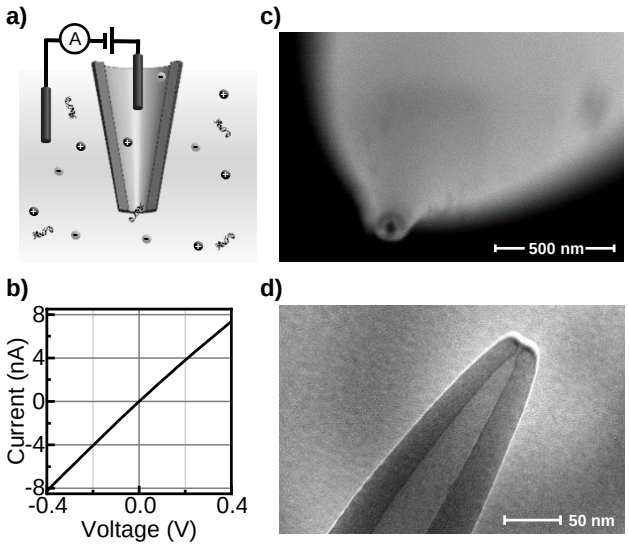

Figure 3-2. Experimental setup and nanopore characterization. a) Illustration of the experimental setup (not to scale). Ag/AgCl electrodes were inserted to the nanopore and bulk solution to apply the bias voltage across the nanopore. b) A typical IV curve for glass nanopore in 1 M KCl with Tris-EDTA-buffer solution. c) SEM image of the glass nanopore showing the overall shape. d) The TEM image of the nanopore tip showing apparent conical shape.

3.2.4 Single molecule counting measurement and data analysis.

The schematic of the single molecule counting setup is illustrated in **Figure 3-2a**. 1 M KCl in Tris-EDTA buffer was used for all DNA experiments to decrease the effect of electroosmotic flow[106]. A voltage was applied across the nanopore by 6363 DAQ card (National Instruments, USA). The resulting current was amplified by a transimpedance amplifier (DLPCA-200, FEMTO, Germany) and then digitalized by 6363 DAQ card with 100 kHz sampling rate. The recorded current time trace was analyzed by a customized MATLAB (MathWorks) software to extract the single molecule translocation information regarding the interarrival time between translocation events, the ionic current dip, and the molecule dwell time.

3.3 Results and discussion

3.3.1 DNA translocation statistics

It was previously observed that the mean time between single-molecule capture events in solid-state nanopore follows an exponential distribution[100], indicating a Poisson process[100, 107]. To validate if this is also true in our glass nanopore, we performed studies on λ-DNAs with a serial of concentrations ranging from 12-60 pM. A quick eyeball on the current time traces in **Figure 3-3a** shows that translocation occurs more often as the concentration increases. The extracted inter-arrival time distribution also shows a remarkable exponential distribution for each concentration (**Figure 3-3b**). Note that the exponential fits to these distributions are usually used to obtain the hidden translocation rate[83, 100].

To further confirm the Poisson process, the same raw data sets were used to extract the probability distribution $P(n)$ for observing n events within a fixed time interval (**Figure 3-3c**). Each

concentration case is then fitted with a Poisson distribution, $P(n) = e^{-\lambda}\lambda^n/n!$, where λ is the expected occurrence of the events. In a process with the rate of R, $\lambda = Rdt$ where dt is the time interval[100].

As shown in **Figure 3-3d**, both fittings to the exponentially distributed inter-arrival time and fittings to the Poisson distribution yield comparable rate determination at different concentrations. **Figure 3-3d** also shows there is a linear relationship between translocation rate and the DNA concentrations in the glass nanopores, consistent with the theory prediction[94] and previous experimental studies[34, 95, 96].

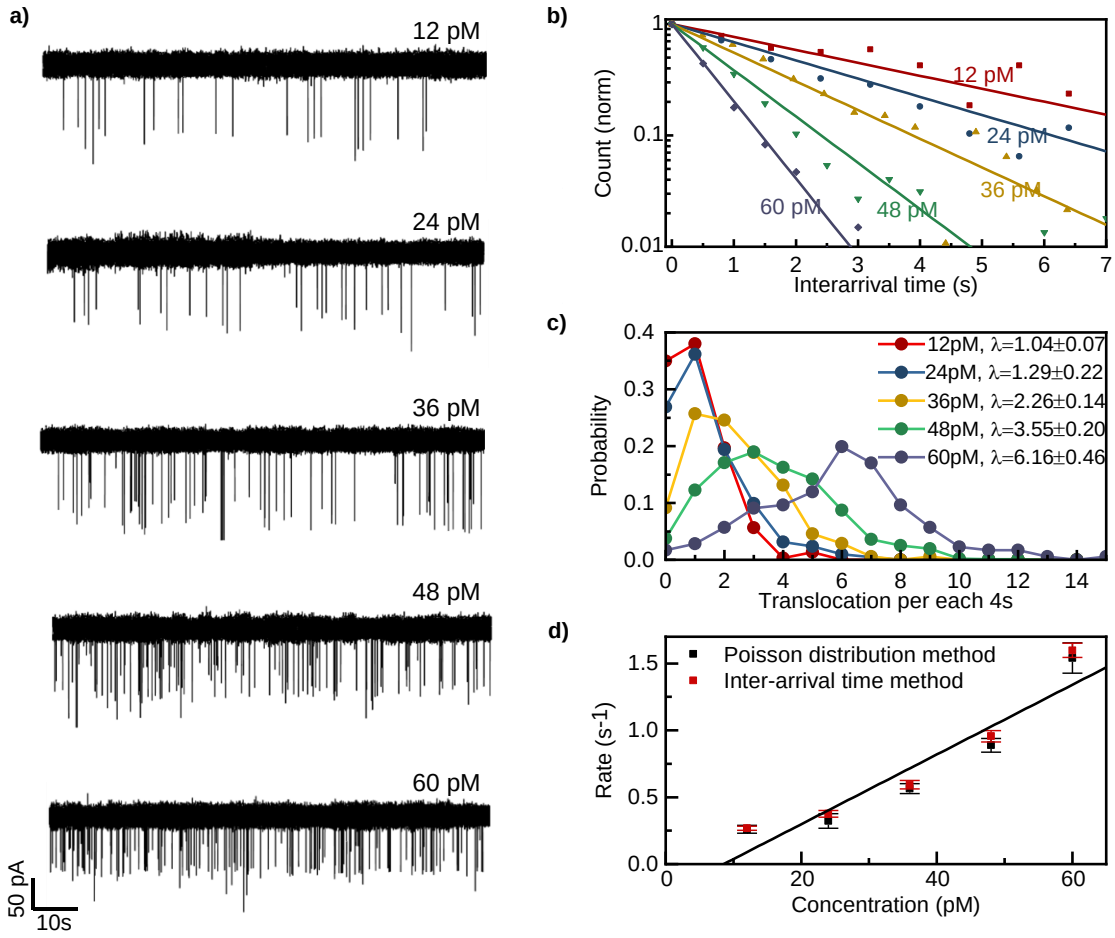

Figure 3-3. Translocation recording of λ-DNA through glass nanopore at 1M KCl under 400 mV bias. a) Continuous current readout illustrating the translocation events at different

DNA concentrations. The average molecular distance is around 3 μm, the interactions between molecules are negligible. b) Normalized distributions of interarrival time for different concentrations with mono-exponential fits to the distributions. c) The probability distribution of the events for different concentrations. The 4s time interval is used to better show the Poisson distribution. d) The translocation rate obtained from both fitting methods versus the λ-DNA concentrations.

3.3.2 n/T method for capturing translocation rate

While both fitting methods provide a measure of the rate *R*, the result can only be obtained off-line after enough digital events were registered to generate sufficient data points for fitting. A more practical approach to determine the rate on-line is by counting the number of events per certain time while the experiment is ongoing. Since the translocation events follow the Poisson process, assuming *n* discrete single-molecule translocation events were observed in a particular observation time window *T*, one can infer the rate with a certain confidence interval as $(n \pm z(n)^{1/2})/T$, where *z* is the standard score. The 95% confidence interval of the rate is $(n \pm 1.96(n)^{1/2})/T$ [108]. We denote this approach as the *n/T* method hereafter. The relative uncertainty of inferring the rate *R* is proportional to $n^{-1/2}$.

It is thus clear that there is a trade-off between minimizing the uncertainty (increasing *n*) and achieving real-time rate determination (reducing *n*). **Figure** 3-4 compares the inferred rate using the online *n/T* method to the rate determined by the Poisson fitting method, using 12 pM λ-DNA sample. Two features were observed when more digital translation event was observed. First, the relative uncertainty (error bars) was reduced to that of the Poisson fitting method. Second, the mean rate estimation (diamonds) converged to the translocation rate obtained from the Poisson fitting method. These two features can be seen quantitively in the inset of **Figure** 3-4, *i.e.*, as more digital translations were observed, both mean and uncertainty ratios converge to 1. This validates the *n/T*

method for rate determination as long as sufficient translocations were observed. Experimentally, we examined at least 200 events for measurement uncertainty <7%.

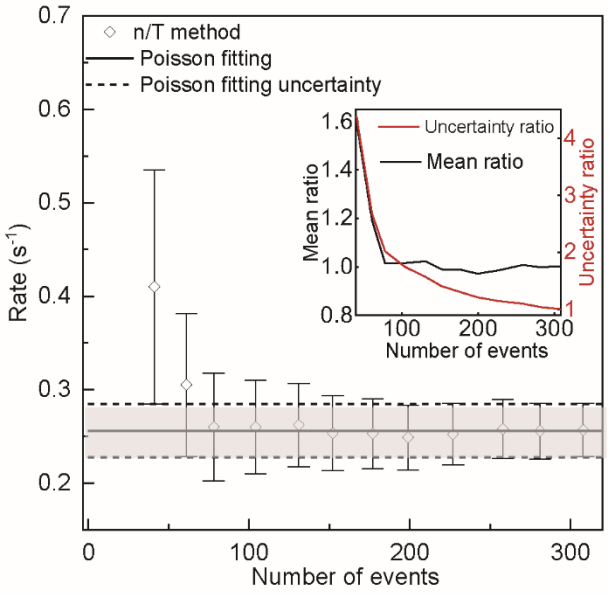

Figure 3-4. The translocation rate determined by the n/T method for increasing the observation numbers. The shaded area is the value obtained by the Poisson fitting method (mean + uncertainty). The inset shows the mean and uncertainty value comparison between these two methods.

3.3.3 Calibration-free model

With an experimentally efficient *n/T* approach to determine the rate, the next task is to determine the capture rate α. The dynamics of molecule translocation through the nanopore consists of three steps: (1) the molecule moves from the bulk of the reaction chamber toward the pore entrance by a combination of diffusion and drift forces; (2) the molecule is captured at the entrance of the nanopore; and (3) the molecule overcomes an entropy energy barrier and goes through the nanopore, causing a detectable ionic current blockade which can be detected electronically as a digital signal [94]. It is known that the capture rate α could be diffusion limited (step 1) or barrier limited (step 3) [83]. The glass nanopores used in our experiments are around 10 nm in size, which

is large enough such that the transport is diffusion limited rather than barrier limited [109, 110], as indicated by the linear dependence of the capture rate on voltage (**Figure 3-5**).

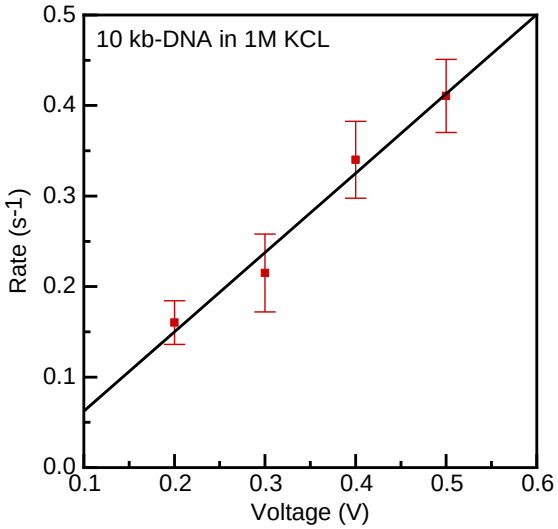

Figure 3-5. Linear dependence of the translocation rate on the applied voltage for 24 pM 10 kbp DNA in 1M KCl buffer solution

In the diffusion-limited region, the capture rate for the conical-shaped glass nanopore is given by $\alpha=2\pi\mu\tilde{d}\Delta V$, where μ is the free solution electrophoretic mobility, ΔV is the applied electric potential across the pore, and $\tilde{d}$ is the characteristic length of the nanopore. If the nanopore geometry and size is explicitly known for a particular experiment, the capture rate can be directly calculated to determine the unknown sample concentration without calibration, similar to a pressure-driven calibration-less quantitation of nanoparticles by calculating the hydrodynamic resistance[111]. Nevertheless, it's well known that glass nanopore geometry is widely dispersed[112]. TEM characterization of each nanopore is often destructive and is time-, facility-, and expertise-intensive[113]. In addition, experimental conditions such as applied voltage, temperatures, and buffers also vary from one experiment to the other. To properly determine the unknown sample

concentration, a calibration curve must be obtained under the same experimental conditions to extract the capture rate α in that particular experiment[83]. While this could be done, it is often time-consuming and experimentally challenging due to potential nanopore clogging under repetitive testing[104].

To overcome these challenges, we here developed an *in-situ* method for determining the capture rate α without the need for prior knowledge on nanopore experimental conditions. This is achieved by recognizing that the baseline current carries information about the background ion translocation rate (**Figure 3-6a**). Therefore, it is feasible to use the ionic concentration (generally known for a particular experiment) as the internal reference to estimate the unknown capture rate α. The baseline current can be estimated as $I_b=2\pi\Lambda C_{ion}\ \tilde{d}\ \Delta V$, where Λ is the molar conductivity which depends on the mobility and valance of the ions as $\Lambda = \sum_i N_A e z_i \mu_i$ [114]. The previously inaccessible parameter $\alpha=2\pi\mu\tilde{d}\Delta V$ can be rewrote as:

$$\alpha = \frac{\mu I_b}{\Lambda C_{ion}} \qquad (3.1)$$

Eq. 3.1 implies that the unknown capture rate can be derived from the experimentally accessible baseline current and the ionic concentration without knowing the nanopore geometry, size and the applied voltage. The molecule mobility μ and molar conductivity Λ can be estimated for a particular molecule and salt. Thus, the molecule translocation rate $R=\alpha N_A C_{mol}$ can be written as:

$$R = \frac{\mu N_A C_{mol}}{\Lambda C_{ion}} I_b \qquad (3.2)$$

To validate Eq. 3.2, we performed experiments with 10 kbp DNA at 24 pM in the 1M KCl buffer solution. **Figure 3-6b** shows the current time trace at different applied voltages for two glass nanopores pulled from different batches. Two features can be observed. First, higher applied

voltage leads to a higher molecule translocation rate, consistent with previous reports[83]. Second, due to the nanopore size variation, the same applied voltage does not generate the same molecule translocation rate. This dependence of the translocation rate on applied voltages and the nanopore sizes indicates a calibration curve must be obtained under the same experimental conditions (the same pore and applied voltage)[97]. Fortunately, Eq. 2 predicts that the molecule translocation rate scales linearly with the baseline current for a fixed testing molecule and salt concentrations. This is exactly what we observed in **Figure 3-6c**. The molecule translocation rate versus the I_b indeed falls into a single line for different pores at different applied voltages.

After verifying this *in-situ* ionic current reference model, calibration-free quantification of the molecule molar concentration can thus be performed by rewriting the Eq. 3.2 as:

$$C_{mol} = \frac{\Lambda R}{\mu N_A I_b} C_{ion} \qquad (3.3)$$

Eq. 3.3 shows that unknown sample concentration can be quantified without explicitly knowing the nanopore geometry, size and the applied voltage, as long as the parameters on the right-hand side of the equation could be determined. To validate this method, we tested λ-DNA, 5 kbp DNA, and 10 kbp DNA at five known concentrations (12, 24, 36, 48, and 60 pM) in 1M KCl buffer, intentionally using glass nanopores pulled from different batches. Since the free solution electrophoretic mobility of DNA in Tris-EDTA buffer was theoretically[115] and experimentally[116] shown to be independent on the DNA length longer than a few persistence lengths[117], μ of 4.5×10^{-8} $m^2V^{-1}s^{-1}$ was used for all DNA molecules[56]. The buffer solution is dominated by 1 M KCl and thus the molar conductivity Λ is estimated to be 10.86 $m^{-1}M^{-1}S$ [114]. **Table 3-1** summarizes the results for this calibration-free method for concentration measurement. The baseline current (I_b) and translocation rate (R) was determined from the experiment. **Figure 3-6d** plots the measured versus the input concentration for all tests. All data points falling into a

straight line of slope 1, indicating the accuracy of the calibration-free method. It is noteworthy that the molecule concentration determined by Eq. 3.3 is widely applicable to other kinds of molecules as long as their electrophoretic mobility was known.

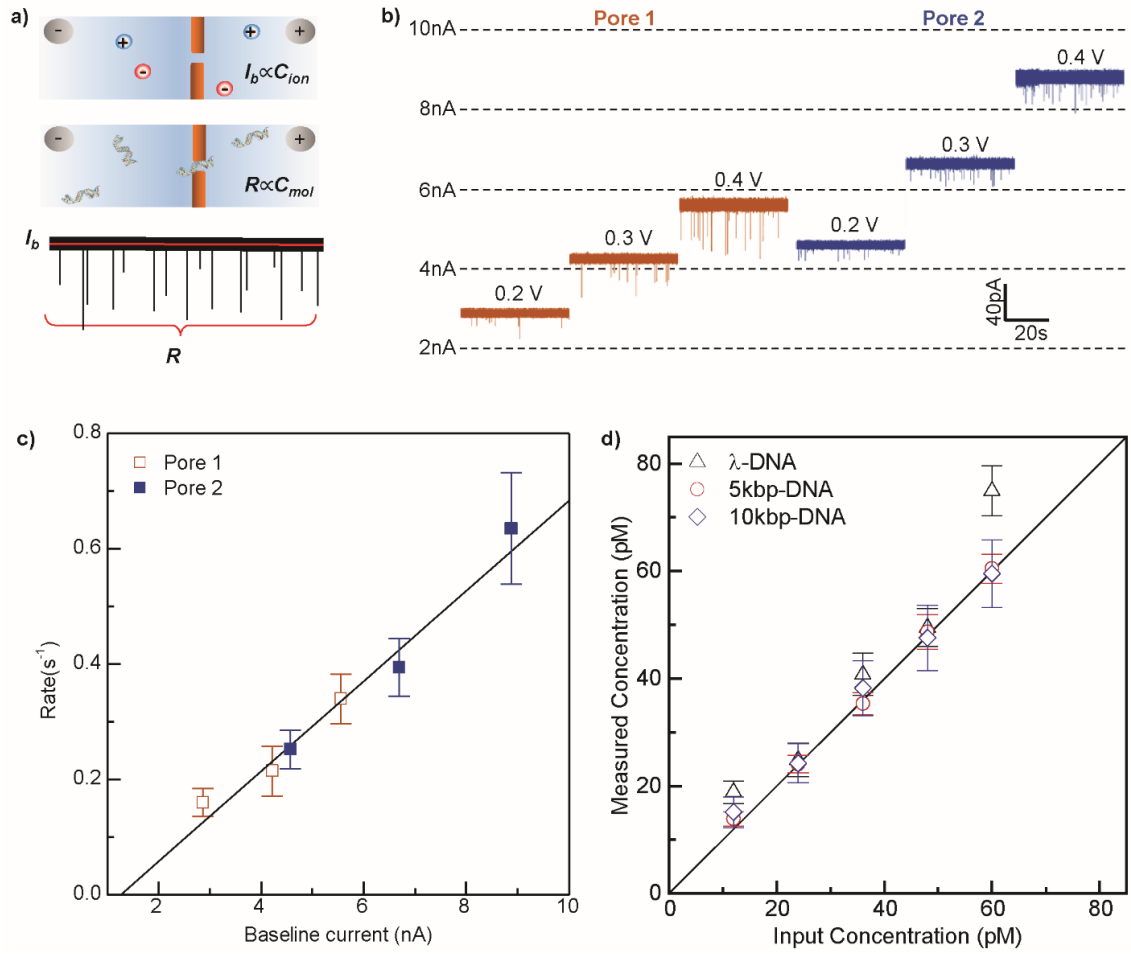

Figure 3-6. a) Schematic of ions and molecules translocation through the same nanopore. The ion and molecule translocation rate is experimentally obtainable from the continuous current readout. b) Current time trace of 24 pM 10 kbp DNA (in 1M KCl) translocating through two different nanopores under different voltages. c) The molecule translocation rate is linearly proportional to the baseline current for the same test sample shown in b. d) Validation of the calibration-free method for concentration determination. The test was performed with different nanopores and DNA molecules with different sizes.

Table 3-1. Summary of calibration-free method for quantifying concentration

Sample	Input concentration(pM)	I_b(nA)	R(1/s)	Measured concentration(pM)*	Error (%)**
λ-DNA	12	6.06	0.26 ± 0.03	18.90 ± 2.07	57.50
	24	5.93	0.34 ± 0.05	24.90 ± 3.11	3.75
	36	6.28	0.58 ± 0.04	40.78 ± 3.92	13.29
	48	8.19	0.92 ± 0.05	49.54 ± 3.54	3.20
	60	8.40	1.43 ± 0.11	74.93 ± 4.65	24.88
5 Kbps DNA	12	3.96	0.13 ± 0.01	13.89 ± 1.27	15.74
	24	4.03	0.22 ± 0.01	24.11 ± 1.64	0.45
	36	4.05	0.33 ± 0.02	35.36 ± 2.07	-1.77
	48	4.03	0.45 ± 0.03	48.70 ± 3.24	1.46
	60	4.46	0.61 ± 0.03	60.49 ± 2.71	0.82
10 Kbps DNA	12	6.21	0.21±0.04	15.15±2.87	26.30
	24	6.21	0.34±0.05	24.22±3.63	0.93
	36	6.27	0.54±0.07	38.23±5.07	6.19
	48	6.83	0.74±0.09	47.59±6.08	-0.85
	60	8.51	1.15±0.12	59.53±6.24	-0.78

* Calculated using Eq. 3.3 with parameters: μ=4.1×10^{-8} m^{2}V^{-1}s^{-1}, Λ =10.86 m^{-1}M^{-1}S, C_{ion}= 1 M
** Error is defined as (Measured-Input)/Input×100%

One important aspect of the nanopore single molecule counting method is the upper and lower bound for concentrations (dynamic range). The upper bound is related to the maximum count rate, which is determined by the speed of the electronic detector and the jamming effect when too many molecules are translocating at the same time[35]. On the other hand, the lower bound (limit of detection) is determined by two factors. The first is the false positive rate when no molecule exists in the testing sample. This is similar to the dark count rate in the single photon counters[118]. This false positive rate determines the minimum count rate at which the signal is dominantly caused by real molecules presented. The false detection events are mostly due to the noise in the testing apparatus. The second factor is the uncertainty in the Poisson rate determination. Since relative

uncertainty of inferring the rate R is proportional to $n^{-1/2}$, a large enough event numbers (N) should be recorded to establish a sufficiently robust statistical basis. With the translocation rate R, a minimal recording time of N/R is thus required. Assuming a practical measurement time of T, a minimal translocation rate N/T is required, which corresponds to the lower bound of the molecule concentration. For example, if we need N to be 200 events and practical experiment time of 30 min, the minimum rate should be around 0.1/s, corresponding to ~10 pM in our experimental setup.

3.4 Summary

In summary, we presented a nanopore single molecule digital counting method for isolated molecule quantification without the need for prior knowledge of experimental conditions such as nanopore geometry, size, and applied voltage. When single molecules were electrophoretically driven through the 10 nm glass nanopore one by one, digital events were registered. We observed that these digital translocation events follow the Poisson distribution, consistent with other types of nanopores[100]. We developed a Poisson statistics-based approach to determine the rate with a certain confidence interval while the experiment is ongoing. We recognized the ionic rates (baseline current) in a particular experiment could be used as an effective *in-situ* reference. We developed a quantitative model for calibration-free quantification of molecule concentration, which was experimentally validated for different nanopores and DNA molecules. It is noteworthy that the method is currently validated in high salt concentration. At low salt concentrations, the electroosmotic flow would start affecting the translocation dynamics[106] and we are performing a systematic study to understand the dynamics in this region. While the results presented in this work were from glass nanopores and DNA molecules, the principle could be well extended to other nanopore types and other charged molecules. We anticipate this calibration-free digital counting approach would provide a new avenue for nanopore sensors.

CHAPTER 4 SEQUENCE-SPECIFIC RECOGNITION OF HIV-1 DNA WITH SOLID-STATE CRISPR-CAS12A-ASSISTED NANOPORE (SCAN)

In this chapter, we demonstrate the use of the glass nanopore for highly sensitive quantification of single-stranded circular DNAs (reporters), which could be degraded under the trans-cleavage activity of the target-specific CRISPR-Cas12a. We developed and optimized the Cas12a assay for HIV-1 analysis. We validated the concept of the solid-state CRISPR-Cas12a-assisted nanopores (SCAN) to specifically detecting the HIV-1 DNAs. We showed that the glass nanopore sensor is effective in monitoring the cleavage activity of the target DNA-activated Cas12a. We developed a model to predict the total experimental time needed for making a statistically confident positive/negative call in a qualitative test. The SCAN concept combines the much-needed specificity and sensitivity into a single platform, and we anticipate that the SCAN would provide a compact, rapid, and low-cost method for nucleic acid detection at the point of care.

4.1 Introduction

Solid-state nanopore sensors made from silicon nitride[29, 30, 64, 119], glass[32, 33, 120], and graphene[121] have shown great potential in detecting single molecules due to their unique label-free electronic sensing, single molecule sensitivity and potential reusability. In typical nanopore experiments, charged biopolymers such as DNAs are electrophoretically driven through the nanoscale orifice, which temporarily blocks the passage of ions that leads to a dip in the current. Each dip in the current indicates one translocation of the analyte through the nanopore, often called an event. The analysis of the event magnitude, shape, duration, and rate provides the basis for interpreting the molecule length, shape, charge, and concentration[122]. Thanks to its elegant

concept, solid-state nanopores have achieved great success in analyzing macromolecules in the past decade. An existing common challenge for solid-state nanopores was the sensing specificity[123]. The typical approach for achieving the specificity is by specific binding sites on the nanopore wall surfaces[124, 125] or using specific probe molecules[126-128]. Nevertheless, additional steps of surface functionalization could limit the device yield[123]. In addition, a specifically modified nanopore means that nanopore can only be used for a fixed target without being generally applicable.

The CRISPR-Cas9 system has shown outstanding competence in targeting nucleic acid with high specificity[129, 130], and has been explored by combining with the nanopore sensings[131-133]. In addition, the recent discovery of the collateral cleavage in other Cas proteins like Cas12 and Cas13 made it possible to translate the sequence-specific targeting to other detectable signals, which has led to the increasing emergence of CRISPR-mediated biosensors[130, 134-140]. For instance, Zhang and colleagues developed SHERLOCK (Specific High sensitivity Enzymatic Reporter unLOCKing), which used RNA-guided RNases Cas13a or Cas13b for RNA detection[136, 137]. In addition, RNA-guided DNase Cas12 was explored for DNA detection, generating multiple versatile systems such as HOLMES[138], DETECTOR[139], and Cas12aVDet[140]. These successes have immensely expanded the applicability of CRISPR/Cas systems for highly specific nucleic acid analysis. So far, most of the CRISPR-mediated bio-sensing applications used fluorescent, bioluminescent, or colorimetric reporters for readouts, which often require optical sensing and additional design and synthesis of reporter molecules like fluorescence/quencher beacons or gold nanoparticles.

In this work, we combined the high specificity offered by the Cas12a and high sensitivity offered by the glass nanopore sensor towards an electronic sensing platform for sequence-specific HIV-1 DNA detection. Cell-associated HIV DNA (CA-HIV DNA, which can be extracted from easily-

obtainable fingerprick blood) is the most widely used marker for HIV persistence in infected cells, the detection of which has significant importance in the diagnosis of HIV infection[141]. The solid-state CRISPR-Cas12a-assisted nanopores (SCAN) use circular single-stranded DNAs (ssDNAs) as reporters, which are cleavable when the crRNA/Cas12 complex (*a.k.a.*, ribonucleoprotein or RNP) is activated by the binding of the specific HIV-1 DNA. We developed Cas12a assay for HIV-1 detection and optimized the buffer conditions for nanopore sensing. We found that the cleavage activity of the target DNA activated RNP can be quantified by the glass nanopore sensors. A model was developed to estimate the optimized reaction time and nanopore reading time such that positive/negative calls in a qualitative test at the 95% confidence level can be made as quickly as possible. We also validated the specificity of the SCAN for detecting two different regions of the HIV-1 gene. With excellent specificity and sensitivity, we believe SCAN offers a promising approach towards developing compact, rapid, and low-cost nucleic acid detection at the point of care.

4.2 Methods

4.2.1 Materials and chemicals.

A.s.Cas12a Ultra (#10001272) and IDTE pH7.5 buffer (#11-01-02-02) were purchased from Integrated DNA Technologies (IDT). dsDNA and crRNA were also synthesized from IDT. M13mp18 ssDNA (#N4040S) and NEBuffer 3.1 (#B7203S) were purchased from NEW ENGLAND Biolabs Inc. (NEB). DNA elution buffer was from Zymo Research (#D4036-5). Nuclease-free molecular Biology grade water was from Hyclone (SH30538). DPBS was purchased from Thermo Fisher (#14190250). DNA gel loading dye (6X) was from Thermo Fisher (#R0611). 10X IDT reaction buffer (200 mM HEPES, 1 M NaCl, 50 mM $MgCl_2$ and 1 mM EDTA,

PH6.5@25°C) was made at the lab. $MgCl_2$, NaCl, KCl and Tris-EDTA-buffer solution (10 mM Tris-HCl and 1 mM EDTA) were purchased from Sigma-Aldrich. HEPES was from Gibco #15630-080. Agarose was from Bio-rad (#1613102). Ethidium Bromide (EB) was from Life Technologies (#15585011). DNA Ladder was from Thermo Scientific (#SM0311). Ag/AgCl wires electrodes were fabricated by using 0.2 mm Ag wires (Warner Instruments, Hamden, USA). Micro injectors of 34 gauge were purchased from World Precision Instruments. Piranha solution was made by mixing concentrated sulfuric acid (H_2SO_4) with hydrogen peroxide (H_2O_2). Quartz capillaries with inner and outer diameter of 0.5 mm and 1 mm were purchased from Sutter Instrument.

4.2.2 HIV-1 Cas12a assay

The crRNAs were resuspended in IDTE pH7.5 buffer and stored in -80 ºC. For RNP formation, Cas12a and crRNA were mixed in 1×PBS to form the non-activated RNP at room temperature for 20 min and stored in -80ºC. In the cleavage reaction, the non-activated RNP complex was mixed with cDNA target and incubated at 37ºC for 10 min for RNP activation. Then ssDNA reporters were added and incubated at 37ºC for cleavage. After the reaction, results were examined both in agarose gel and in the nanopore device. For gel imaging, reactions were terminated with DNA loading dye (6X). The 24 µl mixture was loaded to EB-stained 1% (wt/vol) agarose gel for electrophoresis analysis. For nanopore analysis, reactions were terminated by adjusting the salt concentrations to 1M KCl.

4.2.3 Glass nanopore fabrication

To remove organic residues from quartz capillaries, as-purchased quartz capillaries were firstly cleaned in Piranha solution for 30 minutes, then rinsed with DI water, and dried in a vacuum oven

at 120 ºC for 15 min. A two-line recipe, (1) Heat 750, Filament 5, Velocity 50, Delay140, and Pull 50; (2) Heat 710, Filament 4, Velocity 30, Delay 155, and Pull 215, was used to pull the capillaries with a laser pipette puller (P-2000, Sutter Instruments, USA). This recipe typically produces nanopores of diameter around 10 nm. It is noteworthy that ssDNA that is less than 1kbp length does not generate detectable signal in the glass nanopore.

4.2.4 Nanopore sensing and data analysis

A constant voltage was applied across the glass nanopore by 6363 DAQ card (National Instruments, USA). A transimpedance amplifier (Axopatch 200B, Molecular Device, USA) was used to amplify the resulting current and then digitalized by the 6363 DAQ card at 100 kHz sampling rate. Finally, a customized MATLAB (MathWorks) software was used to analyze the current time trace and extract the single molecule translocation information.

4.3 Working Principle

Figure 4-1 illustrates the working principle of SCAN for sequence-specific DNA detection. It leverages the unique features of the CRISPR-Cas12a and the nanopore sensor. Upon the specific RNA-guided dsDNA binding, the Cas12a could perform collateral cleavage on the surrounding nonspecific ssDNAs. This feature has been previously utilized for developing diagnostic tools[135, 138-140, 142]. In SCAN, circular ssDNAs (M13mp18, 7249 bases) of a known concentration (typically 100 pM) were used as reporters. If target HIV-1 DNAs exist in the analyte solution (**Figure 4-1a**), the Cas12a/crRNA complex (*i.e.*, non-activated RNP) can be activated by binding specifically to the target HIV-1 DNAs. The activated RNP was then able to digest the ssDNA reporters. During this process, the effective concentration of the circular ssDNA reporter was

reduced. On the other hand, if the target HIV-1 DNAs do not present in the analyte solutions (**Figure 4-1b**), the RNP complex remains inactive and will not degrade the ssDNA reporter. As a result, the abundance of the remaining circular ssDNA reporter indicates the existence/absence of the target DNAs. The SCAN approach used the glass nanopores for electronic quantification of the remaining ssDNA reporter through the single molecule counting[43, 120, 143]. The existence of the target HIV-1 DNAs would significantly reduce the ssDNA reporter event rate through the nanopore sensors.

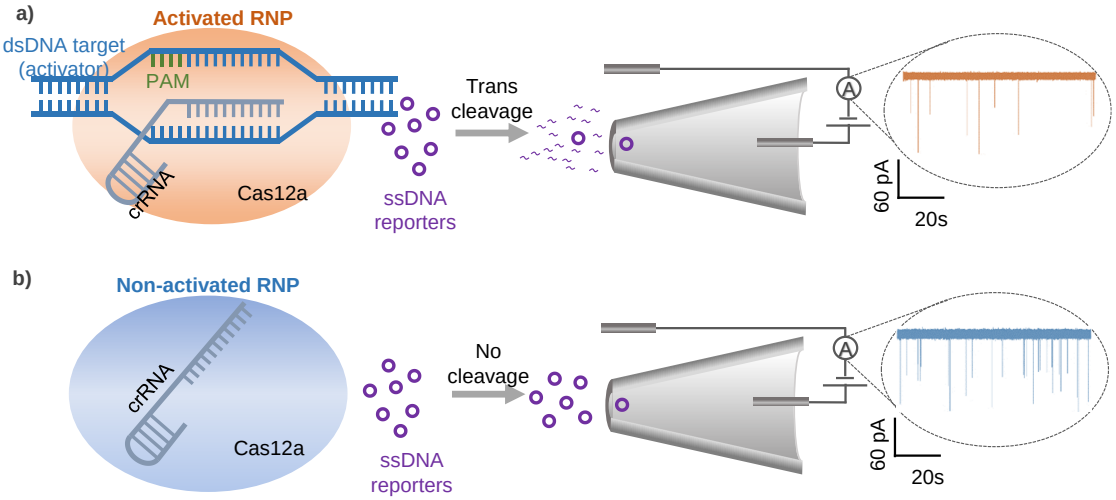

Figure 4-1. Schematic of Solid-State CRISPR-Cas12a-Assisted Nanopore (SCAN) sensor. a) Positive case, the trans-cleavage activity of the Cas12a after activation cause degradation of the circular ssDNA reporters, resulting in reduced reporter event rate through the nanopore. b) Negative case, the Cas12a is not activated in the absence of target dsDNA and thus the ssDNA

It is noteworthy that while the remaining ssDNA reporter can be readily visualized by conventional gel electrophoresis, the nanopore readout is much more sensitive and can be performed in-situ (**Figure 4-2**). Due to the superior single molecule sensitivity of the nanopore, the ssDNA reporter concentration we used in SCAN (typically 100 pM) is much smaller than that in fluorescent platforms (typically 100 nM). To ensure all events observed in the nanopore sensors correspond to the ssDNA reporter rather than the interfering background molecules (*e.g.*, RNPs), we performed

nanopore experiment for a pure RNP and HIV-1 DNA sample (30 nM each) without any ssDNA reporter. We did not observe a single event for a measurement time of 1000 s (**Figure 4-3**), which confirms that the translocation rate of the background activated RNPs is less than 0.001 s^{-1}. The lack of signals from RNPs is most likely due to the fact that the size of the RNP complex and target DNA is much smaller than the circular reporter ssDNAs (7249 bases), which cannot be picked up by the large nanopores of a diameter of 10 nm.

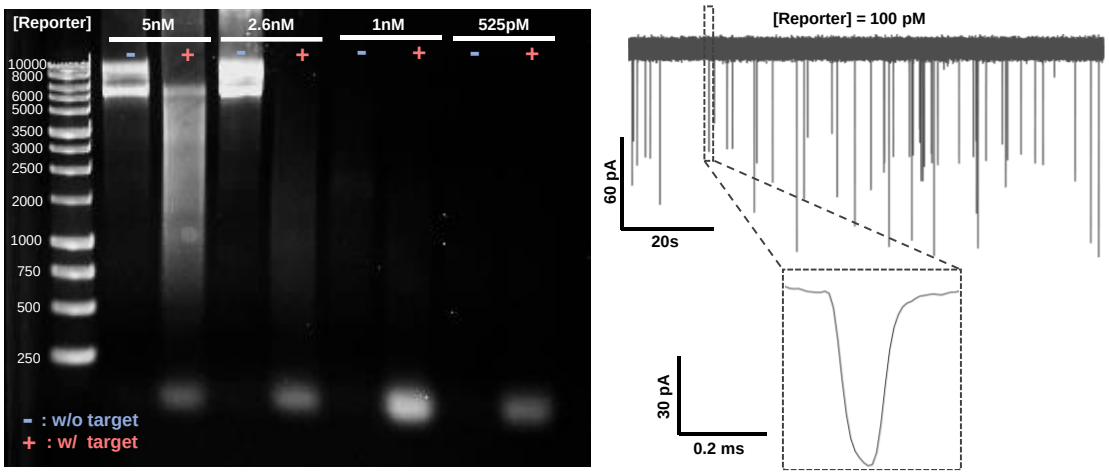

Figure 4-2. Comparison between the sensitivity of traditional gel electrophoresis and nanopore sensor in the detection of reporter residue. Reporter ssDNAs with a concentration lower than 1 nM cannot be detected by the gel images. On the other hand, the nanopores sensor shows higher sensitivity where 100 pM of ssDNA reporters can be easily detected. The magnified view of the current trace illustrated a typical single molecule translocation event.

Figure 4-3. Nanopore experiment for a pure RNP and HIV targets sample (30 nM) without any ssDNA reporter. We did not observe a single event for a measurement duration time of 1000 s, which confirms that the translocation rate of the background activated RNPs is less than 0.001 s^{-1}.

4.4 Results and discussion

4.4.1 HIV-1 Assay and Buffer Optimization

For sequence-specific recognition of HIV-1 DNA, the crRNAs should target conserved regions in all HIV-1 subtypes. To this end, we focused on three commonly evaluated domains of HIV-1, which are GAG (capsid protein), POL (protease, reverse transcriptase and integrase), and ENV (glycoprotein) [144-146]. Base on this information, we synthesized two 50 bp dsDNAs from the GAG region as our HIV-1 targets. Two specific crRNAs were designed for each of these dsDNAs targets (see Methods for detailed sequences).

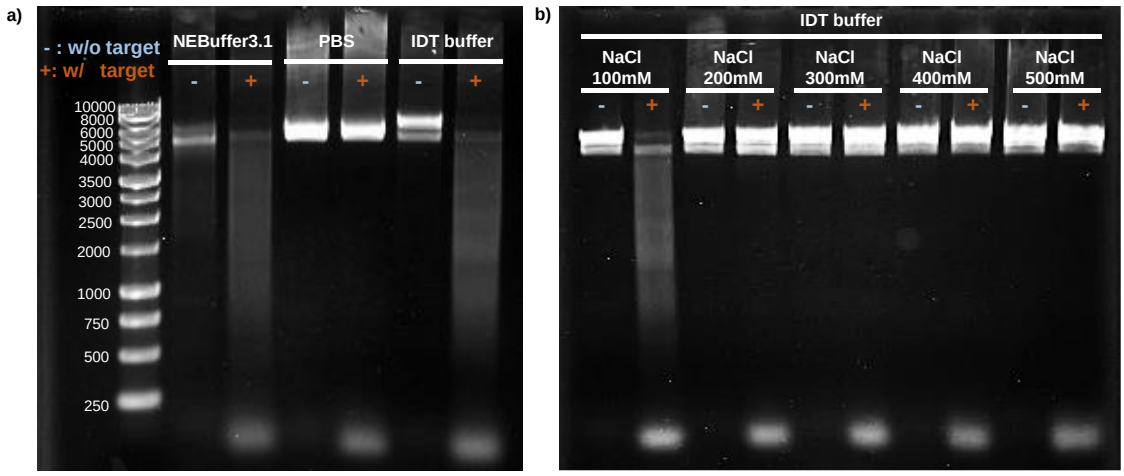

Figure 4-4. Buffer optimizing for HIV-1 Cas12a assay. a) Evaluating three candidate buffers: NEBuffer 3.1, PBS buffer and IDT buffer. b) Evaluating the impact of salt concentration on the Cas12a activity in the IDT buffer.

Towards a glass nanopore compatible reaction buffer[131, 132], we explored three candidates: NEBuffer 3.1, PBS buffer and IDT buffer. The gel analysis was performed to validate each of these buffers (**Figure 4-4a**). As shown, the commonly used NEBuffer 3.1[138, 140, 147] indeed worked in our HIV-1 Cas12a assay. However, it is incompatible with the nanopore sensor. The presence of high concentrated (1.5 μM) Bovine Serum Albumin (BSA) in the NEBuffer acts as an opposing

obstacle for ssDNA reporters and dramatically impact the nanopore ssDNA reporter event rates. For the PBS buffer, the gel results showed that it did not support the cleavage activity of Cas12a. This is likely due to the lack of Mg^{2+} ions, the key co-factor in Cas12a enzymatic activities[148].

We hypothesized that a buffer with Mg^{2+} ions that has no BSAs is desirable for The SCAN device. The IDT buffer is such a candidate. We validated its functionality for our HIV-1 Cas12a assay. While Cas12a indeed functioned properly in the IDT buffer, the low salt concentration of the buffer (100 mM) is non-ideal for the nanopore sensing[51]. It was previously shown that high salt concentration would be favorable for nanopore sensing as the low salt concentration will result in a dramatic reduction of event rate and the signal in glass nanopores[143, 149]. To this end, we evaluated how increasing the salt concentration in the IDT buffer would impact the Cas12a assay. It was found that 200 mM salt would start killing the activity of the Cas12a (**Figure 4-4b**). This indicates the IDT buffer with 100 mM salt should be used in the HIV-1 Cas12a reaction. To solve the conflicting buffer requirements in the Cas12a reaction (low salt) and the nanopore sensing (high salt), we used a two-step protocol in our SCAN system. The reaction between the target DNA, Cas12a/crRNA, and ssDNA reporter was performed in the IDT buffer. The reaction was then terminated by adding 1.045 M KCl solution such that the final salt concentration is 1 M for efficient nanopore counting of the remaining ssDNA reporter. Nanopore Event Rate for Circular ssDNA Reporters Quantification.

For a typical SCAN experiment, the RNP concentration remains constant during the Cas12a cleavage reaction. To validate if the nanopore event rate can be used as a quantitative readout for the ssDNA reporter concentration at the constant RNP background, we performed nanopore counting experiments with serially diluted ssDNA reporter. In all experiments, the RNP and salt concentration was fixed as 30 nM and 1 M, respectively. **Figure 4-5a** shows the time traces of the ionic current from each of these cases. A quick glance of these traces revealed that events occur

more often as the ssDNA reporter concentration increases. The extracted event rate as a function of the reporter concentration was plotted in **Figure 4-5b**. A clear linear relationship between the event rate and the ssDNA reporter concentration was observed ($R^2 = 0.98$), which validates the abundance of ssDNA reporter can be quantified by nanopore counting at the constant RNP background.

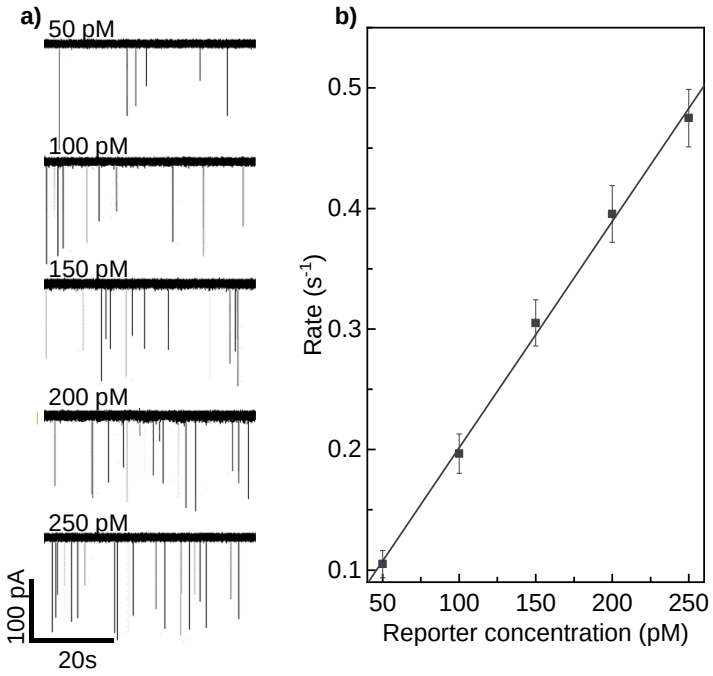

Figure 4-5. Quantitative ability at constant RNP concentrations. a) Translocation recording of serially-diluted ssDNA reporters ranging from 50-250 pM through the glass nanopore under 400 mV bias. The RNP and buffer salt concentration was fixed as 30 nM and 1 M, respectively. b) The nanopore event rate as a function of the ssDNA reporter concentrations. The error bars correspond to the Poisson noise of determining the event rate.

4.4.2 HIV-1 Activated Cas12a Trans-Cleavage Monitored by Nanopore Counting

After verifying the linear relationship between the ssDNA reporter and the nanopore event rate under the constant RNP, we set out to perform the HIV-1 sensing using the SCAN. Three different HIV-1 concentrations (15, 30, and 60 nM) were tested by adding the dsDNA sample to the RNP

solutions in the IDT buffer. In all the experiments, the initial ssDNA reporter concentration was fixed at 100 pM. The reaction was terminated at various reaction times (0, 5, 10, 20, and 30 minutes) by adding KCl salt to the final salt concentration of 1M. The remaining ssDNA reporter concentration was measured by the calibration-free nanopore counting method [43].

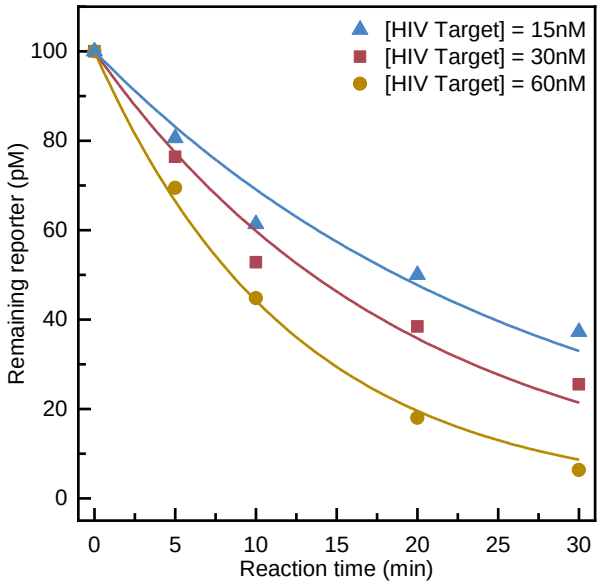

Figure 4-6.. Remaining ssDNA reporter concentration as a function of reaction time (0, 5, 10, 20, and 30 minutes) for different HIV target concentrations (15, 30, and 60 nM). In each case, the initial ssDNA reporter concentration was set as 100 pM and the remaining concentration was obtained using the extracted translocation rate through the nanopore. The solid line is the fitting using the Michaelis–Menten kinetics, $C = C_0 e^{-kT_r}$, where C0 is the initial ssDNA reporter concentration (100 pM). The fitted rate constants k for 15, 30, and 60 nM target HIV was obtained as 0.037, 0.051, and 0.081 min-1 respectively.

Figure 4-6 plots the remaining ssDNA reporter concentration as a function of the reaction time for different target HIV-1 concentrations. For each target HIV-1 concentration, the ssDNA reporter concentration reduced exponentially and can be well fitted by the Michaelis–Menten kinetics, $C = C_0 e^{-kT_r}$, where C and C_0 are the remaining and initial ssDNA reporter concentration, respectively. T_r is the reaction time and k is the rate constant. The rate constant k went up from 0.037 min^{-1} at 15 nM target HIV to 0.051 min^{-1} at 30 nM target HIV, and further to 0.081 min^{-1} at

60 nM target HIV. These trans-cleavage rate constants were in par with previously reported value of 0.03 min^{-1} [150]. It was evident that the more target HIV-1 present in the analyte solution, the faster the ssDNA reporters get degraded by the activated Cas12a.

Although some of the translocation events recorded in the nanopore sensing could come from the partially cleaved ssDNA reporter, the fact that the extracted remaining reporter decay exponentially by the reaction time (**Figure 4-6**) and follow the Michaelis-Menten kinetics suggested that the interference from the partially cleaved ssDNA reporter is negligible. To further explore the impact of the partially cleaved DNAs, we evaluated the distributions of the current dips, dwell time, and event charge deficits (ECDs) of the events for a negative sample and positive samples (**Figure 4-7**). No significant difference was observed between these two samples, indicating most of the detected events were from the intact circular ssDNA reporter.

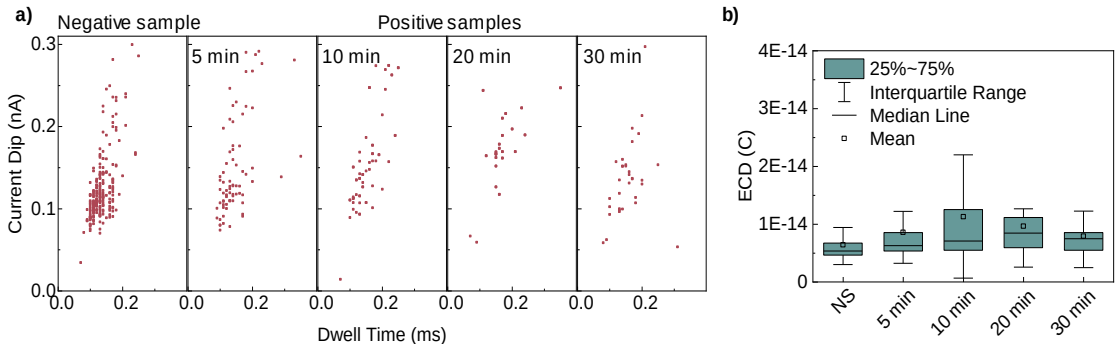

Figure 4-7. a) Scatter plots showing current dip magnitude vs. dwell times for a negative sample and positive samples (30 nM HIV-1) with different cleavage time (5, 10, 20, and 30 minutes). This data illustrates that the distribution of the current dip and dwell times do not change after cleavage. Hence, we can claim that the effect of the cleaved DNAs on the nanopore sensing is negligible. b) The box plot of the event charge deficits (ECD) for all cases, which shows that the ECD distribution does not change significantly from the negative sample to the positive samples.

4.4.3 Statistical Modeling for Qualitative Positive/Negative Test in SCAN

Practically, the SCAN device would require a certain reaction time T_r such that the HIV-1 activated Cas12a could degrade a certain amount of ssDNA reporters. The longer the reaction time, the less the remaining reporters. Subsequently, the remaining reporters will be measured by the nanopore counting within a measurement time of T_m. It was previously shown that the translocation of molecules through the nanopore is a Poisson process[100]. Thus inferring the event rate from observing n events in T_m will have an uncertainty of $(1.96(n)^{1/2})/T_m$ [151]. In other words, longer measurement is statically beneficial for more accurate rate determination. As a result, longer reaction time T_r and measurement time T_m is preferred to make a statistically confident call for a qualitative positive/negative test. However, minimizing the total experimental time (T_r+T_m) would be highly desirable towards a fast sample-to-result turnaround.

In order to estimate the total experimental time for a qualitative positive/negative test, we developed a statistical model. For the negative case (*i.e.*, no reporter degradation), the expected number of events in the nanopore in a measurement time of T_m is given by

$$\lambda_n = \alpha\mu C_0 T_m \quad (4.1)$$

where μ is the electrophoretic mobility of the ssDNA reporter, α is a constant, and C_0 is the initial ssDNA reporter concentration before the reaction. On the other hand, for the positive case after reaction time T_r, the initial reporter concentration C_0 would decrease to $C_0 e^{-kT_r}$ (Michaelis-Menten kinetics) and the expected number of events in the nanopore in a measurement time of T_m would be:

$$\lambda_p = \alpha\mu C_0 e^{-kT_r} T_m \quad (4.2)$$

in which *k* is the rate constant that is linearly proportional to the activated RNP concentration. The activated RNP concentration is limited by the smaller values between HIV-1 DNA and RNP concentration in the system and can be written as

$$k = A \times min(C_{HIV}, C_{RNP}) \quad (4.3)$$

where A is a constant (0.00148 $min^{-1}nM^{-1}$).

In our experiment, we found that while the RNP complexes do not produce measurable events, they do affect the electrophoretic mobility of the ssDNA reporters. It was found the reporter electrophoretic mobility reduces exponentially as we increase the RNP concentration (**Figure 4-8**).

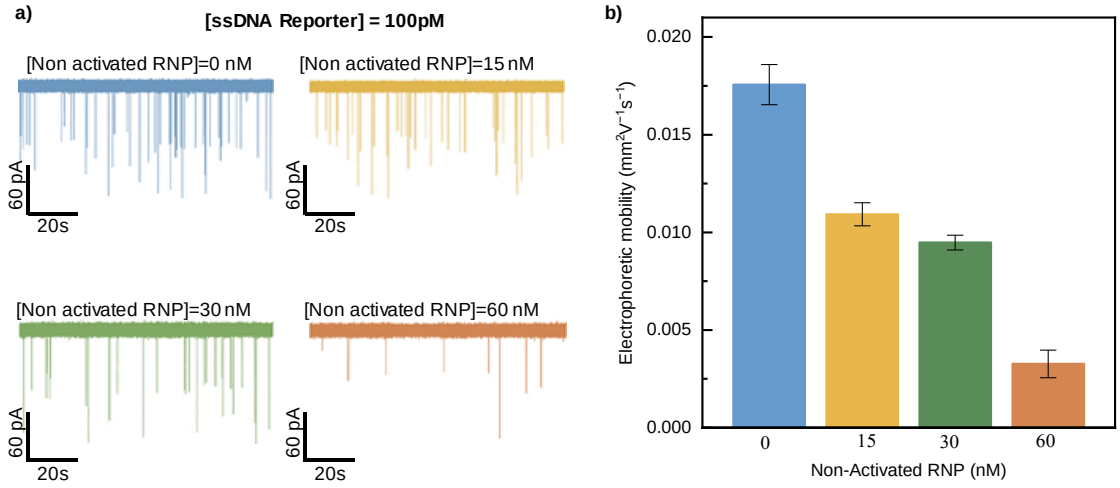

Figure 4-8. RNP concentration effect on the electrophoretic mobility of ssDNA reporters. a) Translocation recording of ssDNA through glass nanopore at four RNP concentrations (0, 15, 30, and 60 nM) under 400 mV bias. All experiments were performed at 1 M salt concentration and ssDNA concentration was fixed at 100 pM. b) Extracted ssDNA reporter electrophoretic mobility as a function of the background RNP concentration.

This phenomenon was previously observed in gel electrophoresis and was described by the Ogston-Morris-Rodbard-Chrambach model, in which molecule electrophoretic mobility has an exponential relationship with the obstacles concentration ($\mu \propto e^{-C_{RNP}}$) [152, 153]. Hence, electrophoretic

mobility of the reporters can be extracted by fitting an exponential curve to our experimental results:

$$\mu = \mu_0 e^{-\beta C_{RNP}} \qquad (4.4)$$

where μ_0 (1.73×10^{-8} $m^2V^{-1}s^{-1}$) and β (0.025 nM^{-1}) are the constants of the fitted exponential curve to the experimental results. Experimentally observed events for negative and positive case would follow the Poisson distribution with expected values of λ_n and λ_p respectively. As illustrated in **Figure 4-9a**, we aim to find out the λ_p such that the overlap of Poisson probability density functions (PDF) to that of the negative case of λ_n is less than 5% (*i.e.*, 95% confidence level for making a positive/negative call). For any fixed nanopore reading time T_m, we can solve the maximal λ_p and therefore the minimal required reaction time T_r. **Figure 4-9b** plots the total experimental time (T_r+T_m) as a function of HIV and RNP concentrations. We observed three important features.

First, under a fixed RNP concentration, the total experimental time can be significantly reduced when HIV target concentration is increased up to that of RNP concentration, beyond which the total experimental time is independent of the HIV-1 target concentration. This is because the rate constant *k* is determined by the smaller amount between target HIV-1 and RNP. Second, although in regions where RNP concentration is higher than HIV-1, the constant rate k is independent of RNP concentration, the total experimental time would be significantly increased when RNP target concentration is increased, especially more than 50 nM regions. This stems from the fact that the electrophoretic mobility of the reporters decays exponentially as we increase the RNP concentration (Eq. 4.4). Hence, we need more time in the nanopore reading to make a call at 95% confidence.

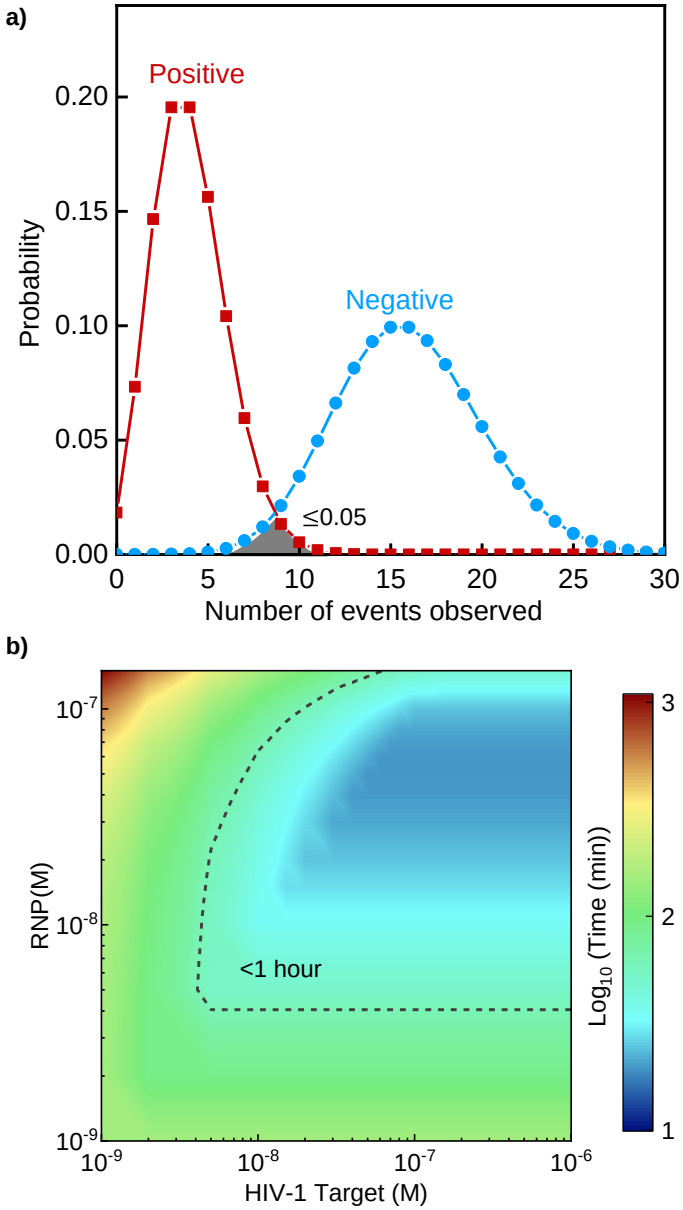

Figure 4-9. a) Illustration of distributions for event numbers observed in the negative and positive case. The overlap of the two distributions should be less than 5% for a positive/negative call at the 95% confidence level. b) The total experimental time needed for making a positive/negative call at different combinations of HIV target and RNP concentrations. The dashed dotted line indicates the region in which the qualitative call can be made within 1 hour.

Third, an optimized combination of HIV-1 and RNP concentration is required such that a positive/negative call at 95% confidence can be made within an hour (dashed line). It was found that the RNP concentration between 10-100 nM and HIV target concentration higher than 10 nM

would be the optimized range in our experiment. If the starting HIV-1 DNA concentration is less than 10 nM, a pre-amplification step before SCAN is highly desirable for quick turnaround. These pre-amplification steps were widely used in previous Cas12a based assays[139, 140, 142].

4.4.4 Sequence-Specific Test

We designed two sets of HIV-1 DNA targets and assays, in which each assay was specific to its target (Assay 1 to Target 1 and Assay 2 to Target 2). To test the cross-reactivity of designed assays, we performed the gel analysis on the assay products. **Figure 4-10a** showed the gel image. We observed clear reporter cleavage when the assays were used to their specific target, and no reporter cleavage if the assay is non-specific to the target. To validate the specificity of the SCAN, we tested four different assay-target combinations.

Figure 4-10b-e presents the results of the nanopore experiment before and after 30 min of reaction. For Target 1 in Assay 1, the translocation event rate change is significant (from 0.329±0.036 s^{-1} to 0.128±0.022 s^{-1}), whereas for Target 1 in Assay 2, the event rate change is negligible (from 0.271±0.034 s^{-1} to 0.258±0.032 s^{-1}). Similarly, for Target 2 in Assay 1, the translocation event rate change is negligible (from 0. 310±0.035 s^{-1} to 0. 308±0.039 s^{-1}), whereas Target 2 in Assay 2, the translocation event rate change is significant (from 0.326±0.037 s^{-1} to 0.103±0.022 s^{-1}). It is clear that only the matched Cas12a assay and its target can produce a significant reduction in the number of translocation events after 30 minutes of reaction. These results demonstrated the SCAN could detect targets specifically. While nanopore sensors were often challenged by the specificity issue, we believe coupling the extremely high specificity of CRISPR Cas 12a to the nanopore sensor can provide an appealing alternative for future applications.

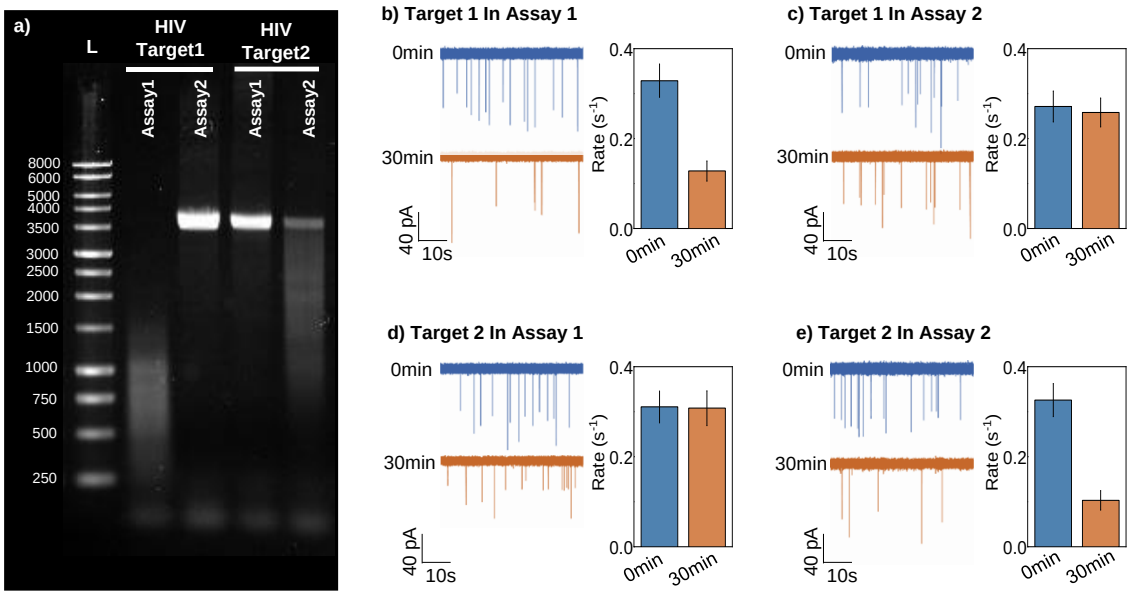

Figure 4-10. a) Agarose gel electrophoresis images of the designed specificity test. Only specific combinations (Assay 1-Target 1, and Assay 2-Target 2) lead to the degradation of reporters. b-e) Specificity test in SCAN. The reaction time for all cases is 30 minutes and the HIV target concentration is 30 nM. Only matched Cas12a assay and its target can produce a significant reduction in the number of translocation events. The error bars correspond to the Poisson noise of determining the event rate.

4.5 Summary

In summary, our findings demonstrated the capabilities of solid-state CRISPR-Cas12a-assisted nanopores for highly sensitive and specificity HIV-1 DNA detection. We found that the buffer salt concentration plays a critical role in both the assay and nanopore readout. We verified the events observed in the nanopore sensors were dominated by the un-cleaved circular ssDNA reporter, rather than the background interference. The nanopore translocation event rate is a valid readout for quantifying the ssDNA reporters in the presence of the RNP complexes. We found the reporter

cleavage rate constant is proportional to the target HIV-1 concentration. We developed a model to estimate the optimized reaction time and nanopore reading time such that positive/negative calls in a qualitative test at the 95% confidence level can be made as quickly as possible. We found that SCAN can detect target DNA concentrations above 10 nM within 1 hour. Concentration less than 10 nM would likely require pre-amplification steps, similar to previous Cas12a based assays [139, 140, 142]. We also validated the specificity of the SCAN for detecting two different regions of the HIV-1 gene. While the results presented in this work were from glass nanopores and HIV-1 DNAs, the SCAN principle could be well extended to other nanopore types and DNA targets. We anticipate that SCAN would provide a new avenue for molecular diagnostic applications.

CHAPTER 5 DETECTION OF SARS-COV-2 WITH SOLID-STATE CRISPR-CAS12A-ASSISTED NANOPORES (SCAN)

In this chapter, we present a solid-state CRISPR-Cas12a-assisted nanopore (SCAN) sensing strategy for the specific detection of SARS-CoV-2. We introduced a nanopore-sized counting method to measure the cleavage ratio of reporters, which is used as a criterion for positive/negative classification. A kinetic cleavage model was developed and validated to predict the reporter size distributions. The model revealed the tradeoffs between sensitivity, turnaround time, and false-positive rate of the SARS-CoV-2 SCAN. With a preamplification and 30 min of CRISPR Cas12a assay, we achieved excellent specificity against other common human coronaviruses and a limit of detection of 13.5 copies/μl (22.5 aM) of viral RNA at the 95% confidence level. These results suggested that the SCAN could provide a rapid, sensitive and specific analysis of SARS-CoV-2.

5.1 Introduction

The coronavirus disease 19 (COVID-19) caused by the severe acute respiratory syndrome coronavirus 2 (SARS-CoV-2) is an ongoing pandemic throughout the world [154, 155]. To facilitate the management and containment of the disease, reliable, rapid, and accessible testing is required. While numerous diagnostic strategies such as sequencing [156-159] and antibody test [160-162] have been introduced for SARS-CoV-2 detection, nucleic acid testings (NAT), primarily quantitative real-time PCR with reverse transcription (RT-qPCR), are the current gold standards [163, 164]. The recent development of the clustered regularly interspaced short palindromic repeats (CRISPR)-based methods started a new path towards molecular diagnosis [165]. Particularly, the discovery of the collateral cleavage of Cas proteins such as Cas12 and Cas13 made it possible to translate the sequence-specific targeting to detectable signals. These discoveries have led to a

variety of CRISPR-mediated biosensors [130, 136-138, 166-170]. These CRISPR-based methods often incorporate an amplification process such as polymerase chain reaction (PCR) [171, 172], loop-mediated isothermal amplification (LAMP) [173], or recombinase polymerase amplification (RPA) [174, 175] to enhance the starting molecule population [137, 176]. Amplification coupled CRISPR-Cas detection has been shown to be highly sensitive (as low as fM level [136, 137]) and highly specific (down to single-nucleotide level [177, 178]). Due to their outstanding sensing performances, CRISPR-based systems have been adopted for SARS-CoV-2 detection amid the ongoing COVID-19 pandemic [163, 172, 179-187].

So far, most of the CRISPR-based methods use fluorescent, bioluminescent, or colorimetric reporters for readouts, which is easy to operate, sensitive and convenient [188]. As alternatives to the optical readout, electronic-based methods such as electrochemical [167, 189-191], and field-effect [192] have also been investigated due to their integration and miniaturization potential. One of the intriguing electronic readout systems utilized for CRISPR-based detection is the nanopore sensor [131, 132]. The single molecule sensitivity of the nanopore sensors has made them a promising candidate for CRISPR-based detection. We previously demonstrated a solid-state CRISPR-Cas12a-assisted nanopore (SCAN) sensor for sequence-specific recognition of HIV-1 [193]. While we demonstrated that the SCAN can detect target DNA concentrations above 10 nM within an hour, detecting concentrations less than 10 nM with a fast turnaround time would likely require pre-amplification steps.

In this work, we developed a reverse transcription amplification coupled SCAN device for rapid, highly sensitive, and highly specific detection of SARS-CoV-2 viral RNAs. The method used an improved nanopore sized counting approach to examine the reporter size distributions and their relative abundance. We showed that the cleavage ratio of the intact circular ssDNA reporters could be quantified by the SCAN, which is used as a criterion for classifying the test as positive or

negative. To guide the experiments, we developed a kinetic model to compute the reporter length distribution as a function of the cleavage reaction time. This experimentally validated model revealed the tradeoffs between sensitivity, turnaround time, and false-positive rate of the SARS-CoV-2 SCAN. With a preamplification and 30 min of CRISPR Cas12a assay, we achieve a limit of detection (LoD) of 13.5 copies/µl (22.5 aM) of SARS-CoV-2 viral RNA at the 95% confidence level. The SARS-CoV-2 SCAN has also shown excellent specificity against three other common human coronaviruses. Our results suggested that the SCAN could provide a rapid, sensitive, and specific analysis of SARS-CoV-2.

5.2 Methods

5.2.1 Materials and chemicals

A.s.Cas12a Ultra (#10001272) and primers were purchased from Integrated DNA Technologies (IDT). crRNA was synthesized by IDT. qScript™ XLT One-Step RT-qPCR Tough Mix was purchased from Quantabio. M13mp18 ssDNA (#N4040S) was purchased from NEW ENGLAND Biolabs Inc. (NEB). The heat-inactivated SARS-CoV-2 viral RNA was from ATCC (ATCC® VR-1986HK™). The synthetic human coronavirus RNA controls were purchased from Twist Bioscience (Twist Bioscience, 103011, 103012, and 103013). DNA gel loading dye (6X) was from NEB (#B7024S). 10X Cas12a reaction buffer (200 mM HEPES, 1 M NaCl, 50 mM $MgCl_2$ and 1 mM EDTA, PH6.5@25°C) was made at the lab. $MgCl_2$, NaCl, KCl, and Tris-EDTA-buffer solution (10 mM Tris-HCl and 1 mM EDTA) were purchased from Sigma-Aldrich. HEPES was from Gibco #15630-080. Agarose was from Bio-rad (#1613102). Ethidium Bromide (EB) was from Life Technologies (#15585011). DNA Ladder was from Thermo Scientific (#SM0311). Ag/AgCl wires electrodes were fabricated by using 0.2 mm Ag wires (Warner Instruments, Hamden, USA). Micro

injectors of 34 gauge were purchased from World Precision Instruments. Piranha solution was made by mixing concentrated sulfuric acid (H_2SO_4) with hydrogen peroxide (H_2O_2). Quartz capillaries with inner and outer diameters of 0.5 mm and 1 mm were purchased from Sutter Instrument.

5.2.2 SARS-CoV-2 RT-PCR assay

We used the CDC primers targeting the N2 region of the SARS-CoV-2 (Forward primer: TTACAAACATTGGCCGCAAA, Reverse primer: GCGCGACATTCCGAAGAA) with a target product length of 67 bp. The 20 µl of the RT-PCR master mix consist of 5 µl of heat-inactivated SARS-CoV-2 viral RNA (for SARS-CoV-2 Cas12a assay validation 2×10^5 copies/µl, and for analytical sensitivity test different concentrations ranging from 2 to 200 copies/µl were used), 1.5 µl of primer/probe mix (50 µM forward primer, 50 µM reverse primer, 20 µM probes), 10 µl of qScript™ XLT One-Step RT-qPCR Tough Mix, and 3.5 µl of H_2O. It should be noted that different concentrations of RNA were prepared by diluting the stock concentration (2×10^5 copies/µl) with ultra-pure DNase/RNase-free distilled water. The RT-PCR was performed for 45 cycles in a Bio-Rad CFX96 Deep Well Real-Time PCR detection system. Each cycle consists of 3 seconds denaturation step at 95 °C and 30 seconds annealing step at 55 °C.

5.2.3 SARS-CoV-2 Cas12a assay

The crRNA was synthesized by Integrated DNA Technologies, and its sequence was: 5'-UAAUUUCUACUCUUGUAGAUCCCCCAGCGCUUCAGCGUUC-3'. The crRNAs were resuspended in pH 7.5 buffer and stored in -80 ºC. Cas12a and crRNA were mixed in 1×PBS to form the non-activated Cas12a/crRNA at room temperature for 20 min and stored at -80ºC. In the

cleavage reaction, the 2 µl of non-activated Cas12a/crRNA complex was mixed with the 1 µl of cDNA target in 14.5 µl of water, and 3.5 µl of a buffer consisting of 100 mM NaCl, 5 mM MgCl2, 20 mM HEPES, and 0.1 mM EDTA and incubated at 37ºC for 10 min for Cas12a activation. Afterward, ssDNA reporters were added and incubated at 37ºC for cleavage. After the reaction, results were examined both in agarose gel and in the nanopore sensor. For gel imaging, reactions were terminated with 4 µl of DNA loading dye (6X). The 24 µl mixture was loaded to EB-stained 1% (wt/vol) agarose gel for electrophoresis analysis. For nanopore analysis, reactions were terminated by adjusting the salt concentrations to 1 M KCl.

5.2.4 Glass nanopore fabrication and characterization

The quartz capillaries were cleaned in Piranha solution for 30 minutes, then rinsed with DI water, and dried in a vacuum oven at 120 ºC for 15 min. This process was performed to remove organic residues from quartz capillaries. A two-line recipe, (1) Heat 750, Filament 5, Velocity 50, Delay140, and Pull 50; (2) Heat 710, Filament 4, Velocity 30, Delay 155, and Pull 215, was used to pull the capillaries with a laser pipette puller (P-2000, Sutter Instruments, USA). A current-voltage experiment was performed to characterize the nanopores by changing the voltage from -400 to 400 mV. A typical nanopore used in this study has a diameter around 10 nm.

5.2.5 Nanopore sensing and data analysis

A constant voltage was applied across the glass nanopore by a 6363 DAQ card (National Instruments, USA). A transimpedance amplifier (Axopatch 200B, Molecular Device, USA) was used to amplify the resulting current. The amplified voltage was digitalized by the 6363 DAQ card at a 100 kHz sampling rate. Finally, a customized MATLAB (MathWorks) software was used to

analyze the current time trace and extract the single molecule translocation information (dwell time, current drop, and ECD).

5.3 Working Principle

Figure 5-1a illustrated the working scheme of the SARS-CoV-2 SCAN using nanopore sized counting. There were three streamlined steps: reverse transcription and amplification, Cas12 assay, and nanopore-based molecule classification and counting. In the first step, a one-step reverse transcription-polymerase chain reaction (RT-PCR) of SARS-CoV-2 RNA was performed to improve the overall sensitivity of the system [180, 181, 183]. After amplification, the complementary DNA (cDNA) amplicons were introduced to the sequence-specific CRISPR RNA (crRNA) and Cas12a ribonucleoprotein mixture (*a.k.a*, RNP).

Upon the specific cDNA binding, the Cas12a could perform collateral cleavage on the surrounding ssDNA reporters [139]. We used circular M13mp18 single-stranded DNA (ssDNA) as the reporter in this study which is widely available and has an excellent signal-to-noise ratio in nanopore measurement. In the trans-cleavage process, the mother circular ssDNA reporters could be digested into daughter linear ssDNAs, and the daughter reporters could be further digested into granddaughter reporters (positive case in **Figure 5-1a**). On the other hand, if SARS-CoV-2 viral RNAs were not present in the analyte solutions, the Cas12a remains inactive and will not degrade the mother circular ssDNA reporter (negative case in **Figure 5-1a**).

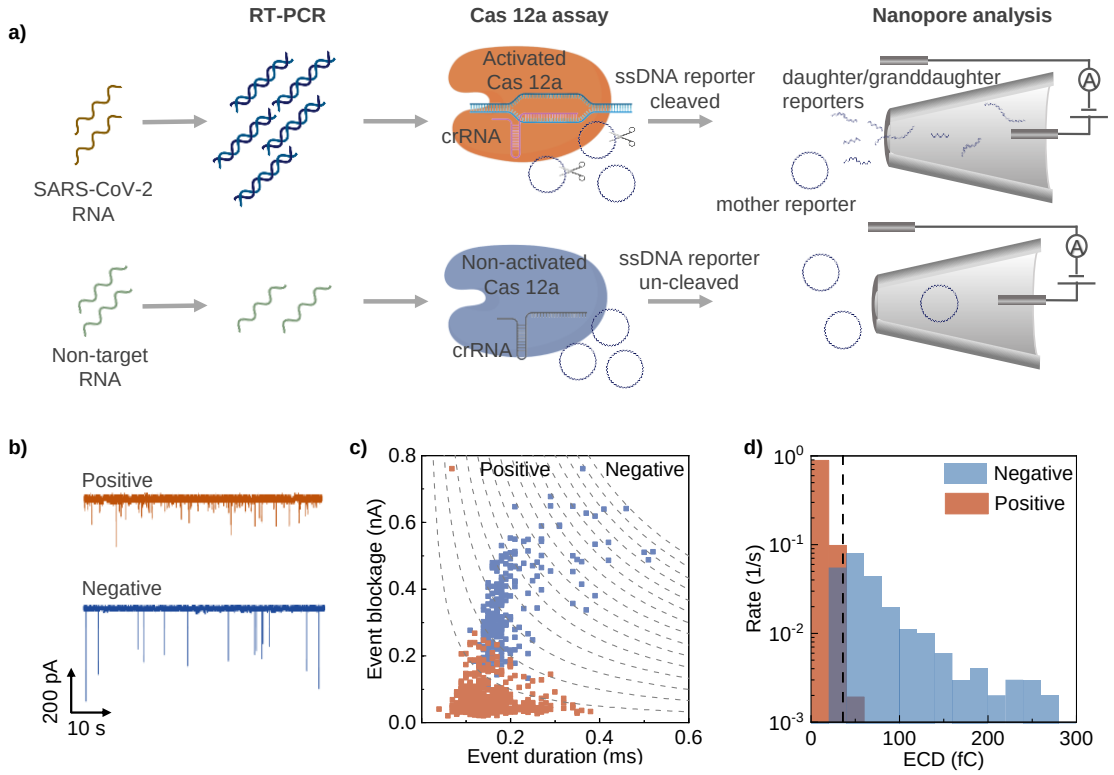

Figure 5-1. a) Schematic of Solid-State CRISPR-Cas12a-Assisted Nanopore (SCAN) sensor. The process starts with a preamplification step, followed by CRISPR assay and nanopore analysis. In a Positive case (upper side), the trans-cleavage activity of the Cas12a after activation cause degradation of the circular ssDNA reporters, resulting in reduced reporter size. In a negative case, the Cas12a is not activated in the absence of target dsDNA, and thus the ssDNA reporters are not cleaved. b) Examples of a typical ionic current trace for a positive and negative case. c) Duration and blockage of translocation events for a positive and negative case. The lines represent equivalent ECD lines from 20 to 300 fC (with a bin size of 20 fC). e) Event rate distribution at different ECD values. The right side of the dashed line represents the un-cleaved region.

These un-cleaved mother reporters and multi-generational cleaved daughter reporters were then counted and classified by a glass nanopore sensor to infer its size and concentration distribution. **Figure 5-1b** shows two representative ionic current time trace for a positive sample and a negative sample (no target control), using a glass nanopore with a diameter size less than 10 nm (**Figure 5-2a and b**). For the positive sample (presence of SARS-CoV-2 RNA), it is apparent that molecule translocation events become more frequent but have less current blockage magnitude as compared

to the negative sample. This is because the mother circular reporters were cleaved to many smaller daughter linear reporters. Our previous work analyzed the resulting reporter concentration by nanopore digital counting without taking the daughter reporter size distribution into consideration [179]. This assumption is not exactly accurate if the reaction time is short. To further analyze the daughter reporter size distribution and its relative abundance, we here adopted a nanopore sized counting method. First, the conventional event duration versus blockage was obtained from the ionic current time trace data (**Figure 5-2c**).

As shown in **Figure 5-1c**, it is evident that the event duration and blockage in a positive case are smaller than in a negative case. Second, we classified each event based on its event charge deficit (ECD), which is used as the molecule size approximation[194]. The ECD is defined as $ECD = \int_{event} \Delta I(t)dt \cong \Delta I\tau$ [195], where ΔI and τ are the duration and blockage of each event, respectively. It was previously demonstrated that ECDs of DNA translocations with the same length are identical regardless of whether the molecules are in a linear, circular relaxed, or supercoiled form [194]. An ECD bin size of 20 fC was used in this study unless otherwise stated. Third, the event rate of each ECD sub-population was obtained by normalizing sub-population event numbers by the nanopore reading time (**Figure 5-1d)**. This enables us to quantify the reporter sub-population concentration through $R_i = C_i\ \alpha N_A$, where N_A is the Avogadro constant, and α is usually referred to as the capture rate [41, 43, 94, 96].

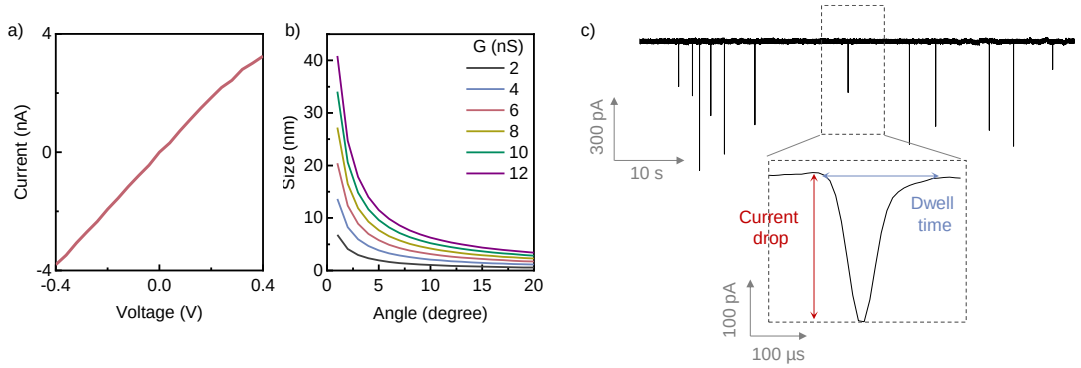

Figure 5-2. a) A typical I-V characterization of the glass nanopore. Based on the result, the average conductance of the nanopore was around 9.2 nS b) Estimation of the nanopore size based on its conductance (G) and half-cone angle (θ). While it is well known that there are variations in each fabrication due to the temperature and humidity changes, SEM and TEM characterization is needed to ensure the pore size and shape. However, since the TEM and SEM characterization of the glass nanopore is destructive in nature (high energy beams will melt the delicate structures at the tip), we often rely on the *in-situ* I-V characterization to infer the size of the nanopore. Based on the findings of Kowalczyk *et al.*[196] and Makra *et al.[197]*, the conductance of a pore has a linear relationship with the pore diameter (D_p) as: $D_p = \frac{2G}{\sigma}\frac{4+\pi\ tan\theta}{4\pi\ tan\theta}$, where σ is the conductivity of the 1 M KCL solution (10.86 S/m). Therefore, one can estimate the nanopore size based on the angle and the conductance of the pore measured by the I-V characterization. In our system, for a pore with a half-cone angle between 3 to 6 degrees, the nanopore size would be between 5 to 10 nm. b) Demonstration of the event duration and blockage measurements from a typical ionic current trace of the nanopore experiment.

The mean (μ) and standard deviation (σ) of the ECD value in the negative cases was used to establish an ECD threshold (*ECDt=μ-2σ*, dashed line in **Figure 5-1d**). An event must have an ECD larger than *ECDt* to be classified as the intact mother reporters (*i.e.*, to the right of the dashed line in **Figure 5-1d)**. To quantify the percentage of the mother reporters being cleaved into daughter reporters, we defined the cleavage ratio (*CR*) as the ratio between the cleaved mother reporter ($C_0 - C_{uncleaved}$) to the total initial mother reporter (C_0). This cleavage ratio can be experimentally obtained by evaluating the aggregated event rate as

$$CR = 1 - \sum_i R_{pi} / \sum_j R_{nj} \qquad (5.1)$$

in which the event rate summation is over all events with *ECD* larger than *ECDt* (thus representing the intact mother reporter concentration in the system), and *n* and *p* denote the negative and positive cases, respectively. The increase in the cleavage ratio of a testing sample would confirm the existence of the target viral RNA.

5.4 Results and discussion

5.4.1 SARS-CoV-2 Cas12a assay validation

Prior to the Cas12a assay, a one-step RT-PCR was performed to increase the number of molecules and boost the signal. We utilized the primers designed by the United States Centers for Disease Control and Prevention (CDC) targeting the N2 region of the SARS-CoV-2 [198]. We performed a real-time RT-PCR with 2×10^5 copies/µl of SARS-CoV-2 viral RNAs for a duration of 45 cycles. The fluorescent signal confirmed the amplification after 20 cycles (**Figure** 5-3).

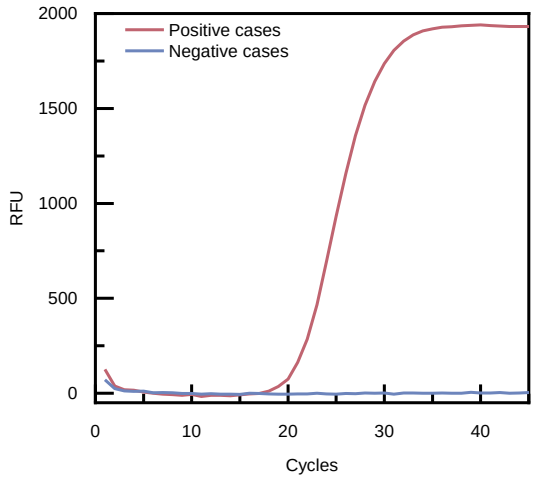

Figure 5-3. Relative fluorescence units (RFU) at different cycles of the RT-PCR. The RT-PCR was performed with an input of 2×10^5 copies/µl of SARS-CoV-2 viral RNAs for a duration of 45 cycles. The result of the fluorescent signal indicated the amplification after 20 cycles

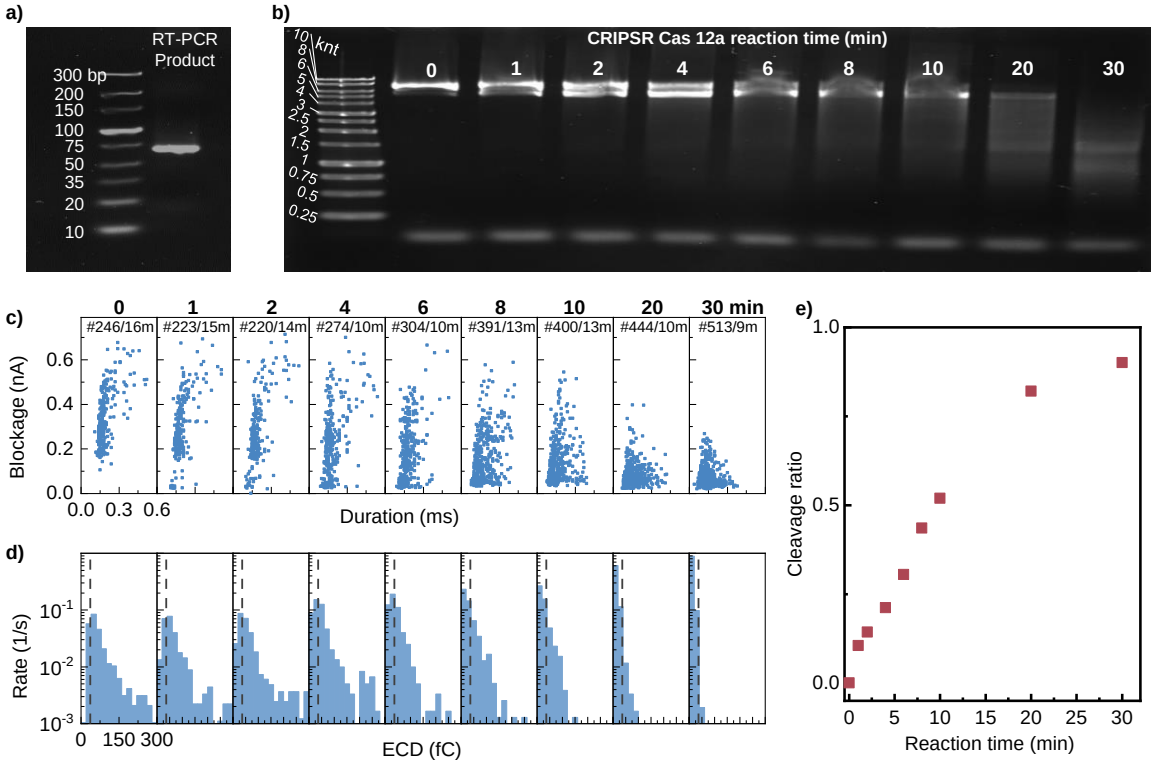

Figure 5-4. a) Gel electrophoresis results of the RT-PCR products validating the length of amplicons as 67 bp. b) Gel electrophoresis results of Cas12a assay products at different reaction times from 0 to 30 minutes. In all cases, the non-activated Cas12a and reporter concentration was fixed as 30 nM and 2.1 nM, respectively. c) Current drop and dwell times of the ssDNA reporter translocation events at different reaction times through the glass nanopore under 400 mV bias. The buffer salt concentration was fixed as 1 M. The total number of events and nanopore reading time is shown for each case d) Event rate distribution at different ECD values. The area right to the dashed line represents the un-cleaved region. e) The calculated values for reporter cleavage ratios at different reaction times.

To further confirm the amplicon product, we performed gel electrophoresis of the RT-PCR products, which showed a sharp band at 67 bp, as expected with our RT-PCT primer design (**Figure 5-4a**). Afterward, we performed the SARS-CoV-2 specific Cas12a assay with reaction time ranging from 0 to 30 mins. The reaction was stopped by adding the DNA gel loading dye (6X), which contained ethylenediaminetetraacetic acid (EDTA). **Figure 5-4b** presents the gel electrophoresis results of the Cas12a assay. We observed several important features. First, the mother reporter appeared in a double band around 7 kbp. This is due to the fact that electrophoretic mobility of

DNA in gels could also be affected by the conformation of the DNA[199]. Second, the daughter reporters become visible after 2 minutes, indicating the cleavage of mother reporters. Third, the primers were observed as a blurred short band in all cases. Fourth, as we increased the reaction time, more mother reporters were cleaved. At 30 minutes, the 7.2 kilo-nucleotides (knt) band of un-cleaved mother ssDNA become barely visible.

To examine the Cas12a cleavage kinetics at a much longer time scale, we performed another test by intentionally extending the Cas12a reaction time up to 24 hours. We found that all mother and prior generation daughter reporters were completely cleaved to be less than 250 nt after 24 hours (**Figure 5-5**). This suggests the trans-cleavage activities indiscriminately and continuously affect both the mother reporters and the partially cleaved daughter reporters.

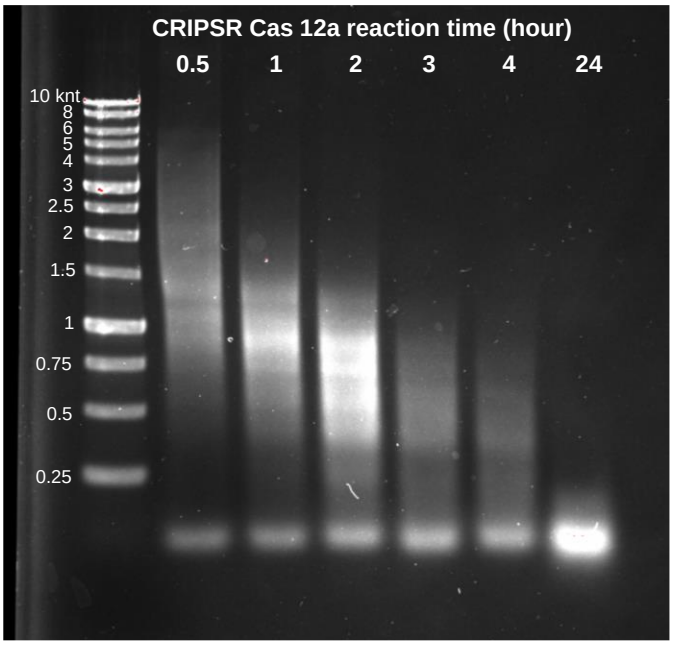

Figure 5-5. Gel electrophoresis results of the Cas12a assay products at five reaction times from 0.5 to 24 hours. All mother reporters were completely cleaved to be less than 250 nt after 24 hours. This suggests the trans-cleavage activities indiscriminately and continuously affect both the mother reporters and the partially cleaved daughter reporters.

As a control, we also performed the Cas12a assay for no target samples to confirm that no degradation of the mother reporters would occur in the absence of SARS-CoV-2 amplicons (**Figure 5-6**).

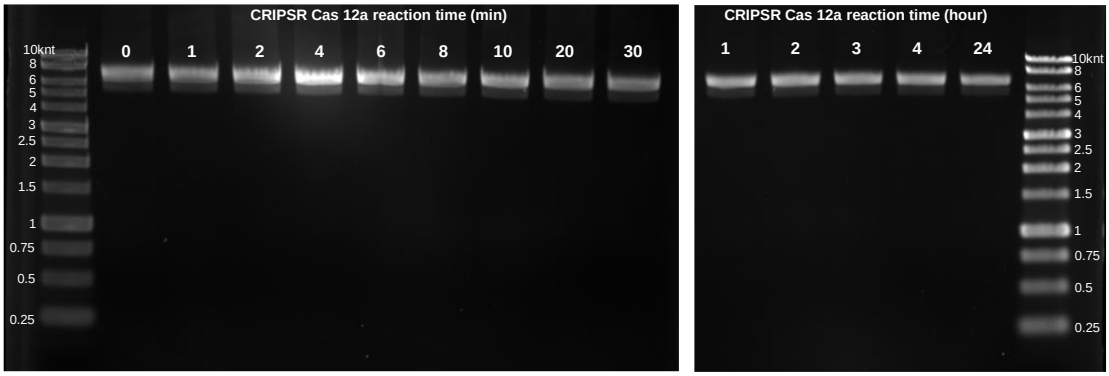

Figure 5-6. Gel electrophoresis results of the no target negative control samples at different Cas12a reaction times from 0 min to 24 hours. No Cleavage was observed in all reaction times, which confirms that daughter and granddaughter reporters would not be generated in no target negative control samples.

5.4.2 Highly sensitive nanopore measurement of the cleavage ratio

After validating the Cas12a assay with gel electrophoresis, we set out to perform the SARS-CoV-2 detection with the glass nanopore. We performed the Cas12a assay with different reaction times from 0 to 30 minutes and recorded the reporter translocations through the nanopore under 400 mV bias (**Figure 5-7)**. Note that in our glass nanopore measurement, DNAs with sizes less than 100 bp are often too small to be detected. Those significantly cleaved reporters with lengths less than 100 bp and RT-PCR amplicons (67 bp) could not contribute to the detected signals. In addition, in our previous study [193], we showed that the other components in the assay, such as Cas12a proteins, do not create signals in the nanopore experiment. Therefore, all the signals in the nanopore measurements are caused by the reporters with a length above the detectable threshold (a few hundred nucleotides).

Figure 5-4c shows the extracted translocation dwell time versus ionic current blockage at each reaction time**.** A clear shift of the blockage-duration distribution was observed when increasing the reaction time, indicating the changing populations of differently sized reporters. To quantify the abundance of differently sized reporters, we used an ECD bin size of 20 fC to classify the events into different sub-populations and calculated its corresponding event rate. **Figure 5-4d** shows the event rate distribution for all sub-populations. As shown, the event rate of larger ECDs (longer reporters) is reducing as the cleavage reaction goes, whereas the event rate of smaller ECDs (shorter reporters) is increasing. Since the concentration of the analyte could be quantified by the event rate in the nanopore experiment, these measurements give us the capability to quantify the relative abundance of differently sized reporters.

To quantify the cleavage ratio at different reaction times, we utilized the nanopore-sized counting method. The case at 0 min of reaction was considered as the negative case to establish the ECD_t. The cleavage ratio (*CR*) at each reaction time was then obtained by using Eq. 5.1. As shown in **Figure 5-4e**, the *CR* was at 0.12 after 1 minute of reaction and increased as increasing the reaction time.

For instance, *CR* was measured as 0.92 at 30 minutes of reaction. As the reaction times increase, more daughter and granddaughter reporters would be created, which increases the possibility of multi-turn cleavage. Therefore, the cleavage ratio increases at a lower rate as we increase the reaction time. It is noteworthy that we were able to detect the cleavage activity after 1 minute in nanopore reading, whereas no cleavage was barely visible in the gel after 1 minute of reaction (**Figure 5-4b)**. This indicates that the nanopore is a much more sensitive readout system for *CR* measurement.

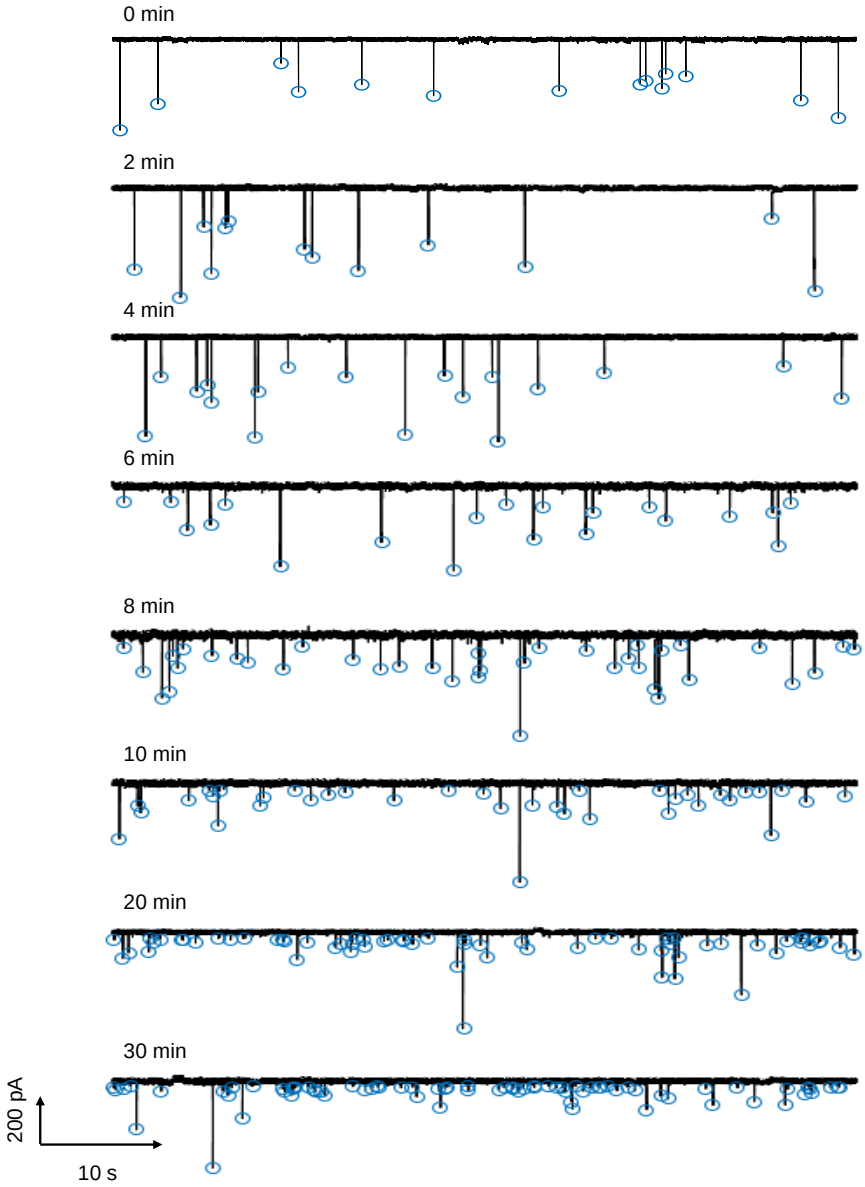

Figure 5-7. Translocation recording of ssDNA reporters at different reaction times from 0 to 30 minutes through the glass nanopore under 400 mV bias. The Cas12a and buffer salt concentrations were fixed as 30 nM and 1 M, respectively. As we increased the reaction time, more events were observed; however, the magnitude of the current drop of events become smaller.

5.4.3 Cleavage numerical modeling and validation

In order to guide our experiments for rapid and sensitive detection of the cleavage ratio using nanopore experiment, we sought to develop a model to estimate the distribution of reporter length over the trans-cleavage process. At the start of the reaction, we assumed that each mother reporter has an identical length of L_m. As the reaction starts, the reporters (including mother and daughter reporters) were randomly picked by the activated Cas12a. The probability that a reporter was picked and cleaved by the Cas12a was proportional to its cross-sectional area R_g^2, where R_g is the gyration radius of the DNA coil. It has been shown that the gyration radius of DNA is proportional to the square root of its length ($L^{1/2}$) [94]. Therefore, the longer the reporter was, the more chance that it was bounded to and cleaved by the Cas12a. The reporter was cut into two parts randomly. We assumed a normal distribution to model the cleavage position in a report. The velocity of the cleavage was modeled by $v(t) = k_{cat}\frac{[E_0][S(t)]}{K_M+[S(t)]}$, in which $[E_0]$ is the initial enzyme (activated Cas12a) concentration, $[S(t)]$ is the substrate concentration (mother and daughter reporters), k_{cat} and K_M are the catalytic rate and the Michaelis constant, respectively. We used previous reported k_{cat} and K_M value of 0.6 (1/s), and 2.7×10^{-6}, respectively [200]. This model was numerically implemented in a customized MATLAB code (see **Figure 5-8** for model flowchart and results).

In order to validate this numerical model for predicting the reporter size distribution after reaction, we performed the Cas12a assay at three enzyme concentrations (7.5, 15, and 30 nM) with reaction times ranging from 0 mins to 24 hours. **Figure 5-9a** presents the gel electrophoresis results. As expected, higher enzyme concentration indeed results in faster cleavage activity since the cleavage velocity is proportional to the enzyme concentration. We extracted the length distribution of the reporter from the gel images by measuring the normalized grayscale values using ImageJ software [201, 202]. The normalized reporter length distributions were then overlaid with the results

produced by our model. As shown in **Figure 5-9b**, shorter daughter reporters were produced at a fixed reaction time as enzyme concentration was increased. Also, both model and gel results showed that the mother reporters were cleaved entirely after 24 hours. The distribution of reporter length captured by our model is consistent with the gel electrophoresis results, which validates our model.

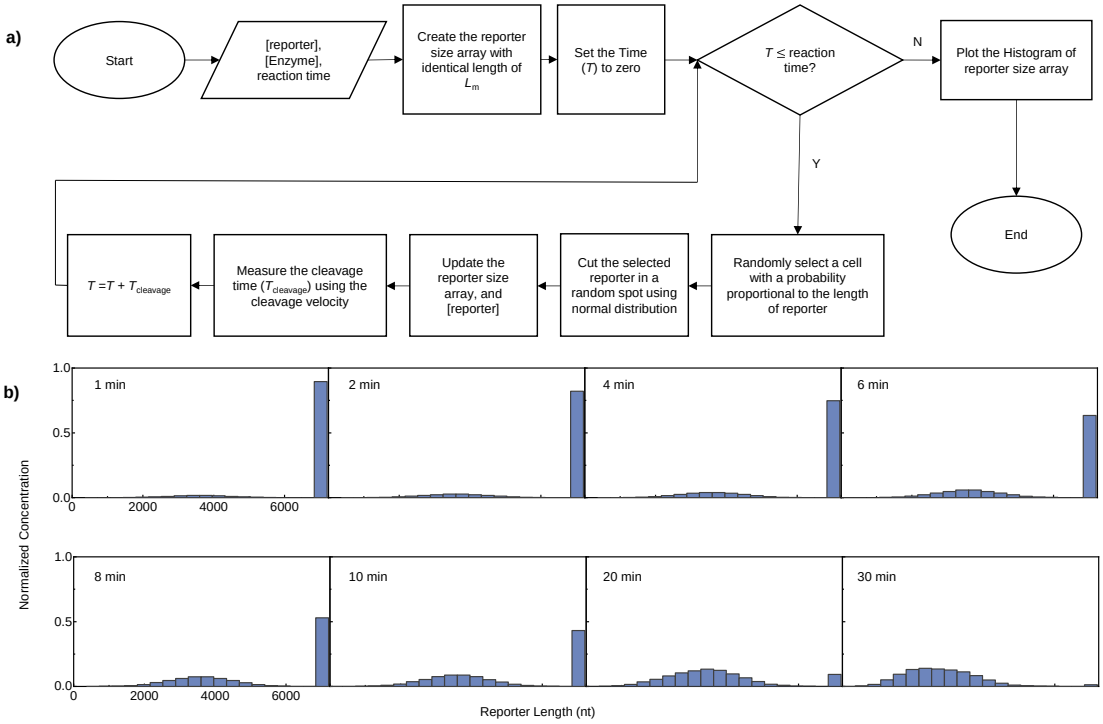

Figure 5-8. a) Algorithm and the model details for estimating the reporter length distribution over the trans-cleavage process. Initially, the reaction time, reporter, and enzyme concentration were specified. An array with an identical length of L_m (in this study L_m=7200) was created to present the mother reporter size. Time was set as zero, and the cleavage loops were started. In each loop, one cell of the reporter size array was randomly selected proportional to the length of the reporters. Afterward, the reporter in the selected cell was cleaved in a random spot using a normal distribution. After the cleavage, the reporter size array and reporter concentration was updated. The cleavage time was calculated by the cleavage velocity, and the total time was updated. The looped continued while the total time was less than the specified reaction time. Finally, after the cleavage process, the histogram of reporter size was plotted. b) The distribution of reporter length with an initial enzyme concentration of 30 nM over different reaction times from 1 to 30 minutes.

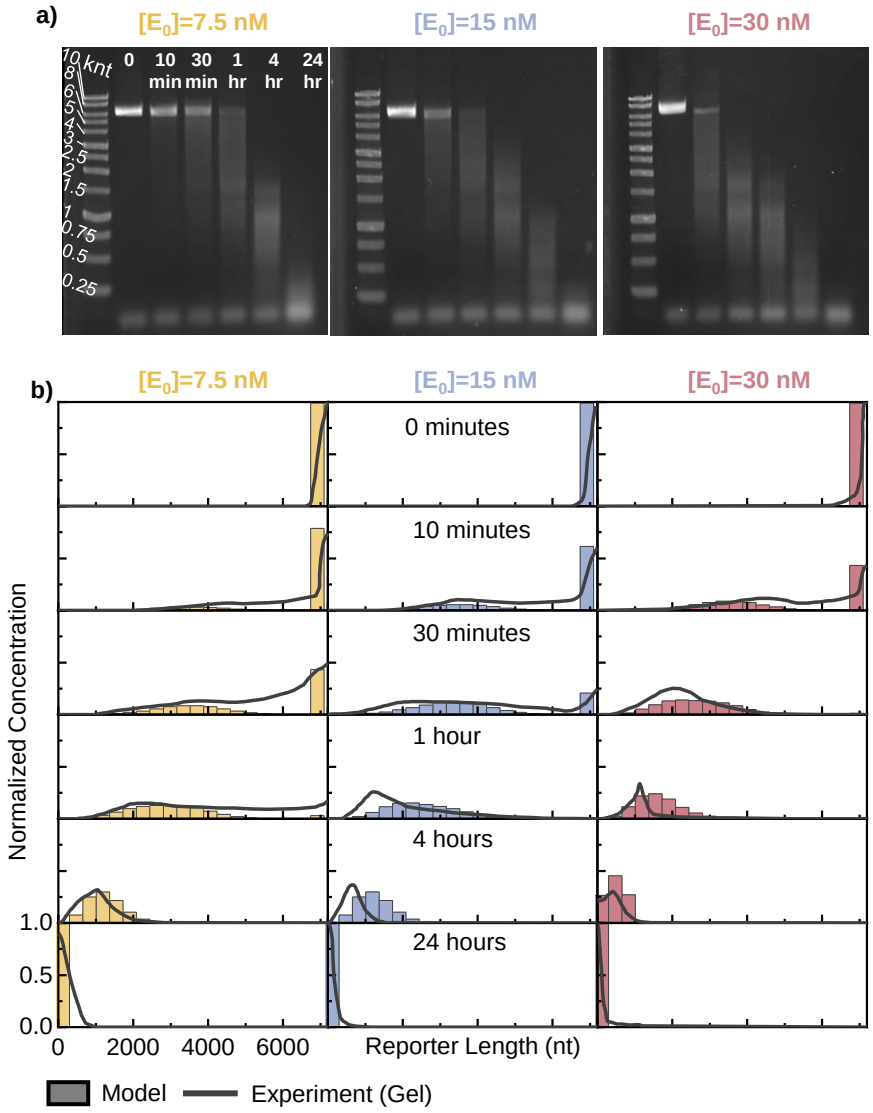

Figure 5-9. a) Gel electrophoresis results of the Cas12a assay at three different initial enzyme concentrations (7.5, 15, and 30 nM) and different reaction times (from 0 minutes to 24 hours). b) Comparison between the reporter length distribution captured by the model and Gel electrophoresis. The normalized grayscale value of the gel results was measured by ImageJ software for the estimation of the reporter concentration.

5.4.4 The tradeoff between sensitivity, reaction time, and false-positive rate

Since the cleavage ratio (*CR*) was used to distinguish a positive and a negative sample, we calculated the *CR* with the model-produced length distributions. The model-derived *CR* values were

then compared with the nanopore-measured *CR* values using the sized counting method (Eq. 1.1). We measured the *CR* at different enzyme concentrations (7.5, 15, and 30 nM) with ranging reaction times from 0 to 30 mins. As shown in **Figure 5-10a**, the model predicted *CR* values agree excellently with that measured by the nanopore.

With the capability to calculate the *CR* at varying activated Cas 12a and reaction time, we were able to estimate the sensitivity and turnaround time of the SCAN system at any given *CR* threshold (CR_t) for a positive call. **Figure 5-10b** presents the minimal required reaction time versus the activated Cas12a enzyme concentration. Note that the activated Cas12a enzyme concentration is equal to the smaller values between SARS-Cov-2 amplicons and non-activated Cas12a concentration in the system.

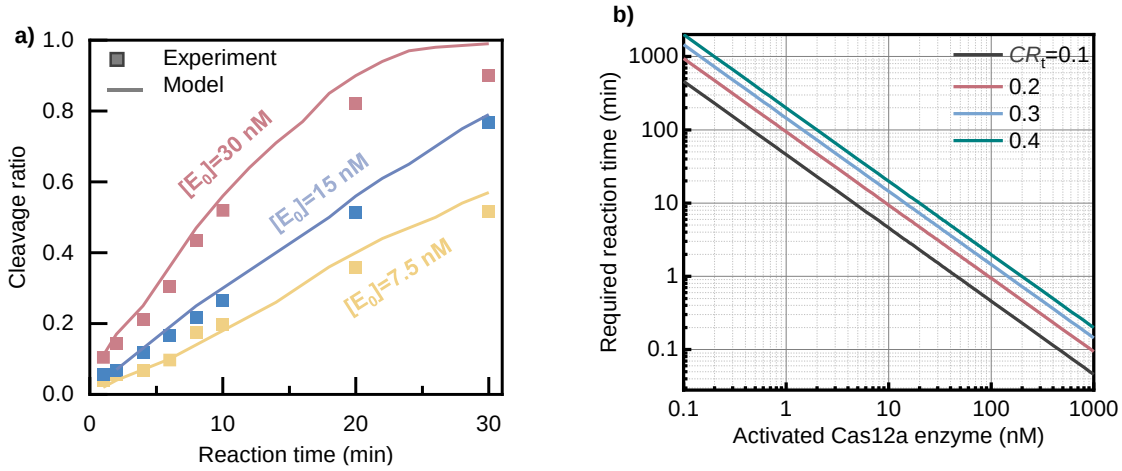

Figure 5-10. a) The measured cleavage ratio of the ssDNA reporter by the sized counting method (experiment) and the numerical model at different reaction times. The outcome of the model and nanopore experiment is in good agreement at three different enzyme concentrations (7.5, 15, and 30 nM). b) Required reaction time versus the activated Cas12a enzyme concentration (from 0.1 to 1000 nM) at four different *CR* thresholds values.

As shown in **Figure 5-10b,** at any given CR_t for a positive call, there is a tradeoff between turnaround time and sensitivity. More reaction time was required when decreasing the activated

Cas12a enzyme concentration. For instance, at CR_t =0.1, more than 45 mins will be required to detect 1 nM of amplicons, whereas 0.45 min is sufficient with 100 nM amplicons. On the other hand, while increasing the CR_t could help to reduce the false-positive rate, it would increase the required minimal reaction time at any given amplicon concentrations. In fact, the *CR* is proportional to the product of cleavage velocity and reaction time (T_r), $CR = v\,T_r$. The cleavage velocity v is proportional to the activated Cas12a concentration C_{enzyme} as $v = \beta C_{enzyme}$. Therefore, one can see that $C_{enzyme}\,T_r/CR$ should equal to the constant coefficient β. This relationship suggests there is a tradeoff between sensitivity (C_{enzyme}), reaction time (T_r), and false-positive rate (CR). With a fixed C_{enzyme} , a higher CR (less false-positive) calls for a longer reaction time T_r. With a fixed CR , reducing the C_{enzyme} (better sensitivity) also requires a longer reaction time T_r (longer turnaround). By coupling with a pre-amplification step, the C_{enzyme} can be effectively enhanced and thus significantly reduce the required T_r (turnaround time).

5.4.5 Analytical specificity and sensitivity of SARS-CoV-2 SCAN

We then went to evaluate the analytical sensitivity and specificity of SARS-CoV-2 SCAN. We used heat-inactivated SARS-CoV-2 RNA samples at different concentrations ranging from 2 to 200 copies/µl. In addition, three other human coronaviruses (229E, NL63, and OC43) with a concentration of 5×10^5 copies/µl were used as the non-target negative controls to evaluate the specificity. 5 µl of each sample was firstly amplified by RT-PCR for 45 cycles (**Figure 5-11**). The product of the RT-PCR was added to 30 nM of non-activated Cas12a. The Cas12a cleavage assay was performed at 37ºC for 30 min. Afterward, the nanopore sized counting was performed to determine the cleavage ratio. A positive/negative call was subsequently derived by comparing the obtained cleavage ratio with CR_t (dashed line in **Figure 5-12a**). The CR_t was defined in our

experiment as $\mu_0+2\sigma_0$ (0.089), where μ_0 (0.054) and σ_0 (0.017) are the mean and standard deviation of the cleavage ratio obtained from no target controls (*i.e.*, SARS-CoV-2 sample at zero concentrations). **Figure 5-12a** presents the cleavage ratios of all SARS-CoV-2 and non-target human coronaviruses samples. As shown, the cleavage ratios for all non-target human coronavirus samples (circle, diamond, and star symbols in **Figure 5-12a**) are less than CR_t and were correctly classified as negatives. This confirmed that the SCAN sensor has an excellent specificity against SARS-CoV-2.

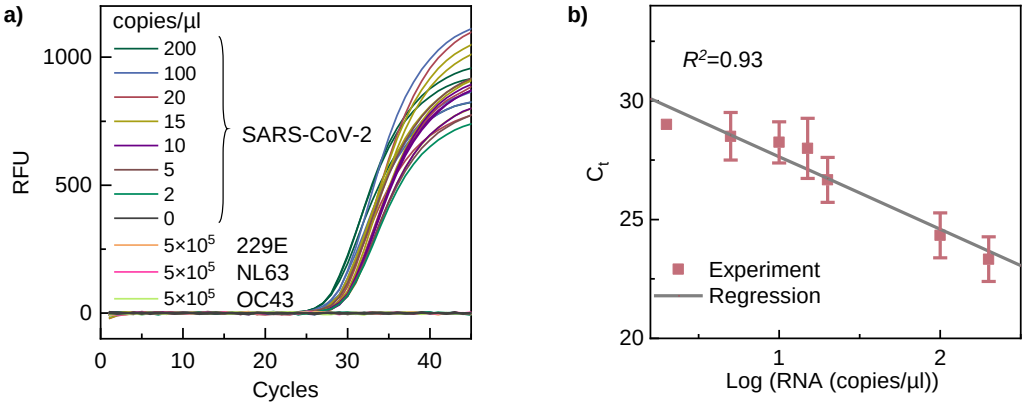

c)

	SARS COV-2								Human Coronavirus		
									229E	NL63	OC43
RNA (copies/µl)	200	100	20	15	10	5	2	0	5×10^5	5×10^5	5×10^5
Amplified Cases	3/3	3/3	3/3	5/5	4/5	2/5	1/5	0/5	0/3	0/3	0/3

Figure 5-11. a) The relative fluorescence unit (RFU) over different cycles of the RT-PCR process. The fluorescence results indicated that the limit of detection of RT-PCR assay was around 10 copies/µl, where 4 out of 5 cases were amplified. b) The threshold cycle (C_t) measurement at different starting RNA copies revealed that the SARS-CoV-2 could be quantitatively estimated by the real-time RT-PCR. The logarithmic regression for the C_t values over different input copies showed that the SARS-CoV-2 RNA in a sample could be estimated by C_t=*-3.052×log (copies)+32.829*. c) Summary of the amplification process for all the samples to evaluate the analytical sensitivity and specificity of SARS-CoV-2 SCAN.

For the serially diluted SARS-CoV-2 samples (square symbols in **Figure 5-12a**), we found that concentrations higher than 15 copies/µl were classified correctly as positives since their cleavage ratios are much larger than CR_t. The high cleavage ratio in these samples indicates the majority of the mother reporters were cleaved after 30 min of reaction.

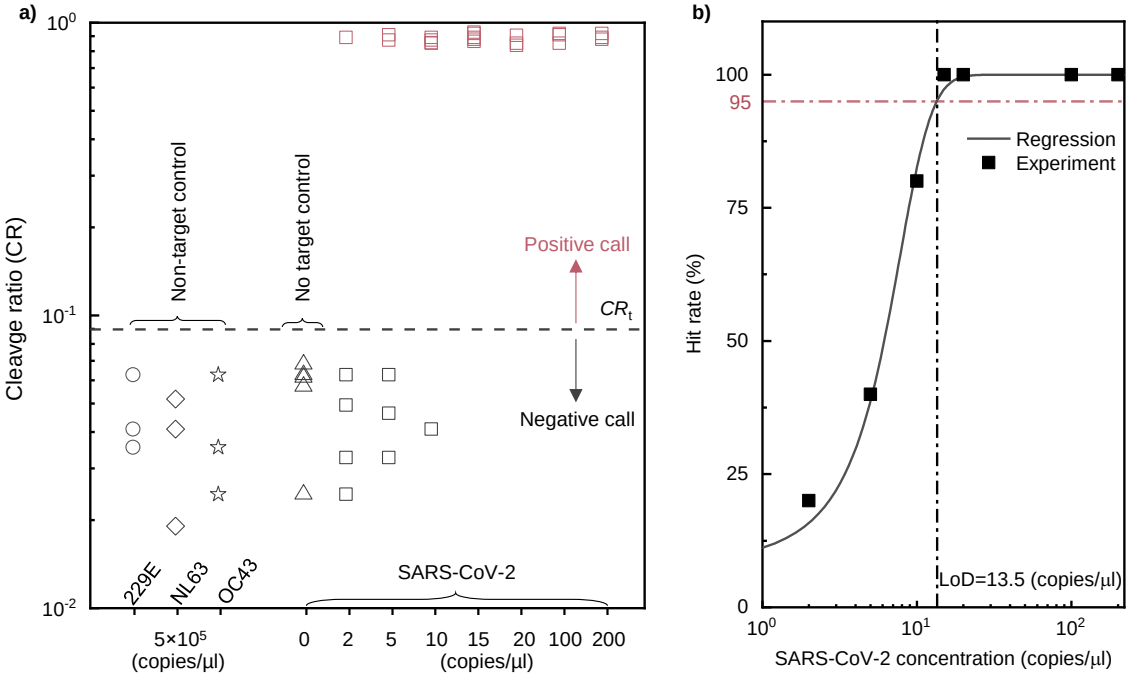

Figure 5-12. a) Cleavage ratio of three different human coronaviruses samples (for specificity test) and SARS-CoV-2 (for sensitivity test) with different input RNA concentrations. Five repeats were performed for lower concentrations (less than 20 copies/µl), and three were tested for higher concentrations (more than 20 copies/µl) and non-target control samples. The cleavage ratios were measured using the nanopore sized counting experiment. The average and standard deviation of the *CR* values of 5 negative target controls were measured to identify the threshold for separating positive from negative calls. Any cases with a *CR* below $CR_t = \mu+2\sigma$ (0.089) were classified as negatives. b) The hit rate percentage at different concentrations of SARS-CoV-2 RNA. The LoD was estimated as 13.5 copies/µl at a 95% confidence level.

On the other hand, we started to observe false negatives results in samples with concentrations lower than 15 copies/µl. For instance, 1 out of 5 samples at a concentration of 10 copies/µl and 4 out of 5 samples at 2 copies/µl were misclassified as negatives. To estimate the LoD of SARS-

CoV-2 SCAN, we examined the hit rate at each different SARS-CoV-2 concentration. The hit rate is defined as the number of replicates with a detected outcome per the total number of replicates tested [203]. As shown in **Figure 5-12b**, the hit rate started to roll off from 1 to 0.8 when the concentration decreased from 15 copies/µl to 10 copies/µl. We fitted the experimental hit rate data with a logistic curve (**Figure 5-12b**) [204, 205]. Based on the fitting curve, we estimated the LoD of SARS-CoV-2 SCAN as 13.5 copies/µl (22.5 aM) at the 95% confidence level.

5.5 Summary

In summary, we introduced and evaluated a sized counting method for nanopores-assisted CRISPR-Cas12a-based detection of SARS-CoV-2. A sized counting scheme for cleavage quantification of the reporters in the Cas12a assay was introduced by utilizing ECD values from the nanopore experiment. We found that the nanopore is a sensitive readout system to measure the cleavage ratios, a criterion used for positive or negative classification. A kinetic cleavage model was developed and experimentally validated to predict the reporter length distribution. This model revealed the tradeoffs between sensitivity, reaction time, and false-positive rate in the SARS-CoV-2 SCAN. These tradeoffs could be relaxed by coupling with pre-amplification steps. With a 25 min RT-PCR step, 30 min of CRISPR Cas12a assay, and 10 min of nanopore reading (65 min of assay-to-result time), we achieved a limit of detection of 13.5 copies/µl (22.5 aM) of viral RNA. The SARS-CoV-2 SCAN showed an excellent specificity with no cross-reactivity to other human coronaviruses. These results suggested that the solid-state CRISPR -Cas12a-assisted nanopores could provide a rapid, sensitive, and specific analysis of SARS-CoV-2.

CHAPTER 6 THE FIGURE OF MERIT FOR CRISPR-BASED NUCLEIC ACID-SENSING SYSTEM: IMPROVEMENT STRATEGIES AND PERFORMANCE COMPARISON

In this chapter, we developed a quantitative CRISPR sensing figure of merit (FOM) to compare different CRISPR methods and explore performance improvement strategies. The CRISPR sensing FOM is defined as the product of the limit of detection (LOD) and the associated CRISPR reaction time (T). A smaller FOM means the method can detect smaller target quantities faster. We found that there is a tradeoff between the LOD of the assay and the required reaction time. With the proposed CRISPR sensing FOM, we evaluated five strategies to improve the CRISPR-based sensing: preamplification, enzymes of higher catalytic efficiency, multiple crRNAs, digitalization, and sensitive readout systems. We benchmarked the FOM performances of 55 existing studies and found that the effectiveness of these strategies on improving the FOM is consistent with the model prediction. In particular, we found that digitalization is the most promising amplification-free method for achieving comparable FOM performances (~ 1 fM·min) as those using preamplification. The findings here would have broad implications for further optimization of the CRISPR-based sensing.

6.1 Introduction

Sensitive, accurate, and fast diagnostics of infectious diseases is crucial to optimize clinical care and guide infection control and public health interventions to limit disease spread. The development of the clustered regularly interspaced short palindromic repeats (CRISPR)-based methods have taken center stage in biotechnology since the modified CRISPR/Cas9 system was applied for gene editing in mammalian genomes [206]. Additionally, the CRISPR-Cas9 system has shown

outstanding competence in nucleic acid-sensing with high specificity [147, 192, 207-210]. Recently, the discovery of the collateral cleavage in other Cas proteins like Cas12 [142], Cas13 [137], and Cas14 [178] made it possible to translate the sequence-specific targeting to other detectable signals, which has led to the increasing emergence of CRISPR-mediated biosensors [130, 136-138, 166-170, 189, 211, 212]. In 2017, Gootenberg *et al.* introduced the specific high sensitivity enzymatic reporter unlocking (SHERLOCK), which exploits Cas13a for viral RNA detection [137]. Simultaneously a Cas-12a-based nucleic acid-sensing tool called a one-hour low-cost multipurpose highly efficient system (HOLMES) was introduced in 2018 [142]. The potential of CRISPR-based diagnostic systems was established in the recent global pandemic where numerous CRISPR-based tests were developed for SARS-CoV-2 (emerging virus responsible for COVID-19 pneumonia) detection [163, 172, 180-187].

While CRISPR-based nucleic acid-sensing systems are growing rapidly, an objective approach to benchmark and compare the performances of different systems remains challenging. Several previous studies have reviewed the performances of various CRISPR-based methods [179, 188, 213-215]. As a potential diagnostic tool, two of the most important performance metrics in CRISPR-based methods are the achievable limits of detections (LODs) and the required reaction times [213, 214]. It is generally favorable to obtain lower LODs in shorter reaction times. Ramachandran *et al.* recently presented an analytical model based on Michaelis-Menten enzyme kinetics to address the question of what are the achievable limits of detection and associated CRISPR reaction times [216]. This study demonstrated that the reaction time is inversely proportional to the target abundance and the Cas enzyme catalytic efficiency. Nevertheless, from the whole system perspective, the achievable LOD and the associated reaction time depend not only on the Cas protein catalytic efficiency but also on other conditions such as preamplification [137, 142], reaction volumes [217, 218], target activator [142, 216], and readout systems [188,

219]. Due to these variations, there were almost no identical setups among different reported CRISPR-based methods.

In this work, we proposed and developed a figure of merit (FOM) for CRISPR-based nucleic acid-sensing systems with the goal to quantitatively benchmark different methods and explore the performance improvement strategies. We developed a kinetic model utilizing a single-enzyme framework and then extended it to bulk (multi-enzyme) systems. The CRISPR-based nucleic acid-sensing FOM, defined as the product of the LOD and CRISPR reaction time, is analytically established by connecting the LOD and reaction time to various reaction setup properties. Using the developed FOM model, we evaluated five strategies to achieve lower LODs with shorter reaction times (*i.e.*, lowering the FOM value). We also compared the improved efficiency of these five strategies. Finally, we benchmarked a total of 55 published works related to CRISPR-based nucleic acid-sensing with reaction and performance parameters available. We found that digital CRISPR offers the best (lowest) FOM among various strategies and represents the most promising route towards amplification-free CRISPR-detection methods.

6.2 Establishment of the CRISPR Sensing FOM

Figure 6-1 presents the common steps for a CRISPR-based nucleic acid-sensing system. We assume the CRISPR nucleic acid-sensing starts with N_0 copies of the targets (DNA or RNA). Normally, a preamplification step could be performed to increase the copy numbers of the targets. For RNA targets, a reverse transcription (RT) step should be performed before or simultaneously with the amplification. Afterward, the cDNA product could be directly utilized in the Cas12 assay [138, 220] and should be transcribed back to RNA targets in the Cas13 assay [137, 176]. While

each different amplification method has its unique kinetics, the number of the amplified targets (N_1) can be related to the initial target quantity N_0 as, $N_1 = A\,N_0$, where A is the amplification ratio.

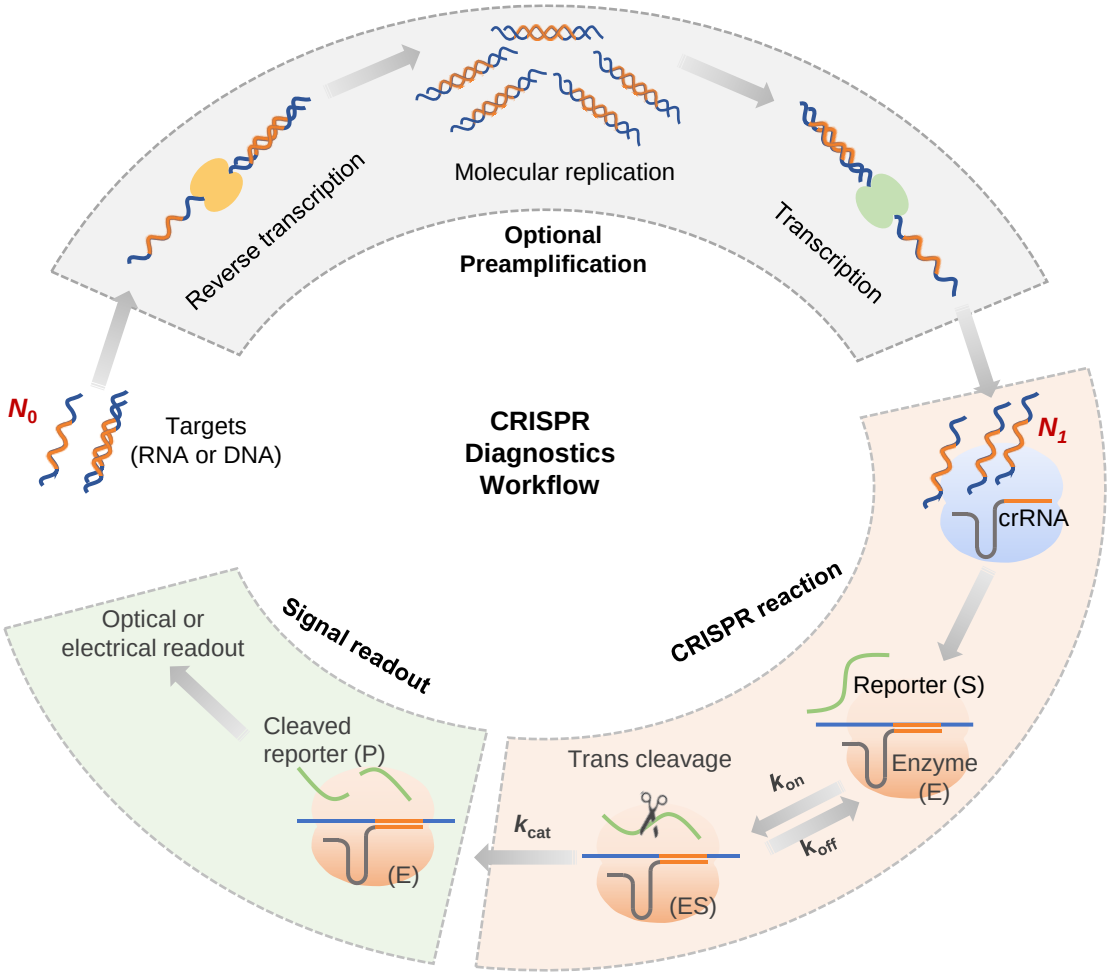

Figure 6-1. Typical steps in CRISPR-based nucleic acid-sensing system. As an optional step, the DNA or RNA targets could be pre-amplified before the Cas reaction to increase the target quantity. Reverse transcription or transcription will be needed depending on the Cas protein property and targets (note that the illustration shows a Cas13 assay as an example). In the CRISPR reaction, the target molecules are specifically recognized and bounded to the Cas proteins and their associated crRNA (*i.e.*, Cas proteins activation). The trans-cleavage of the reporters could be described as an enzymatic reaction where activated Cas proteins and reporters act as enzymes and substrates, respectively. The cleaved reporter results in signal development in various forms (optical or electrical), which is detected by a readout system.

After this optional amplification step, the specific binding of the nucleic acids to the non-activated Cas proteins (Cas/crRNA binary complex) would activate the Cas proteins (Cas/crRNA/target ternary complex). Upon activation, Cas12 and Cas13 indiscriminately trans-cleavage ssDNA and ssRNA reporters, respectively [221]. Since the trans-cleavage activity is an enzymatic reaction, the CRISPR assay can be modeled as [216],

$$E + S \underset{k_{\text{off}}}{\overset{k_{\text{on}}}{\rightleftharpoons}} ES \overset{k_{cat}}{\rightarrow} P + E \quad (6.1)$$

where k_{on}, k_{off}, and k_{cat} are the forward, reverse, and catalytic rates, respectively. *E* represents the enzyme (activated Cas protein), *S* is the substrate (intact reporters), *ES* is the reaction intermediate (enzyme-substrate reporter complex), and *P* signifies the product (*i.e.*, cleaved reporters).

To capture the speed of product formation, we started from the reaction speed of each individual *activated* enzyme. Studies have shown that the single enzyme reaction is a stochastic process [222], and the reaction speed (s^{-1}) is the reciprocal of the mean waiting time $\langle\tau\rangle$ and can be estimated as: $1/\langle\tau\rangle = k_{cat}[S]/(K_M + [S])$, where $[S]$ is substrate concentration and K_{M} is Michaelis constant and defined as $(k_{off} + k_{\text{cat}})/k_{\text{on}}$. Assuming the total *activated* enzymes is limited by the number of targets N_1 (*i.e.*, the input Cas/crRNA binary complex is more than the nucleic acid targets, with or without amplification), we can obtain the reaction speed (s^{-1}) for the CRISPR reaction as:

$$v = N_1 k_{cat} \frac{[S]}{K_M + [S]} \quad (6.2)$$

With a CRISPR incubation reaction time of *T* and reaction volume of V_r, the *concentration* of the cleaved product would be vT/V_r. In order to effectively detect the cleaved products, the product

concentration must be larger than the readout system's limit of detection C_{min} ($vT/V_r > C_{min}$). As a result, we can obtain a critical equation for the CRISPR based nucleic acid-sensing,

$$N_0 \geq \frac{V_r C_{min}}{A T k_{cat} \frac{[S]}{K_M + [S]}} \quad (6.3)$$

This equation means that the lowest quantity of a target concentration (*i.e.*, LOD) that can be detected in a specific CRISPR assay is given by,

$$LOD = \frac{\min(N_0)}{V_0} = \frac{V_r C_{min}}{V_0 A T k_{cat} \frac{[S]}{K_M + [S]}} \quad (6.4)$$

where V_0 is the target sample volume in the Cas reaction. In theory, increasing the V_0 would decrease the LOD of the system. However, V_0 between 1 to 5 µL has been used in most reported Cas reactions [136, 137, 170]. This is because increasing the V_0 could affect the assay buffer [170]. From Eq. 6.4, we can observe a clear tradeoff between the LOD and CRISPR reaction time (T). To benchmark different CRISPR assays, we defined a figure of merit (FOM) for CRISPR-based nucleic acid-sensing as the product of the LOD and reaction time,

$$FOM = LOD \times T = \frac{V_r C_{min}}{V_0 A k_{cat} \frac{[S]}{K_M + [S]}} \quad (6.5)$$

This CRISPR-based sensing FOM could be utilized to benchmark the performance of different assays as it is related to experimental conditions such as preamplification (A), the reaction volume (V_r), readout system (C_{min}), and enzymatic efficiency (k_{cat}, K_M). A smaller FOM value means that lower quantities of the target could be detected faster. As a result, minimizing the FOM should be the goal for CRISPR-based assay optimization.

6.3 FOM Improvement Strategies

6.3.1 Use of preamplification

Based on Eq. 6.5, the FOM has a reverse relation with the amplification ratio (A). This implies that utilizing amplification with higher A would decrease the FOM and improve the overall sensing performances. In fact, various preamplification methods such as polymerase chain reaction (PCR) [142, 172, 223], loop-mediated isothermal amplification (LAMP) [169, 180, 209], and recombinase polymerase amplification (RPA) [137, 211, 224] and their reverse transcriptase (RT) version [188] were adopted in the CRISPR assays. For example, in the Cas13-based SHERLOCK system, RPA was used to improve the LOD of the system up to 6 orders of magnitude [137]. In the Cas12-based HOLMES system, the LOD was improved by 7 orders of magnitude by introducing a 45 min PCR amplification to the assay [142]. However, it is noteworthy that while preamplification could improve the FOM of the CRISPR system significantly, utilizing this additional step complicates the assay design and could increase the cost and assay time.

Figure 6-2a shows a radar chart comparing the six performance metrics of three common preamplification strategies used in CRISPR assays. **(1)** ***One-pot reaction***. While the preamplification could be performed separately before the CRISPR assay in a two-step reaction, it is preferable to combine the preamplification and the CRISPR assay in a one-pot reaction to simplify the assay setup, decrease the assay time and reduce the risk of contaminations [179].

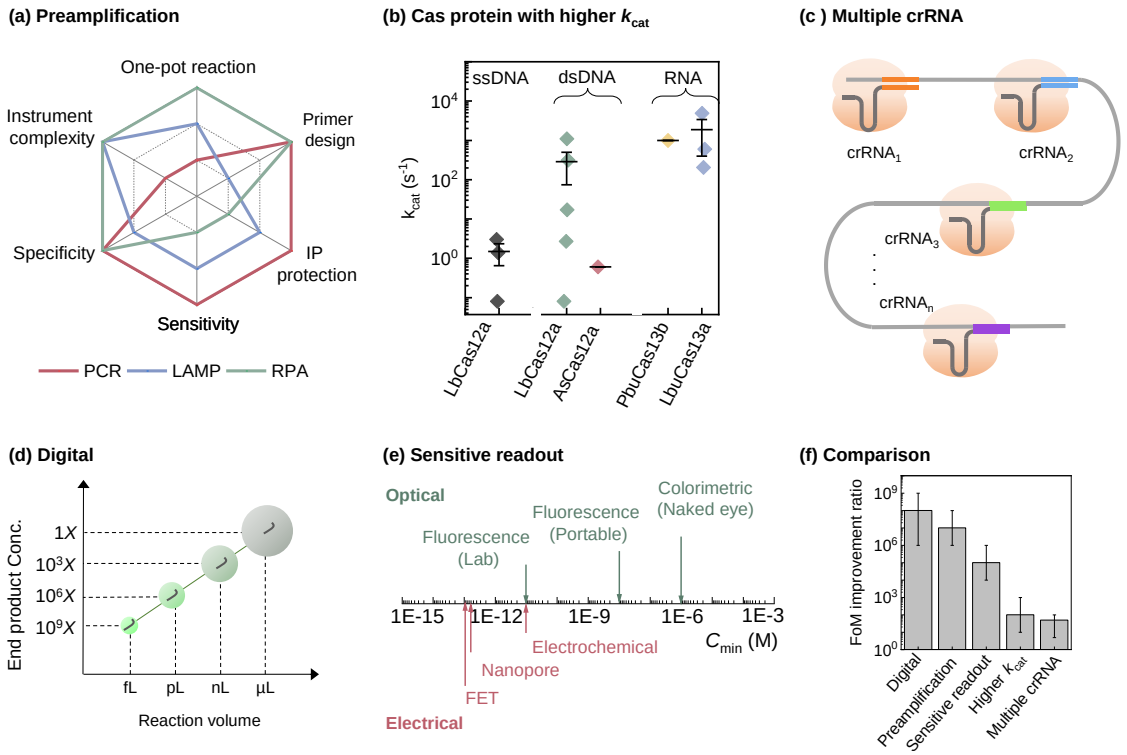

Figure 6-2. Different strategies to reduce the FOM and improve the CRISPR nucleic acid-sensing performance. (a) Qualitative comparison of three common preamplification methods. (b) The reported catalytic rate constant (k_{cat}) of CRISPR effectors activated by different activators (double- and single-stranded DNAs or RNAs). (c) Schematic of using multiple crRNAs in the CRISPR assay. Introducing *n* different crRNAs in the assay results in *n* times more activated Cas in the system and thus increasing the cleavage activity. (d) Effect of digitalization on the product (cleaved reporter) concentration. Reducing the reaction volume effectively increases the signal concentration for a fixed CRISPR reaction time. (e) Comparison of the typical detection limit of various readout methods (C_{min}). (f) Back-of-the-envelope calculation of FOM improvement ratio using different strategies.

To this end, the reaction temperature between the preamplification and the CRISPR assay should be compatible. In this regard, RPA is the most suitable preamplification method to couple with CRISPR assays since the reaction temperature is similar (~37 ºC) [188] and PCR is incompatible with CRISPR due to its required thermal cycling. LAMP is somewhere in between due to its isothermal nature and had been used in one-pot CRISPR reactions [225]. Nevertheless, the required 65 ºC working temperature is less compatible with that in the CRISPR assay [226]. **(2) *Primer design***. Both PCR and RPA require only two primers [227]. On the other hand, the LAMP requires four to six primers that bind laterally to distinct sites of the DNA target [228]. Moreover, the

preamplification primer design is also restricted by the PAM (Cas12-based) [139, 220], and PFS (Cas13-based) [137] regions in the target. As a result, designing the LAMP primer is more challenging than the PCR and RPA assay. **(3)** ***Intellectual property (IP) protection***. PCR is one of the first introduced amplification methods, and the foundational patents for PCR expired in March of 2005 in USA and 2006 in Europe [229]. Therefore, various companies could offer PCR reagents across the world [230]. The LAMP assay was patented by Eiken chemical company (EP 1020534 B) from Japan, and this patent was expired in 2019 [231]. Currently, various companies such as New England Biolabs and Thermofisher in USA and OptiGene in Europe offer the required reagents for LAMP assay [232, 233]. On the other hand, RPA was introduced recently by TwistDx Limited from United Kingdom [231]. So far, only TwistDx and Alere offer the RPA reagents [234]. **(4)** ***Sensitivity***. The sensitivity of a diagnostic test is defined as the number of true positives (judged by the 'Gold Standard') over the total number received a positive result on this test. Li *et al.*[235] reviewed over 50 studies and compared the sensitivity of RPA with PCR. They showed that the sensitivity of RPA is only half as the PCR. ***(5) Specificity***. The specificity of a diagnostic test is defined as the number of true negatives (judged by the 'Gold Standard') over the total number received a negative result on this test. Although the sensitivity of the RPA was not comparable to PCR results, their specificity is comparable [235]. On the other hand, the complexity of primer design and the number of primers involved in LAMP reaction can lead to false positives from non-specific primer interactions [236]. **(6)** ***Instrument complexity***. To deploy the CRISPR-based diagnosis at the point of care, it is preferred to perform the assay with simple, easy-to-use, and cost-effective instruments [179, 188]. Both LAMP and RPA are isothermal assays that could be performed using simple equipment [237] or even equipment-free [238-240]. On the other hand, the PCR method relies on thermal cycling, making the instrumentation more complex.

6.3.2 Use of Cas proteins with higher k_{cat}

According to Eq. 6.5, FOM has a reverse relation with the activated Cas catalytic rate (k_{cat}). Assuming all other factors remain the same, Cas proteins with higher k_{cat} would decrease the FOM of the CRISPR system. Different Cas proteins have shown different trans-cleavage activity with various catalytic rates [212, 241-246]. **Figure 6-2b** presents the k_{cat} of different CRISPR effectors reported by different groups [139, 212, 216, 241, 243-247]. We observed four interesting features from these data. First, different Cas proteins have distinct k_{cat}. Cas13 effectors generally have a higher cleavage rate. For example, the average k_{cat} of LbuCas13a is around 1861 s^{-1}, much higher than the 279 s^{-1} for LbCas12a with the dsDNA activator. Second, similar Cas proteins from different bacteria show different cleavage activity where the average reported k_{cat} for LbCas12a is two orders of magnitude larger than AsCas12a. Third, different activators would result in different cleavage activities. In the case of Lbcas12a, the average k_{cat} of dsDNA activator cases are around 100 times higher than ssDNA activators. Forth, we observed a significant dispersion between the reported k_{cat} for a specific Cas protein. For instance, the k_{cat} of Lbcas12a with a dsDNA activator ranges from 0.08 to 1089 s^{-1}. This result shows that the combination of identical Cas proteins with different sequences of crRNAs would result in different trans-cleavage speeds. In addition, Nguyen *et al.*[241] showed that crRNA extensions could also affect the Cas trans-cleavage activity. Their finding showed that adding a 7-mer ssDNA extension to the 3'-end of crRNA would improve the trans-cleavage activity of LbCas12a proteins (more than two times). The results from **Figure 6-2b** suggest that different combinations of Cas proteins, target activators, and crRNAs should be optimized to obtain the highest k_{cat}. From these reported data in **Figure 6-2b**, selecting an optimal enzyme could reduce the FOM up to 3 orders of magnitude.

6.3.3 Use of multiple crRNA in the reaction

Another strategy to reduce the FOM of CRISPR systems is the use of multiple crRNAs. Combining different crRNAs with the Cas proteins would enhance the population of Cas/crRNA binary complex in the same reaction. Consequently, one target would activate multiple Cas proteins in the assay (**Figure 6-2c**). Considering that different crRNAs would have different kinetics properties (K_M and k_{cat}), the reaction speed with multiple crRNA can be written as:

$$v = N_1 A \sum_{i=1}^{n} \frac{k_{cat_i}[S]}{K_{M_i}+[S]} \quad (6.6)$$

where *n* is the number of crRNAs in the assay. Based on Eq. 6.6, increasing the number of crRNA could increase the cleavage rate.

Recent studies have utilized this technique to improve the CRISPR sensing performance. Fozouni *et al.* used three different crRNAs in developing an amplification-free method for detecting SARS-CoV-2 with CRISPR-Cas13a [246]. They showed that the LOD was improved 100-fold with the same CRISPR reaction time. In another study, Son *et al.* [248] utilized 26 different crRNAs in a Cas13a assay and improved the LOD 5 times. It is clear that utilizing multiple crRNAs could decrease the FOM value and improve the system performance. Nevertheless, the enhancement of the performance using this strategy is additive in nature (Eq. 6.6) and is unlikely to offer more than 2 orders of magnitude improvements. In addition, utilizing multiple crRNAs could complicate the assay design and increase the cost significantly.

6.3.4 Use of digital CRISPR

The FOM model also suggests that the CRISPR assay performance has a reverse relation with the reaction volume. Decreasing the reaction volume from microliter-scale to sub-nanoliter would improve the FOM of the system. In digital assays, bulk reaction volumes (~µL) are partitioned into thousands or millions of small reaction chambers with pL to fL volumes [249]. **Figure 6-2d** depicts the effect of reaction volume reduction on the product (cleaved reporter) concentration. As shown, the concentration of the product could increase up to 9 orders of magnitude. A few recent studies have utilized digital CRISPR to improve the performance of the assay. For instance, Tian *et al.* improved the LOD by five orders of magnitude by reducing the reaction volume to 15 pL[250]. Besides enhancing the FOM, another advantage of digitalized assays is the ability of absolute target quantification without the need for a standard curve [242, 251, 252]. Using Poisson statistics, the sample concentration can be estimated by -ln(1-p), where p is the ratio of the positive partitions over total partitions. Compared to other strategies, digital CRISPR could improve the FOM significantly (more than six orders of magnitude).

6.3.5 Use of sensitive readout system

Another parameter to improve the CRISPR FOM is the readout system's limit of detection C_{min}. Sensitive readout systems with lower C_{min} could help achieve lower FOM and better sensing performance (Eq. 6.5). While the majority of Cas12 or Cas13-based sensing systems were based on fluorescence signal [136, 169], colorimetric [168, 171], electrochemical [167, 212], and electronic readout [193, 223] were also explored for signal readout. **Figure 6-2e** compares the reported C_{min} of the different readout systems [253-257]. Among the optical methods, while simple signal readout systems such as the naked eye and portable fluorescent reader do not offer high

sensitivity compared to other methods, they are appealing in developing cost-effective point of care devices. In addition, electrical systems such as the field-effect transistor (FET) biosensors [254] and nanopore sensors [257] offer a lower limit of detection (lower than 1 pM) and the potential for developing an integrated system.

6.3.6 Comparison of FOM improvement strategies

Figure 6-2f summarizes the FOM improvement ratio using these strategies. The improvement ratio was estimated by using the FOM model (**Eq.5**) with reported LOD and CRISPR reaction times of previous studies. As shown, preamplification and digital assays are most effective in improving the FOM. They could significantly improve the FOM by orders of magnitude (~10^6 to 10^9). Moreover, utilizing a sensitive readout system could improve the FOM by 3 to 5 orders of magnitude compared to a simple readout like using a naked eye. In comparison, utilizing multiple crRNA or different Cas proteins is less effective, although they can still improve the FOM by about 2 orders of magnitude. It is noteworthy that multiple strategies could be implemented in one system to achieve lower FOM. For instance, Son *et al.* [248] combined digitalization and multiple crRNA in a single system and reduced the FOM by more than 6 orders of magnitude compared to the non-amplified Sherlock system [137].

6.4 Performance Benchmarking

Numerous CRISPR-based nucleic acid-sensing systems were reported in the past several years [188, 219, 258]. The FOM model described in Eq. 6.5 provides us with a tool to benchmark the performance of these different systems. We studied a total of 55 published works (**Table 6-1**) related to CRISPR-based nucleic acid-sensing up to this date (Dec. 2021) [135, 137, 139, 142, 167-

169, 172, 173, 175, 180-184, 189, 191, 211, 212, 218, 223-225, 242, 246, 248, 250, 256, 259-285]. It is noteworthy that while many more CRISPR-based sensing studies have been published in the past few years, we only include those with the LOD and CRISPR reaction time available.

Figure 6-3 shows the LOD versus CRISPR reaction time scattering plots along with the FOM-equivalent dash lines from 10^{-6} to 10^{-18} M·min. Note that the upper right corner represents a smaller FOM value and is thus preferred since it means lower LODs can be achieved by shorter CRISPR reaction times. We observed three important features in **Figure 6-3**. First, there is a general reverse relation between the LOD and reaction time. This is not surprising since the LOD×T is a constant for a CRISPR assay with constant properties (Eq. 6.5).

Table 6-1. Summary of the reported CRISPR-based diagnostics with LOD and CRISPR reaction time available.

Pathogen	Target	Effector	Readout System	Amplification	Amplification time (min)	CRISPR reaction time (min)	LOD (aM)	Ref.
Citrus greening disease	DNA	LbCas12a	Fluorescence	LAMP	40	5	16.6	[282]
African Swine Fever	DNA	LbCas12a	Fluorescence	LAMP	40	20	3.6	[173]
African Swine Fever	DNA	LbCas12a	Fluorescence	Non	Non	480	1e6	[135]
African Swine Fever	DNA	LbCas12a	Fluorescence	Non	Non	1440	1e5	[135]
HPV	DNA	LbCas12a	Fluorescence	RPA	15	60	16.6	[281]
African Swine Fever	DNA	LbCas12a	Fluorescence	RPA	30	60	10	[280]
SARS-CoV-2	RNA	LbCas12a	Fluorescence	RPA	30	30	16.6	[279]
HPV	DNA	LbCas12a	Fluorescence	RPA	10	60	10	[139]
Pseudorabies virus	DNA	LbCas12a	Fluorescence	Non	Non	15	1e8	[142]
Pseudorabies virus	DNA	LbCas12a	Fluorescence	PCR	45	15	10	[142]
SARS-CoV-2	RNA	LbCas12a	Fluorescence	RPA (one pot)	Non	40	80.3	[182]
P.aeruginosa	DNA	LbCas12a	Colorimetric	LAMP	15	30	3.4	[278]
HPV	DNA	LbCas12a	Colorimetric	PCR	50	30	240	[277]
Liver cancer	DNA	LbCas12a	Colorimetric	Non	Non	60	2e8	[168]

Ebola virus	RNA	LbCas12a	Fluorescence	RPA	40	240	10	[224]
HPV	RNA	LbCas12a	Electrochemical	Non	Non	60	3e7	[191]
Synthesized target	RNA	AacCas12b	Fluorescence	LAMP	30	30	10	[169]
SARS-CoV-2	RNA	AacCas12b	Fluorescence	RAA	30	30	16.6	[183]
Zika virus	RNA	LwCas13a	Fluorescence	RPA	120	60	2	[137]
Zika virus	RNA	LwCas13a	Fluorescence	Non	Non	60	5e5	[137]
SARS-CoV-2	RNA	LbuCas13a	Fluorescence	Non	Non	120	1.6e4	[246]
SARS-CoV-2	RNA	LbuCas13a (Multiple crRNA)	Fluorescence	Non	Non	120	166	[246]
Synthesized target	RNA	LbuCas13a	Fluorescence	Non	Non	120	1e6	[276]
Synthesized target	RNA	LbuCas13a	Fluorescence	Non	Non	20	3.7e9	[256]
Zika Virus	RNA	LbuCas13a	Fluorescence	RPA	20	60	6	[211]
Cytomegalovirus	DNA	LwCas13a	Fluorescence	RPA	50	180	0.6	[275]
White Spot Syndrome	RNA	Cas13a	Colorimetric	RPA	40	180	1.6	[175]
Various tumor cells	mRNA	LbuCas13a	Electrochemical	EXPAR	30	30	1e3	[212]
SARS-CoV-2	RNA	AsCas12a	Nanopore	PCR	30	30	22.5	[223]
SARS-CoV-2	RNA	LbCas12a	Fluorescence	LAMP	30	10	16.6	[180]
SARS-CoV-2	RNA	AsCas12a	Fluorescence	LAMP	30	30	8.3	[181]
SARS-CoV-2	RNA	LwaCas13a	Fluorescence	RPA	20	60	16.6	[184]
SARS-CoV-2	RNA	LbCas12a	Fluorescence	RPA (one pot)	Non	60	1.5	[274]
African Swine Fever	DNA	LbCas12a	Fluorescence	Non	Non	60	30	[242]
SARS-CoV-2	RNA	LbuCas13a	Fluorescence	Non	Non	60	10	[250]
SARS-CoV-2	RNA	Cas12a	Fluorescence	RPA (one pot)	Non	60	1.6	[273]
SARS-CoV-2	RNA	LbCas12a	Fluorescence	LAMP	20	15	16.6	[272]
SARS-CoV-2	RNA	LbCas12a	Fluorescence	DAMP (one pot)	Non	50	8.3	[218]
HPV	DNA	AaCas12b	Fluorescence	RPA	10	180	1	[271]
HPV	DNA	LbCas12a	Electrochemical	Non	Non	60	5e7	[189]
SARS-CoV-2	RNA	AapCas12b	Fluorescence	LAMP (one pot)	Non	60	3.3	[225]
Different Viruses	RNA	LwaCas13a	Fluorescence	PCR or RPA	20	180	0.9	[270]
miR-19b and miR-20a	mRNA	LwaCas13a	Electrochemical	Non	Non	15	1e7	[167]
SARS-CoV-2	RNA	LbCas12a	Colorimetric	RPA	30	20	8.3	[269]

Listeria monocytogenes	DNA	LbCas12a	Electrochemical	RAA	30	90	0.68	[268]
SARS-CoV-2	RNA	LbCas12a	Fluorescence	RPA	30	10	16.6	[267]
SARS-CoV-2	RNA	LwaCas13a	Fluorescence	PCR	22	30	332	[172]
SARS-CoV-2	RNA	LbuCas13a	Fluorescence	Non	Non	15	8.3	[248]
SARS-CoV-2	RNA	LbuCas13a multiple crRNA	Fluorescence	Non	Non	15	1.6	[248]
SARS-CoV-2	RNA	LbCas12a	Colorimetric	RPA	20	60	1e5	[266]
DENV-4	DNA	AsCas12a	Electrochemical	Non	Non	120	1e3	[265]
BRCA-1	DNA	AsCas12a	Fluorescence	Non	Non	30	1e4	[264]
HPV	DNA	LbCas12a	Fluorescence	Non	Non	60	1e5	[263]
Bacillus anthracis gene	DNA	LbCas12a	Fluorescence	Non	Non	15	1e7	[262]
Synthesized target	DNA	LbCas12a	Fluorescence	Non	Non	60	1e5	[261]
SARS-CoV-2	RNA	LbCas12a	Fluorescence	RPA	15	25	83	[260]
Staphylococcus aureus	DNA	LbCas12a	Colorimetric	RAA	20	20	1	[259]
SARS-CoV-2	RNA	LbCas12a	Fluorescence	RPA (one pot)	Non	60	2	[283]
SARS-CoV-2	RNA	LbCas12a	Fluorescence	LAMP	10	25	6.5	[284]
SARS-CoV-2	RNA	LbCas12a	Fluorescence	LAMP	40	10	26	[285]

These aggregated data confirm a tradeoff between the assay's LOD and the required reaction time. Second, these data points can be divided into six categories (shown as oval in **Figure 6-3**): (1) ensemble without amplification, (2) ensemble with amplification, (3) ensemble using multiple crRNA, (4) digital without amplification, (5) digital with amplification, and (6) digital using multiple crRNA.

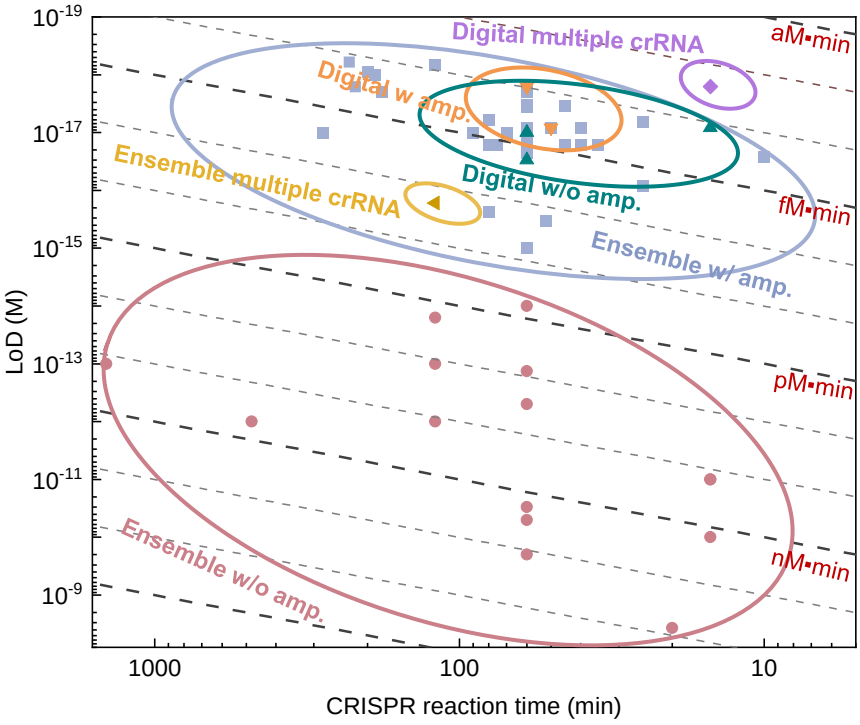

Figure 6-3.. Scattering plot of the limit of detection versus CRISPR reaction time for a total of 55 CRISPR-based sensing studies, along with the FOM equivalent dash lines from 10^{-18} to 10^{-6} M·min. The data points were divided into six categories separated by the ovals in the figure. The top right side of the figure indicates a lower FOM and thus a better CRISPR sensing performance. Within each category, the data points do not perfectly reside on a single line (LOD×T = Constant). This is because the used Cas protein, crRNA, target, amplification method, and readout system could vary within each category.

The category of the ensemble without amplification represents the plain vanilla version of the CRISPR-based sensing. The data points within this category show the worst FOM (1 nM·min to 1 pM·min, red oval in **Figure 6-3**). The data points from all other categories show significant FOM improvements as seen from the up-right shift of these populations. Compared to the plain vanilla version, preamplification or digitalization strategies could improve the CRISPR sensing FOM by 6 to 9 orders of magnitude, consistent with the predictions in **Figure 6-2f**. Third, FOM in the order of 1 fM·min to 10 fM·min could be achieved within the digitalization categories with or without

preamplification. This means that a target concentration of 100 aM to 1 fM could be obtained in 10 min CRISPR reaction time using digital assays without amplification, which was experimental validated [218, 247, 273]. The best FOM performance was observed by combining digital assay and multiple crRNA cases where FOM deceased to 24 aM·min [248]. As a result, digital CRISPR assay provides the most appealing method for amplification-free CRISPR-based nucleic acid-sensing.

6.5 Summary

In summary, we proposed and developed a figure of merit (FOM) for CRISPR-based nucleic acid-sensing systems to quantitatively benchmark different methods and explore the performance improvement strategies. The CRISPR-based nucleic acid-sensing FOM, defined as the product of the LOD and CRISPR reaction time, is analytically established by connecting the LOD and reaction time to various reaction setup properties. Based on the developed model, we found that the CRISPR sensing FOM was linked to the reaction volume, the sensitivity of the readout system, preamplification efficiency, and Cas protein enzymatic properties. We evaluated different strategies to reduce the FOM and improve the performance of the CRISPR systems, including the use of preamplification, novel Cas proteins with higher k_{cat}, multiple crRNA, digital CRISPR, and sensitive readout systems. Comparison of FOM improvement strategies showed that preamplification and digital CRISPR have the highest impact on the FOM (up to 9 orders of magnitude). We benchmarked the FOM performances of 55 existing studies and found that the effectiveness of these strategies on improving the FOM is consistent with the model prediction. In particular, we found that digitalization is the most promising amplification-free method for achieving comparable FOM performances (~1 fM·min) as those using preamplification.

CHAPTER 7 STAMP-BASED DIGITAL CRISPR-CAS13A (STAMP-DCRISPR) FOR AMPLIFICATION-FREE QUANTIFICATION OF HIV-1 PLASMA VIRAL LOAD

In this chapter, we report the development of a self-digitalization through automated membrane-based partitioning (STAMP) technique to digitalize the CRISPR-Cas13 assay (dCRISPR) for amplification-free and absolute quantification of HIV-1 viral RNAs. The analytical performances of STAMP-dCRISPR were evaluated with synthetic HIV-1 RNA, and it was found samples spanning 4 orders of dynamic range between 100 aM to 1 pM can be quantified as fast as 30 min. We also examined the overall assay from RNA extraction to STAMP-dCRISPR quantification with spiked plasma samples. The overall assay showed a resolution of 42 aM at a 90% confidence level. Finally, a total of 20 clinical plasma samples from patients were evaluated with STAMP-dCRISPR. The obtained results agreed well with the RT-qPCR. Our result demonstrates a new type of easy-to-use, scalable, and highly specific digital platform that would offer a simple and accessible platform for amplification-free quantification of viral RNAs, which could be exploited for the quantitative determination of viral load for an array of infectious diseases.

7.1 Introduction

Acquired immunodeficiency syndrome (AIDS) caused by human immunodeficiency virus (HIV) infection, a notorious fatal epidemic, has led to millions of deaths worldwide since its origin [286]. Although AIDS-related annual mortality has reduced by 33% in the past decade due to the application of antiretroviral therapies and advanced HIV diagnosis, the number of new HIV infections remains high (for instance, 1.5 million in 2020 globally), which is estimated to cost billions of dollars for AIDS therapy [287]. Since AIDS patients at early stages tend to present no

obvious symptoms but can still be infectious, early awareness of infection enables timely treatment for exposed patients and prevents further transmission [288]. Viral load quantification of the HIV-1 RNA not only identifies the progression of the disease in a patient but also could be employed to monitor the trends in large populations of patients [289-291]. Therefore, nucleic acid tests (NAT) that have been utilized for viral load quantification hold tremendous promise in AIDS diagnosis [292]. One of the major techniques for viral load quantification of HIV is the reverse transcriptase quantitative polymerase chain reaction (RT-qPCR) due to its accessibility and high sensitivity [289, 293]. Although RT-qPCR has been the gold standard for detecting the HIV-1 RNA [294, 295], the emerging clustered regularly interspaced short palindromic repeats (CRISPR) based technology has taken immense attention for nucleic acid tests due to its high sensitivity and specificity [213, 221].

Since the discovery of Cas9 proteins for gene editing, the CRISPR technology has taken center stage in biotechnology [206]. Recently, the discovery of the collateral cleavage in other Cas proteins like Cas12 [142] and Cas13 [137] made it possible to translate the sequence-specific targeting to other detectable signals, which has led to the increasing emergence of CRISPR-mediated biosensors [130, 136-138, 166-170, 189, 193, 211, 212, 223]. Among these CRISPR-mediated assays, a preamplification step is often required to boost the limit of detection and time to results performance [134, 170]. However, preamplification complicates the assay setup, increases the assay time, raises the risk of contamination, and could introduce false-negative or -positive results due to amplification errors [179]. We previously investigated different strategies to boost the CRISPR assay performance [296], such as the use of Cas proteins with higher cleavage activity [200], the use of multiple crRNA in the reaction [246, 248], the use of a sensitive readout system [257], and the reaction digitalization [218, 242, 247, 248, 250, 273, 274, 297-302]. Among these techniques, we found only the digitalization method could match the limit of detection

(attomolar range) and the fast turnaround time (less than 1 hour) of preamplification-coupled CRISPR assays [296].

So far, various digitalization techniques have been introduced. For instance, water in oil droplets generated by T-junction [18], flow focusing [19, 20], and centrifugation [21] have been used for digitalization. Furthermore, digital assays have been performed inside numerous microchambers fabricated by polydimethylsiloxane (PDMS) or glass chambers. Partitioning of the assay inside these chambers has been achieved using vacuum [22, 23], pressure [24], SlipChip [25], hydrophilic patterns [26, 27], or self-digitization [28]. While these techniques have been optimized and improved considerably, complicated fluidic control systems and complex micro and nanofabrication processes are required for them. Therefore, developing a platform to eliminate complicated fluidic control and fabrication processes would be desirable for highly accessible digital assay systems.

In this study, we demonstrated a self-digitalization method through an automated membrane-based partitioning (STAMP) and developed a STAMP-based digital CRISPR-Cas13a (STAMP-dCRISPR) for the absolute quantification of HIV-1 viral load. We first established a stamping technique to digitalize the Cas13a assay inside a commercial track-etched polycarbonate (PCTE) membrane without a complicated fluidic control process (*e.g.*, pump, vacuum, and valve). To optimize the Cas13a assay, we studied the effect of different CRISPR RNA (crRNA) design and assay reaction time on the sensing performance. The absolute quantitative performance, the limit of detection and the dynamic range were evaluated by quantifying the synthetic HIV-1 RNA at different concentrations. We also examined the overall assay from plasma RNA extraction to STAMP-dCRISPR with spiked HIV-1 plasma samples. Finally, the clinical applicability of the STAMP-dCRISPR was demonstrated in the absolute quantification of 20 HIV-1 patient samples

7.2 Methods

7.2.1 STAMP device fabrication

The PMMA holders were prepared by cutting the PMMA sheets with 1/8" thickness using a laser cutter machine (Universal Laser System). Two pieces of PMMA with the dimensions of 24×24 mm and 35×35 mm with inner circles of 11 and 13 mm were fabricated and attached using acrylic cement (United States Plastic Corporation, cat# 46872). To handle the track-etched polycarbonate membranes (Sterlitech Corporation, cat# PCT25025100), we utilized a vacuum pen (Pen-vac pro series V8910). The PVP layer of the membranes was removed by dipping the membranes in 10% acetic acid for 30 min, followed by heating to 140 °C for 60 min in a vacuum oven. Afterward, the membrane was attached to the holder using adhesive tapes (70 μm thickness). We used mineral oil purchased from Sigma-Aldrich (cat# 69794-500ML) to seal the membrane.

7.2.2 Automated data acquisition and analysis

The fluorescent images were taken using a fluorescent microscope (Nikon ECLIPSE Ti). The integration time was set as 6 s to image the membrane. To cover the whole membrane, a motorized stage (Prior OptiScan) was utilized, and 24 images were taken to cover the membrane. A stitching algorithm was employed to obtain the whole fluorescent images of each membrane. Afterward, MATLAB (MathWorks) software was used to implement a *k*-means clustering algorithm to differentiate between positive and negative pores.

7.2.3 crRNA design and selection

The optimal protospacer length observed for Cas13a is 28 nucleotides along [303]. In addition, Abudayyeh et al. analyzed the flanking regions of protospacers and found that sequences starting with a G immediately after the 3' end of the protospacer were less effective relative to all other nucleotides (A, U, or C) [304]. Therefore, considering the protospacer-flanking site (PFS), 28 nucleotide crRNA protospacer sequences were designed by targeting the HIV-1 type B sequence downloaded from the NCBI website. In the next step, 496 complete HIV sequences deposited in NCBI server were downloaded on 9/14/2021. These sequences were aligned using SnapGene software. We searched designed crRNAs against the aligned sequence with more than 80% similarity and chose five matched crRNAs. It should be mentioned that we used a previously validated sequence for the direct repeat region of the crRNA as follows: 5'-GAUUUAGACUACCCCAAAAACGAAGGGGACUAAAAC -3' [170].

7.2.4 Cas13 reaction mixture

The designed crRNAs were synthesized by Integrated DNA Technologies. The crRNAs were resuspended in pH 7.5 buffer and stored at -80 ºC. LwaCas13a proteins were purchased from MCLAB (cat# CAS13a-100). Cas13a and crRNA were mixed in 1×PBS to form the non-activated Cas13a/crRNA at room temperature for 20 min and stored at -80ºC. In the cleavage reaction, the 2 µL of non-activated Cas13a/crRNA complex was mixed with the 2 µL of RNA target in 9.5 µL of water, 0.5 of Murine RNase Inhibitor (purchased from New England Biolabs, cat# M0314S), 2 µL of FQ-labeled reporter (RNaseAlert substrate purchased from IDT, cat# 11-04-02-03), and 4 µL of a CRISPR buffer consisting of 20 mM HEPES-Na pH 6.8, 50 mM KCl, 5 mM $MgCl_2$, and 5%

glycerol. Afterward, the mixed solution was incubated in a microplate (for bulk assays) or PCTE membranes (for digital assays) at 37ºC for different reaction times.

7.2.5 Bulk Cas 13a assay

For bulk assay fluorescent signal acquisition, the 20 µL CRISPR reaction mix was incubated inside a 384 well black plate (purchased from ThermoFisher, cat# 142761). The fluorescent signal was measured every 30 s for different reaction times using a microplate reader (Tecan plate reader infinite 200 PRO). The excitation wavelength was set as 480 nm with a bandwidth of 9 nm, and the emission wavelength was set as 530 nm with a bandwidth of 20 nm. The temperature was fixed at 37ºC. The gain and integration time were set as 110 and 20 µs, respectively.

7.2.6 STAMP-dCRISPR assay

For the STAMP-dCRISPR, the CRISPR reaction mix was incubated inside the PCTE membrane using STAMP. In the first step, 8 µL of reaction mix was dropped on top of a glass surface, and the stamp was slowly placed on top of it. After 60 seconds, we started the second step and sealed the top surface of the membrane by adding 60 µL of mineral oil on top of the membrane. The stamp was peeled off from the glass surface in the third step. In the final step, the stamp was placed on top of the system base, which consisted of a glass substrate and a double-sided tape filled with mineral oil to seal the bottom side of the membrane. The sealed system was placed on top of a hot plate (Fisherbrand Isotemp Hot Plate) at 37 °C for different reaction times.

7.2.7 Contrived plasma mock sample and clinical samples

To prepare the contrived plasma mock sample, different copies (1000, 1500, 2000, 2500, and 3000) of HIV viral particles (Seraseq, cat# 0740-0004) were mixed in 140 µL of fresh, healthy plasma (Research Blood Components). After mixing, the samples were preserved at -80 °C. The clinical HIV plasma samples were obtained from Hershey Medical Center by an approved institutional review board (IRB) of the Pennsylvania State University. All samples were coded to remove information associated with patient identifiers. The plasma samples were stored at -80 °C before the examination.

7.2.8 Viral RNA extraction from plasma

To extract the RNA a column-based RNA extraction kit purchased from Qiagen (cat# 52904) was utilized. The procedure is optimized for samples with a volume of 140 µL. The sample is first lysed under the highly denaturing conditions provided by a viral lysis buffer. In addition, we added carrier RNA to the lysis buffer, which enhances the binding of viral RNA to the kit membrane and reduces the chance of viral RNA degradation. Afterward, the purification was carried out in 3 steps using a standard centrifuge (Eppendorf centrifuge 5425). We washed the sample using ethanol and 2 washing buffers provided by the kit. In the final stage, we used 10 uL of nuclease-free water (BioLabs, cat# 52904B1500S) as an elution buffer to obtain the extracted RNAs from the membrane.

7.2.9 HIV-1 RT-PCR assay

We used a one-step, two-enzyme RT-PCR protocol for HIV-1 assays. The reaction has a total volume of 20 µL, consisting of 5 µL TaqMan Fast Virus 1-Step Master Mix (cat# 4444432, Thermofisher), 1.2 µL forward primer (0.6 µM), 1.2 µL reverse primer (0.6 µM), 0.5 µL probe (0.25 µM), and 10 µL RNA templates as well as 2.1 µL PCR grade water. We used a previously validated HIV-1 RT-PCR primer set (Forward primer: 5'-CATGTTTTCAGCATTATCAGAAGGA -3', and Reverse primer: 5'-TGCTTGATGTCCCCCCACT -3') [305]. In addition, the probe was selected as 5'- FAM-CCACCCCACAAGATTTAAACACCATGCTAA-Q -3', where Q indicates a 6-carboxytetramethylrhodamine group quencher conjugated through a linker arm nucleotide. The following thermal cycling sequences performed the RT-PCR: 50 ℃ for the first five minutes without repeating to reverse transcription reactions which convert HIV-1 RNA into cDNA, then 95℃ for 20 seconds without repeating to initiate amplification, followed by 46 cycles of amplification stage consisting of 3 seconds of 95 ℃ and 30 seconds of 60℃ thermal-cycling.

7.3 Results and discussion

7.3.1 STAMP device and characterization

In order to achieve self-digitalization without complicated fluidic control, we developed the STAMP method to digitalize the assay. In this method, a commercial polycarbonate track-etched (PCTE) membrane was utilized for digitalization. This type of commercial membrane consists of a high density of micro/nanopores with uniform pore sizes ranging from 10 nm to 30 µm [29]. **Figure 7-1a** illustrates a top and side view of the assembled stamp device where the membrane is

sandwiched between a polymethyl methacrylate (PMMA) holder and a thin tape (70 μm thickness). In addition, **Figure 7-1a** depicts an image of the transparent and flexible PCTE membrane with a diameter of 1.3 cm. We characterized the pore size distribution by examining 5 different membranes. As shown in **Figure 7-1b**, the average pore size was measured as 24.6±1.6 μm, and the pore density was determined to be 9895±531 pores/cm^2.

The operation of the stamp device only requires 4 simple manual steps. In the first step (**Figure 7-1c-i**), the analyte sample droplet was deposited on top of a glass surface, and the stamp was slowly placed on top of it. To ensure the filling process, only 8 μL of the sample was required, which is 33% more than the spacing volume of 6 μL between the membrane and glass surface. Once in contact, the surface tension between the sample and pore walls causes a capillary action that forces the sample into the membrane's pores. After 60 seconds of soaking, 60 μL of mineral oil was added to the top chamber to seal the top surface of the membrane (**Figure 7-1c-ii**). An inspection of the stamp confirmed that all pores were successfully filled despite that there were excessive liquids underneath the membrane (**Figure 7-2a**). To remove these excessive samples, one only needs to peel off the stamp from the glass surface (**Figure 7-1c-iii**). The as-purchased membranes were coated with polyvinylpyrrolidone (PVP) which renders the surface hydrophilic. To facilitate the excessive liquid removal, this hydrophilic coating was removed by dipping the membranes in 10% acetic acid for 30 minutes and heating at 140 °C for 60 minutes in a vacuum oven.

Figure 7-1d shows that the contact angle increased from 48 to 79 degrees after this chemical treatment, confirming the PVP removal process. Since the glass surface is hydrophilic and the PCTE membrane surface is hydrophobic, the excess liquid would remain on the glass and be removed from the membrane surface. In the pore areas, the surface tension overcomes the liquid intermolecular forces and holds the sample inside the pores. An examination of the stamp confirms

this process for effectively removing the excess liquid while maintaining the digitalized samples (**Figure 7-2b**). Lastly, the stamp was placed on top of a customized base with prefilled mineral oil (**Figure 7-1c-iv**) to form a fully sealed digital system for further reaction.

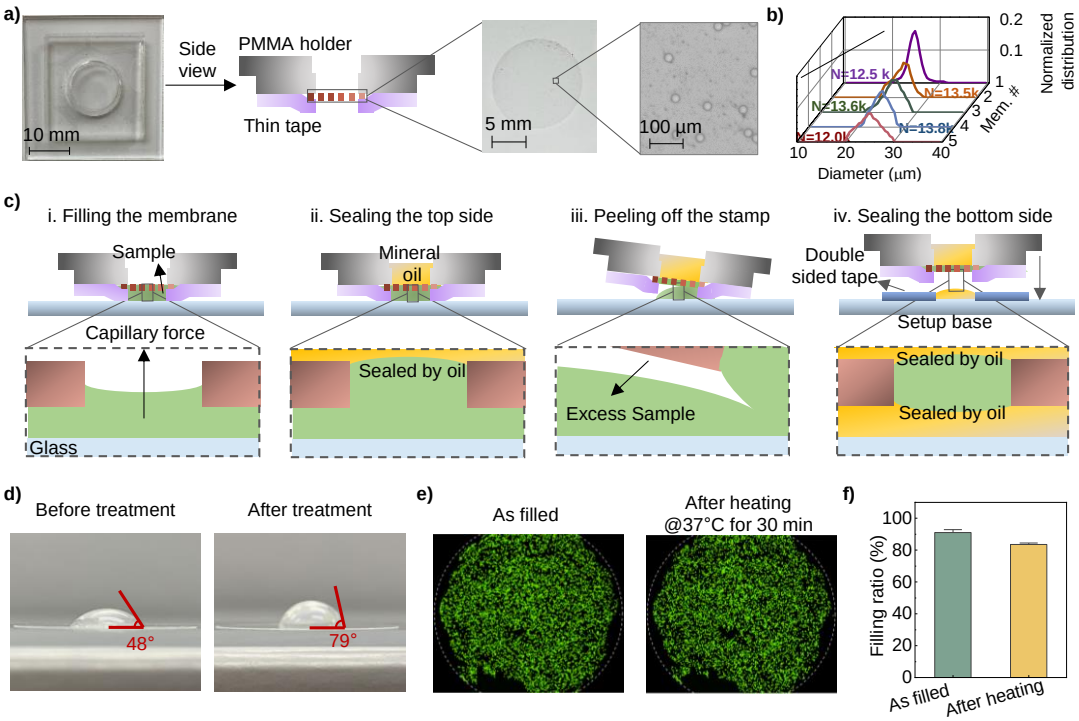

Figure 7-1. STAMP device characterization and filling process. a) Different components of the STAMP system along with a top-side view of the assembled device and images of the commercial PCTE membranes. b) Pore size distribution of five different membranes and their total number of pores. d) STAMP process. **i.** The process starts by placing the stamp device on top of the sample. **ii.** The top side of the system is sealed by adding mineral oil. **iii.** The stamp is removed from the glass to eliminate the excess liquid from the bottom of the membrane. **iv.** The stamp is placed on the setup base (consisting of glass, double-sided tape, and mineral oil) to seal the bottom side of the system. d) Chemical treatment to remove the polyvinylpyrrolidone (PVP) coating from the PCTE membrane. The contact angle of a water droplet on top of the membrane increased from 48 to 79 degrees after treatment, confirming the effectiveness of the PVP removal process. e) Fluorescent images of a membrane demonstrating the filling of the membrane using STAMP before and after 30 minutes of heating at 37 °C. All filled pores are labeled with a filled green circle to demonstrate the filling process. f) Measured filling ratio of the membranes before and after 30 minutes of heating at 37 °C. We used a bright image of the membrane to estimate the total number of pores.

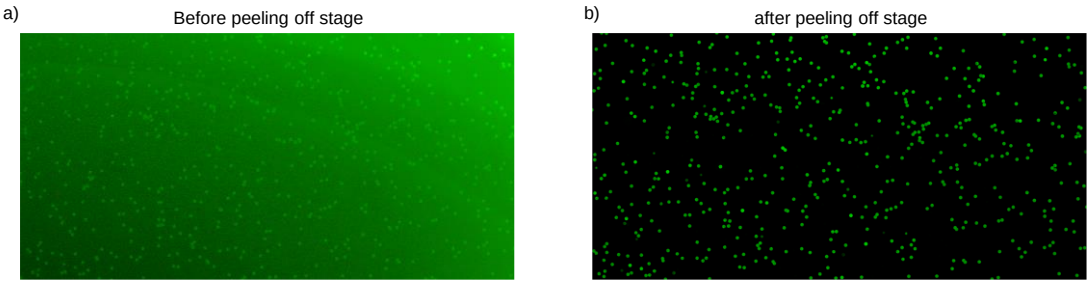

Figure 7-2. Effect of peeling-off stage on the excess sample removal process. Fluorescent images of the membrane a) before and b) after the peeling-off stage of the stamping process. These images confirmed the excess sample removal process in the peeling-off stage.

To evaluate the membrane filling process and evaporation under heating procedures, we measured the filling ratio (total number of filled pores per total number of pores) of the final sealed membrane before and after 30 minutes of heating at 37 °C. **Figure 7-1e** and **Figure 7-1f** illustrate representative fluorescent images of the membrane and the measured filling ratio before and after the heating procedure. The average filling ratio before the heating was measured as 91.09%. Usually, some parts of the membranes do not fill, which could be caused by the sample intermolecular forces overcoming the surface tension when the stamp is removed from the glass. After 30 minutes of heating at 37 °C, we observed evaporations in some parts of the membrane where the filling ratio reduced to 83.54%. Those unfilled pores show no fluorescence signals at all and can be easily distinguished from the pores with negative reactions (which exhibit weak fluorescence signals, **Figure 7-3**). To improve the accuracy of the absolute quantification, we only considered the filled pores as the total number of reactions in our system.

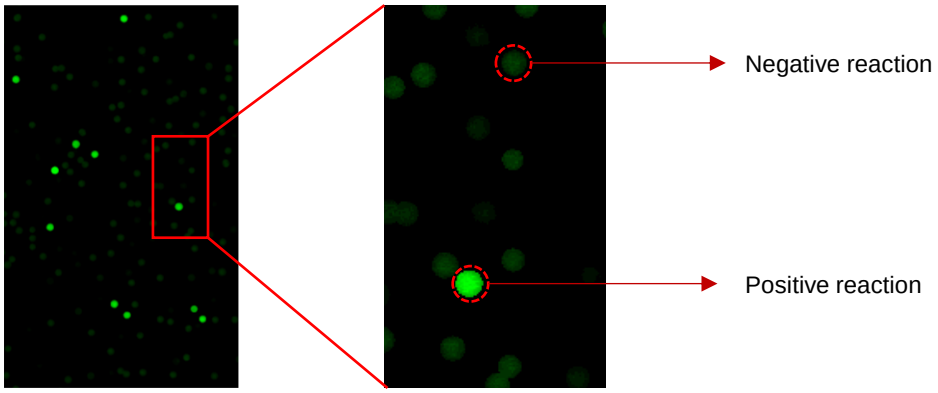

Figure 7-3. Typical fluorescent signals from a negative and positive reaction. Fluorescent image of part of a membrane demonstrating typical fluorescent signals from a negative and positive reaction. The negative reaction containing the unquenched FAM reporters also shows a weak fluorescence signal in our fluorescent images.

7.3.2 Automated HIV-1 STAMP-dCRISPR system and its noise floor

After the development of the STAMP device, we set out to develop a platform to utilize the STAMP for running the digital CRISPR (dCRISPR) assay for HIV-1 viral load quantification. The Cas13a reaction mix was digitalized inside the membrane using the STAMP technique (**Figure 7-4a**). With binding to the specific RNA-guided target, Cas13a proteins become activated and perform trans-cleavage on the surrounding FQ-labeled single-stranded reporter [142] (**Figure 7-4b)**.

Fluorescence images of the membranes were taken by a fluorescence microscope with a motorized stage to cover the whole membrane (**Figure 7-4c**). The light source wavelength was filtered to 480 nm using an excitation filter and redirected to the sample using a dichroic mirror. Afterward, the emitted light from the sample was obtained by CMOS camera after filtration. 24 images were taken and stitched together to cover the whole membrane area (**Figure 7-4d**). The acquired images were analyzed to distinguish positive from negative pores based on the fluorescent intensity emitted from each pore. We utilized a *k*-means clustering algorithm to differentiate between positive and

negative pores [306] (**Figure 7-4e, Figure 7-5**). The Poisson statistics was utilized to quantify the number of HIV-1 RNA targets without external references.

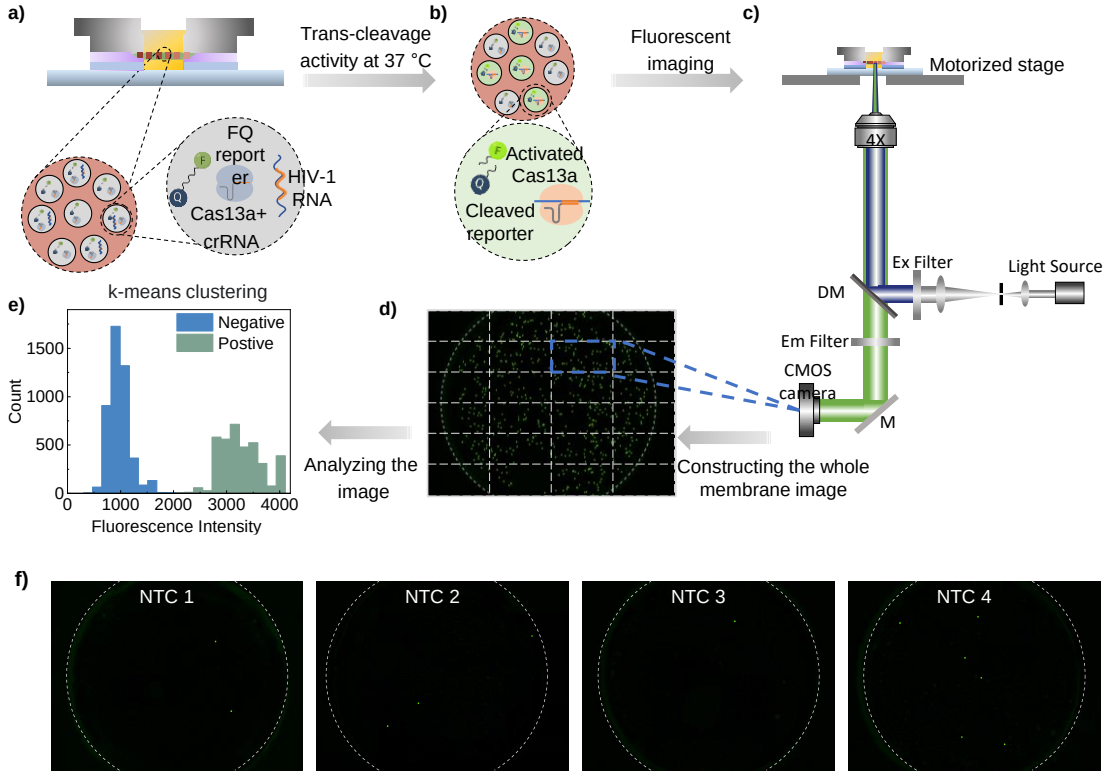

Figure 7-4. Utilization of STAMP device for running the digital CRISPR assay for HIV-1 viral load quantification. a) Digitalization of CRISPR-Cas13a assay including HIV-1 RNA, Cas13a and crRNA complex, fluorophore quencher (FQ)-labeled single-stranded RNA reporters. b) Trans-cleavage activity of the activated Cas13a proteins (after binding with HIV-1 RNAs) on non-target surrounding FQ RNA reporters. Cleavage of the reporters results in the FAM fluorescence illumination. c) Fluorescent imaging setup. d) The fluorescent image of a whole membrane stitched from 24 images taken by the microscope. e) Clustering the positive and negative pores based on their fluorescent intensity using a k-means clustering algorithm. f) Fluorescent images illustrating positive and negative pores at 4 negative control cases. All positive pores are labeled with a filled green circle for better demonstration.

Fluorescence images of the membranes were taken by a fluorescence microscope with a motorized stage to cover the whole membrane (**Figure 7-4c**). The light source wavelength was filtered to 480. With n total number of reactions, the positive pore ratio (PPR) is defined as $PPR=m/n$, where m is

the number of positive reactions. Based on the Poisson statistics, the concentration of the sample could be estimated as:

$$C = \frac{\lambda}{V_p} = -\frac{\ln(1-PPR)}{V_p} \quad (7.1)$$

where λ is the expected number of targets in each pore, and V_p is the average volume of the pores.

We examined the no-target control (NTC) cases to obtain the background noise of STAMP-dCRISPR. **Figure 7-4f** presents the fluorescent images of the 4 NTC cases. While no targets were added in these cases, few positive pores were detected. Multiple factors could cause the background noise in our systems, such as non-specific reporter cleavage [307, 308], imaging [309, 310], and post-processing inaccuracy [309]. The system background noise (defined as $\mu_{NTC}+3\sigma_{NTC}$) was measured as 0.00093, where μ_{NTC} and σ_{NTC} are the averages and standard deviation of the *PPR* in the negative cases measured.

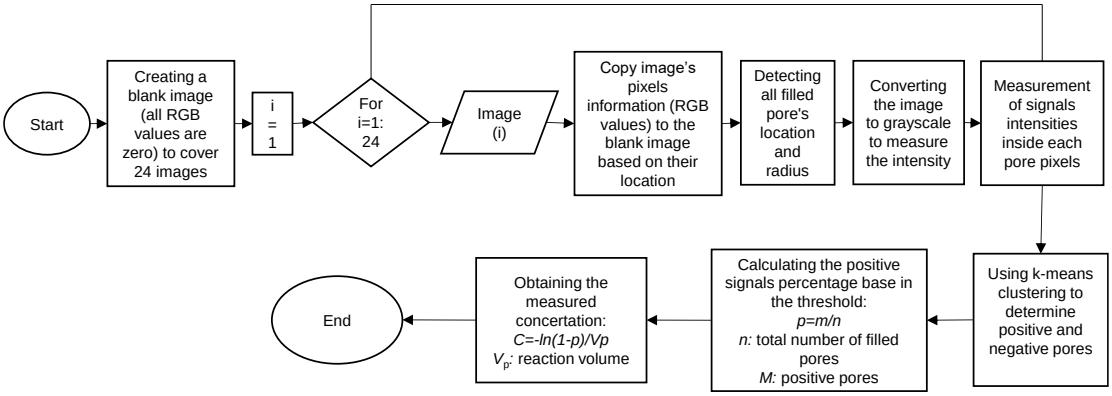

Figure 7-5. Algorithm for acquiring the fluorescent intensity and stitching of the images. The algorithm runs through 24 images and identifies the pixels inside the filled pores in each case. Afterward, The fluorescent intensity of each pore is calculated by combining the intensity of the pixels inside the pores. After examining all 24 images, a k-means algorithm would classify the positive and negative pores based on the fluorescent intensity. Finally, the concentration of the sample would be calculated using Poisson statistics.

7.3.3 Design and optimization of HIV-1 Cas13 assay

To optimize the Cas13 crRNA design, we initially designed five crRNAs along the HIV-1 genome (red rectangles in **Figure 7-6a**, **Table 7-1**). In addition, we synthesized five 100 nucleotides target to cover each designed crRNA (colored rectangles in **Figure 7-6a**, **Table7-2**). We cross-react the crRNAs with target samples and no target samples in a total of 30 reactions to validate the assay's specificity.

Table 7-1. Detailed sequences of crRNAs

Description	Sequence
HIV-1 crRNA 1	GAUUUAGACUACCCCAAAAACGAAGGGGACUAAAACGGCUAUACAUU CUUACUAUUUUAUUUAA
HIV-1 crRNA 2	GAUUUAGACUACCCCAAAAACGAAGGGGACUAAAACAAACCUCCAAU UCCCCCUAUCAUUUUUG
HIV-1 crRNA 3	GAUUUAGACUACCCCAAAAACGAAGGGGACUAAAACGCUUUUAUUUU UUCUUCUGUCAAUGGCC
HIV-1 crRNA 4	GAUUUAGACUACCCCAAAAACGAAGGGGACUAAAACCUAAUUUAUCU ACUUGTTCAUUUCCUCC
HIV-1 crRNA 5	GAUUUAGACUACCCCAAAAACGAAGGGGACUAAAACUCCCUGUAAUA AACCCGAAAAUUUUGAA

Table 7-2. Detailed sequences of targets

HIV-1 Target 1 fragment	TAGGAGAAATTTATAAAAGATGGATAATCCTGGGATTAAATAAAATAG TAAGAATGTATAGCCCTACCAGCATTCTGGACATAAGACAAGGACCAA AG
HIV-1 Target 2 fragment	ATTAGAAGAAATGAGTTTGCCAGGAAGATGGAAACCAAAAATGATAGG GGGAATTGGAGGTTTTATCAAAGTAAGACAGTATGATCAGATACTCATA G
HIV-1 Target 3 fragment	AAAGCCAGGAATGGATGGCCCAAAAGTTAAACAATGGCCATTGACAGA AGAAAAAATAAAAGCATTAGTAGAAATTTGTACAGAGATGGAAAAGGA AG
HIV-1 Target 4 fragment	TCTATCTGGCATGGGTACCAGCACACAAAGGAATTGGAGGAAATGAAC AAGTAGATAAATTAGTCAGTGCTGGAATCAGGAAAGTACTATTTTTAGA T
HIV-1 Target 5 fragment	ACAAACTAAAGAATTACAAAAACAAATTACAAAAATTCAAAATTTTCG GGTTTATTACAGGGACAGCAGAAATCCACTTTGGAAAGGACCAGCAAA GC

Figure 7-6b shows the fluorescent intensity over 60 minutes of Cas13a reactions. An increase in fluorescent intensity was only observed in cases where targets and crRNAs were matched, confirming the assay's specificity. In the case of crRNA 3, no significant fluorescent signal increase was observed, which is likely due to the low trans-cleavage activity [246]. In addition, crRNA1 and 4 showed the highest trans-cleavage activity among the cases where the higher fluorescent intensity was observed after 60 minutes of reaction.

To further compare the performance of the Cas13a assay using crRNA 1 and 4, we performed a Michaelis-Menten kinetic study on the system. **Figure 7-6c** presents the measurements of reaction rates for the trans-cleavage activity of Cas13a proteins for crRNA1 and 4. Each data point is a measured initial reaction velocity (nM/s) for a titrated reporter concentration.

Figure 7-7 shows the details of cleaved reporter concentration and measurements of cleavage speed. In order to extract the kinetic properties of Cas13 proteins using crRNA1 and 4, the curves in **Figure 7-6d** were fitted using nonlinear regression based on the Michaelis-Menten equation:

$$V = k_{cat}\, E_0 \frac{[S]}{K_M + [S]} \quad (7.2)$$

where E_0 is the target-activated Cas/13−cRNA complex concentration, [S] is the reporter concentration, k_{cat} is the catalytic turnover rate of the enzyme, and K_M is Michaelis constant. For the reaction using crRNA 1 and 4, the catalytic rate of 29.49 s^{-1} and 60.32 s^{-1} were measured, respectively. The assay using crRNA1 displayed a reaction with a higher cleavage rate. Therefore, crRNA1 was chosen for our digital assay to obtain a faster signal. In addition, we also quantified the bulk assay limit of detection using crRNA 1 and 4. As shown in **Figure 7-6d**, HIV-1 Cas 13 assay using crRNA1 showed a better limit of detection of ∼20 pM compared to ∼100 pM when using crRNA4. The pM range of limit of detection in an amplification-free bulk Cas13 assay is on par with the previously reported Sherlock assay (∼50 pM) [137].

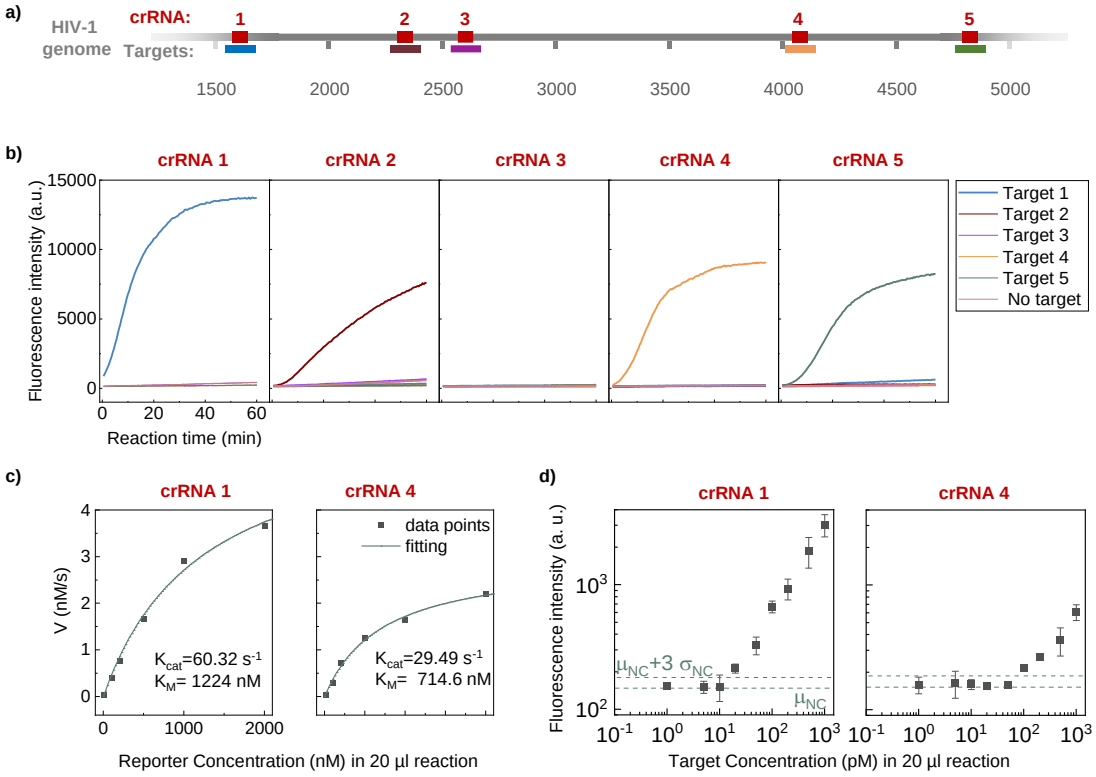

Figure 7-6. Optimization of Cas13 crRNA and bulk assay characterization. a) Schematic of the HIV-1 genome and the location of each crRNA spacer and the target region. b) Fluorescence intensity values over 60 minutes for 5 different crRNA and their corresponding targets (positive), no-target (NTC), and negative control (NC) samples. c) Michaelis-Menten kinetic study of the Cas13a assay using crRNA 1 and crRNA 4. d) Sensitivity test of CRISPR assay using crRNA 1 and crRNA 4. In each case, three NTC cases were tested to determine the background fluorescent intensity as µNTC+3σNTC, where µNTC and σNTC are the averages and standard deviation of the NTC cases, respectively.

Figure 7-7 shows the details of cleaved reporter concentration and measurements of cleavage speed. In order to extract the kinetic properties of Cas13 proteins using crRNA1 and 4, the curves in **Figure 7-6d** were fitted using nonlinear regression based on the Michaelis-Menten equation:

$$V = k_{cat}\, E_0 \frac{[S]}{K_M + [S]} \qquad (7.3)$$

where E_0 is the target-activated Cas/13−cRNA complex concentration, $[S]$ is the reporter concentration, k_{cat} is the catalytic turnover rate of the enzyme, and K_M is Michaelis constant. For the reaction using crRNA 1 and 4, the catalytic rate of 29.49 s^{-1} and 60.32 s^{-1} were measured,

respectively. The assay using crRNA1 displayed a reaction with a higher cleavage rate. Therefore, crRNA1 was chosen for our digital assay to obtain a faster signal. In addition, we also quantified the bulk assay limit of detection using crRNA 1 and 4. As shown in **Figure 7-6d**, HIV-1 Cas 13 assay using crRNA1 showed a better limit of detection of ~20 pM compared to ~100 pM when using crRNA4. The pM range of limit of detection in an amplification-free bulk Cas13 assay is on par with the previously reported Sherlock assay (~50 pM) [137].

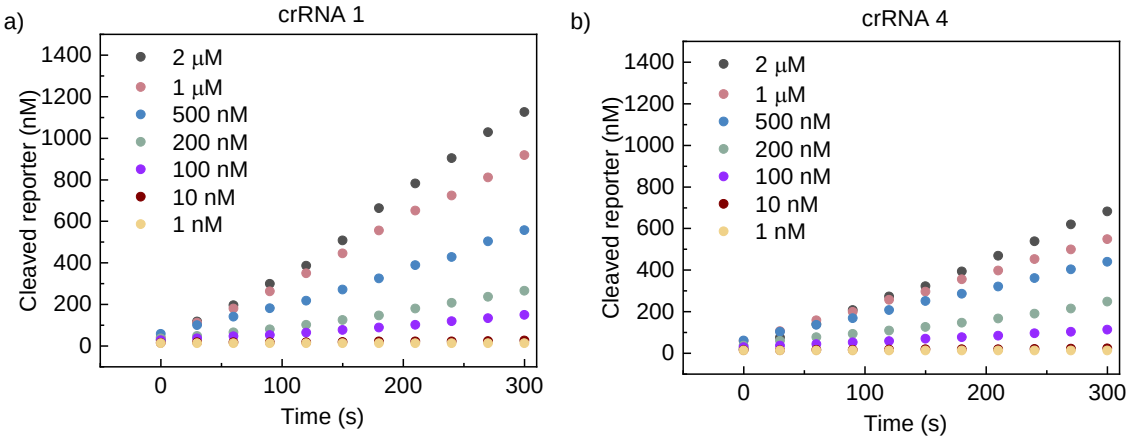

c)

Reporter concentration (nM)	Cleavage Velocity using crRNA 1 (nM/s)	Cleavage Velocity using crRNA 4 (nM/s)
2000	3.657189	2.208361
1000	2.917791	1.634262
500	1.664232	1.261519
200	0.762344	0.709897
100	0.410205	0.283772
10	0.035589	0.028096

Figure 7-7. Cleavage velocity measurements using crRNA1 and 4. Measurements of cleaved reporters associated with the trans-cleavage activity of the CRISPR Cas13 proteins using a) crRNA 1 and b) crRNA 4. In each case, cleaved reporters were measured for 420 s to extract the cleavage speed (*V* (nM/s)). c) Details of measured cleavage speed of CRISPR Cas13 proteins using crRNA 1 and crRNA 4 at different reporter concentrations.

7.3.4 Optimizing HIV-1 STAMP-dCRISPR assay time

To obtain the optimal reaction time for HIV-1 assay, we measured the *PPR* at different reaction times for the Cas13a assay containing 5 fM HIV-1 synthetic RNA. **Figure 7-8a** presents the fluorescence images at various reaction times. As the reaction time increased, more positive pores were observed in fluorescent images. This happened because more reporters would be degraded in the positive pores as the reaction time increases, resulting in more wells reaching fluorescent intensity above the sensor detection sensitivity. **Figure 7-8b** and **Figure 7-8c** show the corresponding fluorescent intensity (FI) of positive and negative pores and their distributions, respectively. These results confirmed our observation that more positive pores were detected as the reaction time increased. To quantify the effect of reaction time, *PPR* was plotted from 0 to 60 minutes of reaction (**Figure 7-8d** and **Table 7-3**). As expected, *the PPR* increases as time passes; however, the ratio becomes stable after 30 minutes. This means that the shortest time to develop a reliable *PPR* reading is about 30 minutes in our assay.

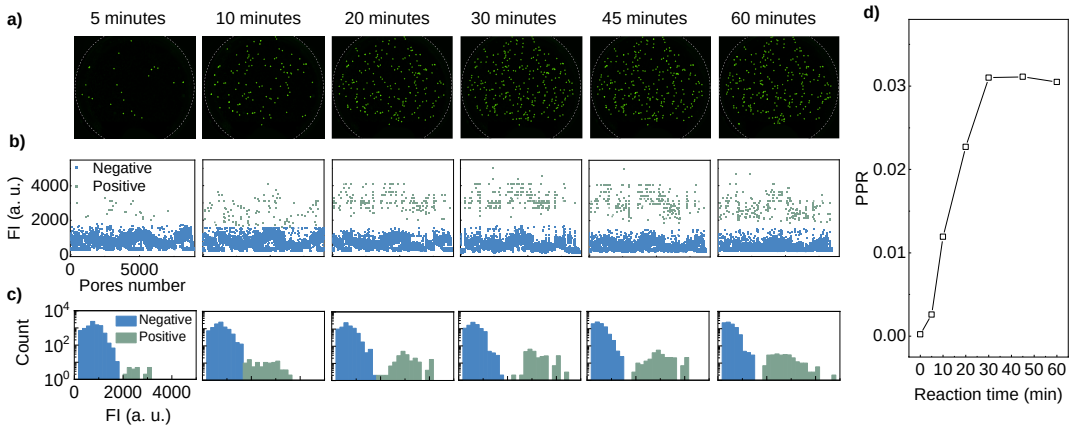

Figure 7-8 Optimizing STAMP-dCRISPR assay time. a) Fluorescent images illustrating the positive and negative pores at different reaction times from 0 to 60 minutes. The dashed grey circles illustrate the membrane edge. All positive pores are labeled with a filled green circle for better demonstration. b) Fluorescent intensity inside all filled pores (positive and negative) at different reaction times. Positive and negative pores are labeled as green and blue circles, respectively. c) Distribution of fluorescent intensity emitted from positive (green bars) and negative (blue bars)

pores. d) The ratio of positive pores (*PPR*) at different reaction times.

Based on the measured k_{cat} (**Figure 7-6c)**, a single activated Cas13a enzyme would produce ~13 nM of cleaved reporters (fluorescent probes) inside each pore (volume of 13 pL) in a 30 minute reaction. In contrast, a bulk reaction of 20 µL volume would only have produced ~ 9 pM with the same 30 min reaction. Decreasing the reaction volume from microliter to picolitre would increase the fluorescent concentration by around 6 orders of magnitude and thus help improve the lower limit of detection.

Table 7-3. Details information for the total number of filled pores, positive pores, and positive pore ratio at different reaction times.

Reaction time (min)	Total filled number of filled pores	Number of positive pores	Positive pore ratio (PPR)
0	2	9421	0.000212292
5	24	9235	0.002598809
10	110	9230	0.01191766
20	202	8901	0.022694079
30	275	8872	0.030996393
45	271	8710	0.031113662
60	257	8431	0.030482742

7.3.5 Analytical performance test with synthetic HIV-1 RNAs

A series of synthetic HIV-1 RNA dilutions from 10 aM to 5 pM were tested to examine the quantitative analytical performance of the STAMP-dCRISPR. **Figure 7-9a** presents the fluorescent images at different HIV-1 RNA concentrations. As expected, more positive pores were detected as

HIV-1 RNA concentration increased. The *PPR* at different target concentrations is plotted in **Figure 7-9b**. Expectedly, the measured *PPR* increased from 3.7×10^{-4} at 10 aM to 0.99 at 5 pM. These results revealed the dynamic range of STAMP-dCRISPR from 100 aM to 1 pM (4 orders of magnitude). For a concentration lower than 100 aM, the background noise of the system would interfere with the quantification, and accurate measurement could not be achieved. On the other hand, the *PPR* would saturate at 1 for cases with a concentration higher than 1 pM.

Figure 7-9c presents the measured concentrations via STAMP-dCRISPR versus the expected target concentration (**Table 7-4**). The measured concentrations in the dynamic range (100 aM to 1 pM) agree very well with the expected concentrations (R^2=0.998), confirming the absolute quantification capability of the STAMP-dCRIPSR. With the background noise defined as $\mu_{NTC}+3\sigma_{NTC}$, the LOD of the STAMP-dCRIPSR was determined to be around 100 aM. As compared to the LOD of 20 pM in the bulk assay shown in **Figure 7-6d,** the STAMP-dCRIPSR improved the LOD by 5 orders of magnitude.

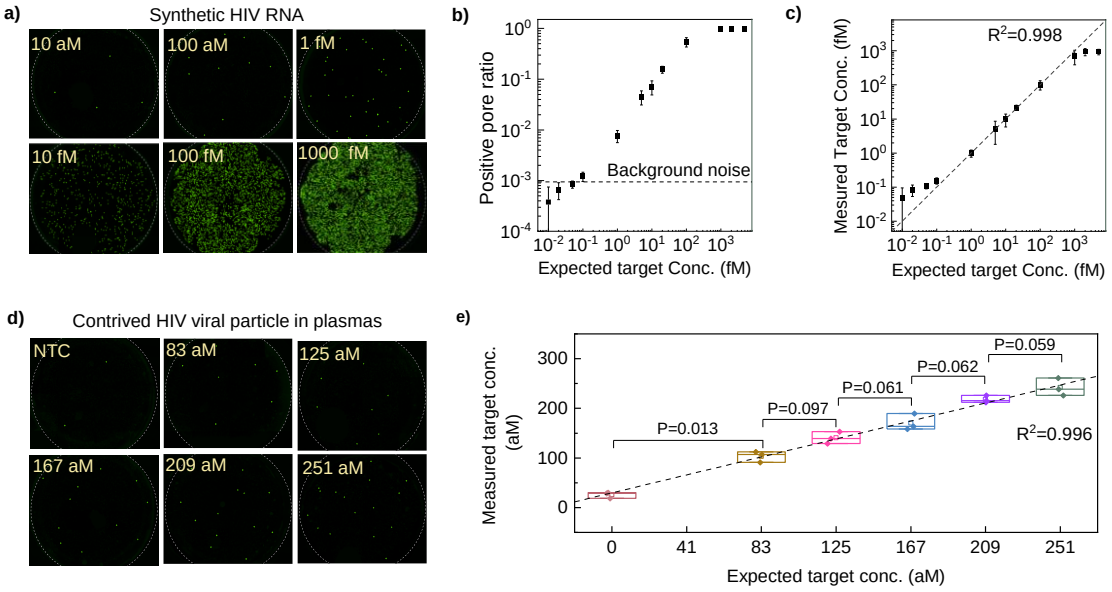

Figure 7-9. Optimizing STAMP-dCRISPR assay time. a) Fluorescent images illustrating the positive and negative pores at different reaction times from 0 to 60 minutes. The dashed grey circles

illustrate the membrane edge. All positive pores are labeled with a filled green circle for better demonstration. b) Fluorescent intensity inside all filled pores (positive and negative) at different reaction times. Positive and negative pores are labeled as green and blue circles, respectively. c) Distribution of fluorescent intensity emitted from positive (green bars) and negative (blue bars) pores. d) The ratio of positive pores (*PPR*) at different reaction times.

Table 7-4. Details information for the total number of filled pores, positive pores, positive pore ratio, the expected number of targets in each pore (λ), and measured concentrations at different expected target concentrations.

Expected Target Concentration (fM)	Total number of filled pores	Number of positive pores	Positive pore ratio	Measured Concentration (fM)
First batch				
0.01	8625	4	0.000463768	0.06
0.02	7835	4	0.00051053	0.07
0.05	7545	7	0.000927767	0.12
0.1	9231	10	0.001083306	0.14
1	8729	57	0.006529958	0.86
5	7342	280	0.038136747	2.99
10	6686	400	0.059826503	7.88
20	5451	912	0.167308751	23.32
100	6925	4136	0.597256318	116.17
1000	8765	8722	0.995094124	797.74
2000	6950	6941	0.998705036	849.34
5000	8574	8571	0.999650105	1016.34
Second batch				
0.01	9053	5	0.000552303	0.07
0.02	7432	6	0.00080732	0.10
0.05	8312	7	0.000842156	0.11
0.1	8653	12	0.001386802	0.18
1	8981	81	0.00901904	1.15
5	9232	503	0.054484402	7.13
10	9367	766	0.081776449	11.96

20	8869	1271	0.143308152	19.75
100	8882	4150	0.467237109	80.43
1000	9080	9069	0.998788546	857.85
2000	9456	9453	0.999682741	1029.17
5000	8938	8931	0.999216827	956.21
		Third batch		
0.01	8322	1	0.000120163	0.016
0.02	7325	5	0.000682594	0.09
0.05	7880	6	0.000761421	0.10
0.1	9321	11	0.001180131	0.15
1	10755	80	0.007438401	0.95
5	9242	390	0.042198658	5.53
10	7329	623	0.085004776	11.34
20	6408	826	0.128901373	17.62
100	8713	5007	0.574658556	109.32
1000	8425	8235	0.977448071	484.36
2000	8133	8125	0.999016353	921.21
5000	7123	7111	0.998315317	815.12

7.3.6 Resolution test with contrived plasma sample

To examine the resolution of viral load from the plasm samples, we prepared a serial of mock plasma samples with HIV-1 viral particles spiked into the healthy plasma. Each concentration was prepared in triplicates. The viral RNAs were extracted from these mock plasma samples using a column-based extraction process before being quantified using STAMP-dCRISPR. **Figure 7-9d** presents six representative fluorescent images. It is evident that more positive pores were observed as we increased the viral concentration. **Figure 7-9e** shows the measured concentration obtained by STAMP-dCRISPR versus the expected values (see **Table 7-5** for testing statistics). The

measured concentrations agree very well with the input concentrations (R^2=0.996), confirming the capability of STAMP-dCRISPR system for the absolute quantification of plasma samples. In addition, the *p*-value obtained from the t-test between adjacent concentrations revealed that the STAMP-dCRISPR could differentiate the spiked samples with a resolution of 42 aM with >90% confidence. This resolution is equivalent to resolving 5 copies of HIV-1 RNAs in the STAMP device.

Table 7-5. Details information for the total number of filled pores, positive pores, positive pore ratio, and measured concentrations at different input target copies inside the 140 μL of plasma

Input targets (Copies)	Total number of filled pores	Number of positive pores	Positive pore ratio	Measured targets (Copies)
First batch				
0	8845	2	0.000226116	347
1000	8423	6	0.000712335	1096
1500	7510	9	0.001198402	1844
2000	8585	11	0.001281305	1972
2500	8428	14	0.00166113	2557
3000	9041	16	0.001769716	2725
Second batch				
0	6752	1	0.000148104	227
1000	9115	8	0.000877674	1350
1500	8252	9	0.001090645	1678
2000	8765	13	0.001483172	2285
2500	7921	14	0.001767454	2721
3000	8321	17	0.002043024	3146
Third batch				
0	8501	2	0.000235266	361
1000	8346	7	0.000838725	1290
1500	8895	9	0.001011804	1557

2000	8871	11	0.001239995	1908
2500	6521	11	0.001686858	2597

7.3.7 Clinical validation of STAMP-dCRISPR

To demonstrate the clinical utility of the STAMP-dCRISPR, we tested 20 clinical HIV plasma samples using STAMP-dCRISPR. Like the mock samples, we extracted the HIV viral RNA using a column-based extraction process. The extracted RNA was aliquoted into two identical duplicates and tested with STAMP-dCRISPR and RT-PCR, respectively. **Figure 7-10a** shows the fluorescent images of STAMP-dCRISPR results. **Figure 7-10b** presents the real time RT-PCR results with six concentration references (R1-R6). The C_t values showed a linear logarithmic relationship with the reference concentrations, which validates the RT-PCR assay (**Figure 7-11**).

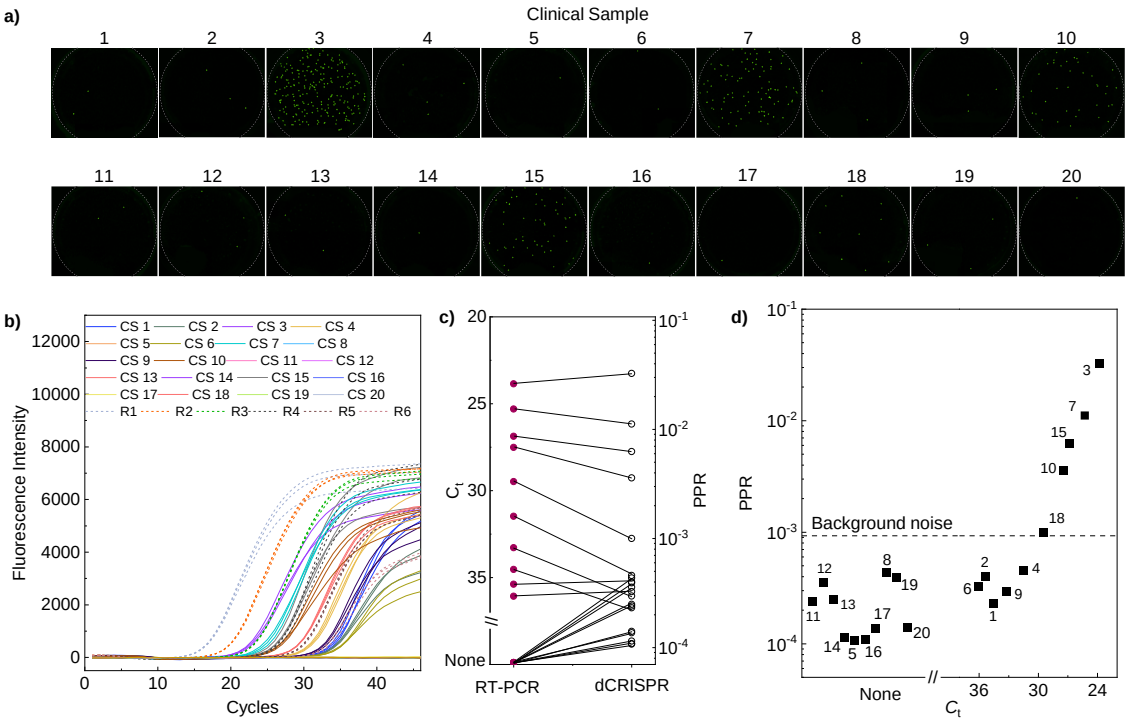

Figure 7-10. Clinical samples test using STAMP-dCRISPR. a) Fluorescent images illustrating positive and negative pores for different clinical samples. All positive pores are labeled with a filled green circle for better demonstration. b) Fluorescent intensity of 20 clinical samples and 6 analytical

samples during 46 cycles of RT-PCR amplification. c) Correspondence between the C_t values obtained from RT-PCR and PPR values from STAMP-dCRISPR. d) C_t values versus PPR values for all 20 clinical samples. C_t values for non-amplified cases were set as None in the figure.

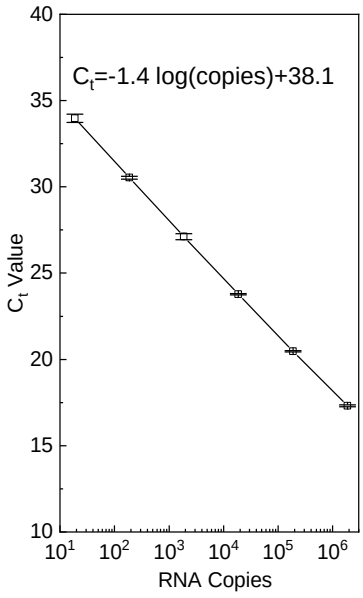

Figure 7-11. The C_t values obtained from the RT-PCR versus the target RNA copies. C_t values showed a logarithmic relationship with the sample concentration and verified our assay.

Table 7-6. Details information for the total number of filled pores, positive pores, positive pore ratio, the expected number of targets in each pore (λ), and measured concentrations of clinical samples.

Sample #	Total number of filled pores	Number of positive pores	Positive pore ratio	λ
1	8651	2	0.000231187	0.000231214
2	7515	3	0.000399202	0.000399281
3	7234	235	0.032485485	0.032912355
4	8723	4	0.000458558	0.000458663
5	9316	1	0.000107342	0.000107348
6	6153	2	0.000325045	0.000325098
7	8424	94	0.011158594	0.012552231
8	6928	3	0.000433025	0.000433119

9	10127	3	0.000296238	0.000296282
10	10870	39	0.003587856	0.003594308
11	8324	2	0.000240269	0.000240298
12	8412	3	0.000356633	0.000356697
13	8021	2	0.000249345	0.000249377
14	8740	1	0.000114416	0.000114423
15	8801	55	0.00624929	0.006268898
16	9201	1	0.000108684	0.00010869
17	7338	1	0.000136277	0.000136286
18	9021	9	0.000997672	0.000998172
19	7668	3	0.000391236	0.000391313
20	7123	1	0.00014039	0.0001404

Table 7-7. Details information for the RT-PCR Ct values of clinical samples.

Sample #	Total number of filled pores	Ct Value (mean)	Ct Value (STD)
1	8651	34.53	0.22
2	7515	35.39	0.14
3	7234	23.86	0.09
4	8723	31.48	0.23
5	9316	None	None
6	6153	36.08	0.05
7	8424	25.3	0.2
8	6928	None	None
9	10127	33.28	0.18
10	10870	27.51	0.16
11	8324	None	None

12	8412	None	None
13	8021	None	None
14	8740	None	None
15	8801	26.87	0.11
16	9201	None	None
17	7338	None	None
18	9021	29.48	0.11
19	7668	None	None
20	7123	None	None

To benchmark the STAMP-dCRISPR results with the RT-PCR, C_t values of RT-PCR results were compared with the PPR values measured by STAMP-dCRISPR (**Figure 7-10c** and **Figure 7-10d, Table 7-6, Table 7-7)**. The *PPR* corresponded well with C_t values for RT-PCR positive cases and showed the potential of STAMP-dCRISPR for clinical HIV detection. In addition, The *PPR* was less than background noise in all 10 RT-PCR negative cases (no C_t values), and no false positive results were observed using STAMP-dCRISPR.

7.4 Summary

In summary, we reported a self-digitalization through automated membrane-based partitioning (STAMP) technique to digitalize the CRISPR-Cas13 assay (dCRISPR) for amplification-free and absolute quantification of HIV-1 viral RNAs. We first characterize the STAMP device to digitalize the Cas13a assay inside a commercial PCTE membrane reliably. Afterward, we developed an automated platform to utilize the STAMP device for HIV-1 viral load quantification. The effect of five different crRNAs on the Cas13a trans-cleavage speed was studied, and crRNA 1, which showed the fastest cleavage speed, was chosen for the digital assay. Investigating the effect of assay

reaction time on the sensing performance revealed that 30 minutes reaction is enough for our system to differentiate between positive and negative pores in the membrane. We evaluated the analytical performances of STAMP-dCRISPR with synthetic HIV-1 RNAs. The results showed that the samples spanning 4 orders of dynamic range between 100 aM to 1 pM could be quantified using our system. In addition, we identified the resolution of STAMP-dCRISPR as 42 aM at a 90% confidence level by testing the contrived plasma samples. Finally, we evaluated 20 clinical plasma samples with STAMP-dCRISPR, and the results agreed well with the RT-qPCR. We believe STAMP-dCRISPR offers an amplification-free quantification platform for not only HIV-1 but also other infectious diseases.

CHAPTER 8 CONCLUSION AND PERSPECTIVES

8.1. Conclusions

This dissertation explores the digital quantification of target nucleic acids using solid-state nanopores and CRISPR towards rapid, label-free nucleic acid testing. Three major parts have been explored in the realm of this thesis.

While the solid-state nanopore sensors have shown exceptional promise with their single molecule sensitivity and label-free operations, one of the most significant challenges in the nanopore sensor is the limited analyte translocation event rate that leads to prolonged sensor response time. This issue is more pronounced when the analyte concentration is below the nano-molar (nM) range, owing to the diffusion-limited mass transport. In our work, we systematically studied the experimental factors beyond the intrinsic analyte concentration and electrophoretic mobility that affect the event rate in glass nanopore sensors. The synergistic effects of these factors on the event rates were investigated with the aim of finding the optimized experimental conditions for operating the glass nanopore sensor from the response time standpoint. These findings would provide insight for future glass nanopore sensing experiments towards ultrasensitive sensing applications where the device response time is significant. In nanopore sensing, a detailed nanopore geometry and size characterization or a calibration curve of concentration standards are often required for quantifying the unknown sample. We proposed and validated a calibration-free nanopore single molecule digital counting method for isolated molecule quantification. We recognized the ionic rates (baseline current) in a particular experiment could be used as an effective *in-situ* reference. We developed a quantitative model for calibration-free quantification of molecule concentration, which was experimentally validated for different nanopores and DNA molecules.

While solid-state nanopore sensor represents a promising platform for nucleic acid detection due to its unique single molecule sensitivity, differentiating between different pathogens using solid-state nanopores is highly challenging. Therefore, we combined the high specificity offered by the CRISPR Cas proteins and the high sensitivity offered by the glass nanopore sensor (SCAN) towards nucleic acid detection. We first utilized the SCAN for HIV-1 detection. We found that concentrations less than 10 nM would likely require pre-amplification steps to detect target pathogens in less than 1 hour. Therefore, in our next work, we combined SCAN with a pre-amplification step for specific detection of SARS-CoV-2. With a preamplification and 30 min of CRISPR Cas12a assay, we achieved excellent specificity against other common human coronaviruses and a limit of detection of 13.5 copies/µl (22.5 aM) of viral RNA at the 95% confidence level.

While CRISPR-based nucleic acid-sensing systems have grown rapidly in the past few years, most of these systems need a pre-amplification step which was observed in our study. We developed a quantitative CRISPR sensing figure of merit (FOM) to explore performance improvement strategies and find an alternative for the preamplification step. Based on our model which was benchmarked by 57 existing studies, digitalization was the most promising amplification-free method for achieving comparable FOM performances (~1 fM·min) as those using preamplification. Therefore, in our final work, we proposed and evaluated a simple and easy-to-use digital CRISPR platform for pathogen detection and quantification. We validated this system by quantifying HIV-1 viral RNAs. The analytical performances of STAMP-dCRISPR were evaluated with synthetic HIV-1 RNA, and it was found samples spanning 4 orders of dynamic range between 100 aM to 1 pM can be quantified as fast as 30 min. We also evaluated 20 clinical plasma samples with STAMP-dCRISPR, and the results agreed well with the RT-qPCR.

In summary, the significant contributions of this thesis are as follows:

(1) We explored the molecular transport dynamics through the nanopore and the experiment-relevant parameters and their effects on the event, which would help us to design an experimental setup with higher throughput and accuracy.

(2) We proposed and validated a calibration-free model for concentration estimation to address the pore-to-pore variations issues of nanopores.

(3) We introduced a solid-State CRISPR-assisted nanopore diagnostic system for specific and sensitive detection of pathogens and evaluated the system performance by detecting HIV-1 and SARS- CoV-2.

(4) We developed an inexpensive and simple digital CRISPR-based platform for nucleic acid quantification without the need for a preamplification step.

8.2. Future prospective

The research work presented in the thesis has shown very promising results. However, several important aspects should be addressed in future research.

(1) In our study on the impact of experiment-relevant parameters on the molecular transport dynamics through the nanopore, we showed that due to the negative surface charge in glass nanopores, translocation from the glass nanopore could be orders of magnitude faster than that into the nanopore at low salt concentrations and higher surface charges. Nevertheless, due to the complication of filling and draining the glass nanopores, we perform our experiment by translocating the samples into the nanopores. In future works, the analyte could be inserted inside the nanopore to increase the translocation rate and improve the sensing response time.

(2) The free nanopore single molecule digital counting method was evaluated using glass nanopore and DNA molecules. On the other hand, the principle could be well extended to other nanopore

types and other charged molecules. To evaluate this technique for other cases, it is necessary to test different types of nanopores, such as silicon nitride or biological nanopores, and different charged molecules, such as proteins.

(3) In the SCAN development, we realized that the HIV-1 Cas12a reaction should be performed at 100 mM salt concentration. However, a high salt concentration would be favorable for nanopore sensing as the low salt concentration will dramatically reduce the event rate and the signal in glass nanopores. We used a two-step protocol in our SCAN system to solve the conflicting buffer requirements in the Cas12a reaction (low salt) and the nanopore sensing (high salt). In future works, utilizing different techniques introduced in chapter 2, such as translocation direction and nanopore geometry to enhance the translocation rate, could help us achieve a one-step protocol for the SCAN system at low salt concentration.

(4) In the SCAN system for SARS-COV-2 diagnostic, we utilized a PCR amplification step before the CRISPR assay to enhance the sensitivity. While PCR needs thermocycling from 60 ºC to 95 ºC, CRISPR assay should be performed at 37 ºC. Therefore, we performed the assay in two steps. Operating the assay in two-step complicates the testing process, increases the liquid handling, and potentially increases the risk of contaminations due to amplification products transferring. Utilizing isothermal amplification techniques such as RPA has the potential to solve this issue. However, adding all the components (amplification and CRISPR reagents) in one pot would decrease the efficiency due to the possible cross-reactions and digestion of the initial amplification products by the Cas/crRNA complex [181]. Therefore, developing a one-step assay with the optimized concentration of reagents could provide substantial opportunities for CRISPR-based point-of-care testing.

(5) In our study on CRISPR diagnostic performance improvement strategies, we realized different Cas proteins and crRNA sequences could affect the system performance. In developing SCAN for HIV-1 and SARS-COV-2 testing, we didn't explore the effects of different crRNA designs

on the system performance. Exploring new crRNA designs and different Cas proteins could improve the sensing efficiency considerably.

(6) While STAMP-dCRISPR showed excellent specificity in clinical sample testing, we could pick up some of the RT-PCR samples with our system. This is mainly due to the subsampling error, which arises in all biological assays (digital or analog), which does not analyze the full volume of the sample [311]. While the CRISPR mixture volume is 20 μL, the STAMP device takes ~ 100 nL for each analysis. Subsampling error could affect the lower detection limit at low concentrations and is independent of the instrumentation and signal acquisition. Several methods could alleviate this challenge in the future. Using multiple membranes for a single sample could increase the volume of testing samples and substantially improve the system's performance. Also, magnetic-bead based preconcentration [302] could be utilized to enrich target RNA molecules inside the membrane.

Bibliography

[1] C. Wang, M. Liu, Z. Wang, S. Li, Y. Deng, and N. He, "Point-of-care diagnostics for infectious diseases: From methods to devices," *Nano Today*, vol. 37, p. 101092, 2021.

[2] D. M. Morens, G. K. Folkers, and A. S. Fauci, "The challenge of emerging and re-emerging infectious diseases," *Nature*, vol. 430, no. 6996, pp. 242-249, 2004.

[3] H. Harapan *et al.*, "Coronavirus disease 2019 (COVID-19): A literature review," *Journal of infection and public health*, vol. 13, no. 5, pp. 667-673, 2020.

[4] S. G. Deeks, J. Overbaugh, A. Phillips, and S. Buchbinder, "HIV infection," *Nature reviews Disease primers*, vol. 1, no. 1, pp. 1-22, 2015.

[5] P. Sands, C. Mundaca-Shah, and V. J. Dzau, "The neglected dimension of global security—a framework for countering infectious-disease crises," *New England Journal of Medicine*, vol. 374, no. 13, pp. 1281-1287, 2016.

[6] A. M. Caliendo *et al.*, "Better tests, better care: improved diagnostics for infectious diseases," *Clinical Infectious Diseases*, vol. 57, no. suppl_3, pp. S139-S170, 2013.

[7] C. D. Kelly-Cirino *et al.*, "Importance of diagnostics in epidemic and pandemic preparedness," *BMJ global health*, vol. 4, no. Suppl 2, p. e001179, 2019.

[8] R. M. Lequin, "Enzyme immunoassay (EIA)/enzyme-linked immunosorbent assay (ELISA)," *Clinical chemistry*, vol. 51, no. 12, pp. 2415-2418, 2005.

[9] A. Hematian *et al.*, "Traditional and modern cell culture in virus diagnosis," *Osong public health and research perspectives*, vol. 7, no. 2, pp. 77-82, 2016.

[10] G. A. Posthuma-Trumpie, J. Korf, and A. van Amerongen, "Lateral flow (immuno) assay: its strengths, weaknesses, opportunities and threats. A literature survey," *Analytical and bioanalytical chemistry*, vol. 393, no. 2, pp. 569-582, 2009.

[11] I. M. Mackay, K. E. Arden, and A. Nitsche, "Real-time PCR in virology," *Nucleic acids research*, vol. 30, no. 6, pp. 1292-1305, 2002.

[12] S. Hosseini, P. Vázquez-Villegas, M. Rito-Palomares, and S. O. Martinez-Chapa, "Advantages, disadvantages and modifications of conventional ELISA," in *Enzyme-Linked Immunosorbent Assay (ELISA)*: Springer, 2018, pp. 67-115.

[13] A. Niemz, T. M. Ferguson, and D. S. Boyle, "Point-of-care nucleic acid testing for infectious diseases," *Trends in biotechnology*, vol. 29, no. 5, pp. 240-250, 2011.

[14] X. Lin, X. Huang, K. Urmann, X. Xie, and M. R. Hoffmann, "Digital loop-mediated isothermal amplification on a commercial membrane," *ACS sensors*, vol. 4, no. 1, pp. 242-249, 2019.

[15] K. A. Heyries *et al.*, "Megapixel digital PCR," *Nature methods*, vol. 8, no. 8, pp. 649-651, 2011.

[16] M. Baker, "Digital PCR hits its stride," *nature methods*, vol. 9, no. 6, pp. 541-544, 2012.

[17] X. Huang *et al.*, "Smartphone-based in-gel loop-mediated isothermal amplification (gLAMP) system enables rapid coliphage MS2 quantification in environmental waters," *Environmental science & technology*, vol. 52, no. 11, pp. 6399-6407, 2018.

[18] X. Lin *et al.*, "A microfluidic chip capable of switching W/O droplets to vertical laminar flow for electrochemical detection of droplet contents," *Analytica chimica acta*, vol. 828, pp. 70-79, 2014.

[19] R. Novak *et al.*, "Single‐cell multiplex gene detection and sequencing with microfluidically generated agarose emulsions," *Angewandte Chemie International Edition*, vol. 50, no. 2, pp. 390-395, 2011.

[20] Y.-D. Ma, K. Luo, W.-H. Chang, and G.-B. Lee, "A microfluidic chip capable of generating and trapping emulsion droplets for digital loop-mediated isothermal amplification analysis," *Lab on a Chip,* vol. 18, no. 2, pp. 296-303, 2018.

[21] F. Schuler *et al.*, "Digital droplet PCR on disk," *Lab on a Chip,* vol. 16, no. 1, pp. 208-216, 2016.

[22] E.-C. Yeh, C.-C. Fu, L. Hu, R. Thakur, J. Feng, and L. P. Lee, "Self-powered integrated microfluidic point-of-care low-cost enabling (SIMPLE) chip," *Science advances,* vol. 3, no. 3, p. e1501645, 2017.

[23] Q. Zhu *et al.*, "A scalable self-priming fractal branching microchannel net chip for digital PCR," *Lab on a Chip,* vol. 17, no. 9, pp. 1655-1665, 2017.

[24] Y. Men, Y. Fu, Z. Chen, P. A. Sims, W. J. Greenleaf, and Y. Huang, "Digital polymerase chain reaction in an array of femtoliter polydimethylsiloxane microreactors," *Analytical chemistry,* vol. 84, no. 10, pp. 4262-4266, 2012.

[25] B. Sun, F. Shen, S. E. McCalla, J. E. Kreutz, M. A. Karymov, and R. F. Ismagilov, "Mechanistic evaluation of the pros and cons of digital RT-LAMP for HIV-1 viral load quantification on a microfluidic device and improved efficiency via a two-step digital protocol," *Analytical chemistry,* vol. 85, no. 3, pp. 1540-1546, 2013.

[26] L. Bao, A. R. Rezk, L. Y. Yeo, and X. Zhang, "Highly ordered arrays of femtoliter surface droplets," *small,* vol. 11, no. 37, pp. 4850-4855, 2015.

[27] T. M. Yen *et al.*, "Self-Assembled Pico-Liter Droplet Microarray for Ultrasensitive Nucleic Acid Quantification," *ACS nano,* vol. 9, no. 11, pp. 10655-10663, 2015.

[28] A. Gansen, A. M. Herrick, I. K. Dimov, L. P. Lee, and D. T. Chiu, "Digital LAMP in a sample self-digitization (SD) chip," *Lab on a Chip,* vol. 12, no. 12, pp. 2247-2254, 2012.

[29] M. Firnkes, D. Pedone, J. Knezevic, M. Doblinger, and U. Rant, "Electrically facilitated translocations of proteins through silicon nitride nanopores: conjoint and competitive action of diffusion, electrophoresis, and electroosmosis," *Nano letters,* vol. 10, no. 6, pp. 2162-2167, 2010.

[30] J. Li, M. Gershow, D. Stein, E. Brandin, and J. A. Golovchenko, "DNA molecules and configurations in a solid-state nanopore microscope," *Nature materials,* vol. 2, no. 9, pp. 611-615, 2003.

[31] R. Smeets, S. W. Kowalczyk, A. Hall, N. Dekker, and C. Dekker, "Translocation of RecA-coated double-stranded DNA through solid-state nanopores," *Nano letters,* vol. 9, no. 9, pp. 3089-3095, 2008.

[32] L. J. Steinbock, R. D. Bulushev, S. Krishnan, C. Raillon, and A. Radenovic, "DNA translocation through low-noise glass nanopores," *Acs Nano,* vol. 7, no. 12, pp. 11255-11262, 2013.

[33] W.-J. Lan, D. A. Holden, B. Zhang, and H. S. White, "Nanoparticle transport in conical-shaped nanopores," *Analytical chemistry,* vol. 83, no. 10, pp. 3840-3847, 2011.

[34] N. A. Bell, M. Muthukumar, and U. F. Keyser, "Translocation frequency of double-stranded DNA through a solid-state nanopore," *Physical Review E,* vol. 93, no. 2, p. 022401, 2016.

[35] S. Garaj, W. Hubbard, A. Reina, J. Kong, D. Branton, and J. A. Golovchenko, "Graphene as a subnanometre trans-electrode membrane," (in English), *Nature,* vol. 467, no. 7312, pp. 190-193, Sep 9 2010.

[36] B. N. Miles, A. P. Ivanov, K. A. Wilson, F. Dogan, D. Japrung, and J. B. Edel, "Single molecule sensing with solid-state nanopores: novel materials, methods, and applications," (in English), *Chemical Society Reviews,* vol. 42, no. 1, pp. 15-28, 2013.

[37] C. B. Rosen, D. Rodriguez-Larrea, and H. Bayley, "Single-molecule site-specific detection of protein phosphorylation with a nanopore," *Nature biotechnology,* vol. 32, no. 2, pp. 179-181, 2014.

[38] D. Japrung *et al.*, "Single-molecule studies of intrinsically disordered proteins using solid-state nanopores," *Analytical chemistry,* vol. 85, no. 4, pp. 2449-2456, 2013.

[39] C. Shasha, R. Y. Henley, D. H. Stoloff, K. D. Rynearson, T. Hermann, and M. Wanunu, "Nanopore-based conformational analysis of a viral RNA drug target," *ACS nano,* vol. 8, no. 6, pp. 6425-6430, 2014.

[40] M. Zhang, L.-H. Yeh, S. Qian, J.-P. Hsu, and S. W. Joo, "DNA Electrokinetic translocation through a nanopore: local permittivity environment effect," *The Journal of Physical Chemistry C,* vol. 116, no. 7, pp. 4793-4801, 2012.

[41] T. Albrecht, "Single-molecule analysis with solid-state nanopores," *Annual Review of Analytical Chemistry,* vol. 12, pp. 371-387, 2019.

[42] M. Wanunu, W. Morrison, Y. Rabin, A. Y. Grosberg, and A. Meller, "Electrostatic focusing of unlabelled DNA into nanoscale pores using a salt gradient," *Nature nanotechnology,* vol. 5, no. 2, pp. 160-165, 2010.

[43] R. Nouri, Z. Tang, and W. Guan, "Calibration-Free Nanopore Digital Counting of Single Molecules," *Analytical chemistry,* vol. 91, no. 17, pp. 11178-11184, 2019.

[44] Y. Wu, R. D. Tilley, and J. J. Gooding, "Challenges and Solutions in Developing Ultrasensitive Biosensors," *Journal of the American Chemical Society,* vol. 141, no. 3, pp. 1162-1170, 2018.

[45] T. M. Squires, R. J. Messinger, and S. R. Manalis, "Making it stick: convection, reaction and diffusion in surface-based biosensors," *Nature biotechnology,* vol. 26, no. 4, pp. 417-426, 2008.

[46] K. J. Freedman, L. M. Otto, A. P. Ivanov, A. Barik, S.-H. Oh, and J. B. Edel, "Nanopore sensing at ultra-low concentrations using single-molecule dielectrophoretic trapping," *Nature communications,* vol. 7, no. 1, p. 10217, 2016.

[47] J. J. Gooding and K. Gaus, "Single‐Molecule Sensors: Challenges and Opportunities for Quantitative Analysis," *Angewandte Chemie International Edition,* vol. 55, no. 38, pp. 11354-11366, 2016.

[48] S. O. Kelley, C. A. Mirkin, D. R. Walt, R. F. Ismagilov, M. Toner, and E. H. Sargent, "Advancing the speed, sensitivity and accuracy of biomolecular detection using multi-length-scale engineering," *Nature nanotechnology,* vol. 9, no. 12, pp. 969-980, 2014.

[49] M. M. Hatlo, D. Panja, and R. van Roij, "Translocation of DNA molecules through nanopores with salt gradients: the role of osmotic flow," *Physical review letters,* vol. 107, no. 6, p. 068101, 2011.

[50] A. Y. Grosberg and Y. Rabin, "DNA capture into a nanopore: interplay of diffusion and electrohydrodynamics," *The Journal of chemical physics,* vol. 133, no. 16, p. 165102, 2010.

[51] K. Chen, N. A. Bell, J. Kong, Y. Tian, and U. F. Keyser, "Direction-and salt-dependent ionic current signatures for DNA sensing with asymmetric nanopores," *Biophysical journal,* vol. 112, no. 4, pp. 674-682, 2017.

[52] Y. He, M. Tsutsui, C. Fan, M. Taniguchi, and T. Kawai, "Controlling DNA translocation through gate modulation of nanopore wall surface charges," *ACS nano,* vol. 5, no. 7, pp. 5509-5518, 2011.

[53] C. R. Crick *et al.*, "Precise attoliter temperature control of nanopore sensors using a nanoplasmonic bullseye," *Nano letters,* vol. 15, no. 1, pp. 553-559, 2014.

[54] F. Nicoli, D. Verschueren, M. Klein, C. Dekker, and M. P. Jonsson, "DNA translocations through solid-state plasmonic nanopores," *Nano letters,* vol. 14, no. 12, pp. 6917-6925, 2014.

[55] A. P. Ivanov, P. Actis, P. Jönsson, D. Klenerman, Y. Korchev, and J. B. Edel, "On-demand delivery of single DNA molecules using nanopipets," *ACS nano,* vol. 9, no. 4, pp. 3587-3595, 2015.

[56] N. C. Stellwagen, C. Gelfi, and P. G. Righetti, "The free solution mobility of DNA," *Biopolymers: Original Research on Biomolecules,* vol. 42, no. 6, pp. 687-703, 1997.

[57] B. J. Kirby and E. F. Hasselbrink Jr, "Zeta potential of microfluidic substrates: 1. Theory, experimental techniques, and effects on separations," *Electrophoresis,* vol. 25, no. 2, pp. 187-202, 2004.

[58] D.-H. Lin, C.-Y. Lin, S. Tseng, and J.-P. Hsu, "Influence of electroosmotic flow on the ionic current rectification in a pH-regulated, conical nanopore," *Nanoscale,* vol. 7, no. 33, pp. 14023-14031, 2015.

[59] W. Yang *et al.*, "Detection of CRISPR-dCas9 on DNA with Solid-State Nanopores," (in English), *Nano Letters,* vol. 18, no. 10, pp. 6469-6474, Oct 2018.

[60] D. Zhou *et al.*, "Establishment and application of a loop-mediated isothermal amplification (LAMP) system for detection of cry1Ac transgenic sugarcane," *Scientific Reports,* Article vol. 4, p. 4912, 05/09/online 2014.

[61] W. Timp, U. M. Mirsaidov, D. Wang, J. Comer, A. Aksimentiev, and G. Timp, "Nanopore sequencing: electrical measurements of the code of life," *IEEE transactions on nanotechnology,* vol. 9, no. 3, pp. 281-294, 2010.

[62] W.-J. Lan, D. A. Holden, J. Liu, and H. S. White, "Pressure-driven nanoparticle transport across glass membranes containing a conical-shaped nanopore," *The Journal of Physical Chemistry C,* vol. 115, no. 38, pp. 18445-18452, 2011.

[63] S. Tseng, S.-C. Lin, C.-Y. Lin, and J.-P. Hsu, "Influences of cone angle and surface charge density on the ion current rectification behavior of a conical nanopore," *The Journal of Physical Chemistry C,* vol. 120, no. 44, pp. 25620-25627, 2016.

[64] K. A. Roshan, Z. Tang, and W. Guan, "High fidelity moving Z-score based controlled breakdown fabrication of solid-state nanopore," *Nanotechnology,* vol. 30, no. 9, p. 095502, 2019.

[65] W. Guan, R. Fan, and M. A. Reed, "Field-effect reconfigurable nanofluidic ionic diodes," *Nat Commun,* vol. 2, p. 506, Oct 18 2011.

[66] H. S. White and A. Bund, "Ion current rectification at nanopores in glass membranes," (in English), *Langmuir,* vol. 24, no. 5, pp. 2212-2218, Mar 4 2008.

[67] N. Laohakunakorn and U. F. Keyser, "Electroosmotic flow rectification in conical nanopores," *Nanotechnology,* vol. 26, no. 27, p. 275202, 2015.

[68] Y. Qiu, I. Vlassiouk, Y. Chen, and Z. S. Siwy, "Direction dependence of resistive-pulse amplitude in conically shaped mesopores," *Analytical chemistry,* vol. 88, no. 9, pp. 4917-4925, 2016.

[69] M. Cretich, G. G. Daaboul, L. Sola, M. S. Ünlü, and M. Chiari, "Digital detection of biomarkers assisted by nanoparticles: application to diagnostics," *Trends in biotechnology,* vol. 33, no. 6, pp. 343-351, 2015.

[70] F. Calderón-Celis *et al.*, "Enhanced universal quantification of biomolecules using element MS and generic standards: application to intact protein and phosphoprotein determination," *Analytical chemistry,* vol. 91, no. 1, pp. 1105-1112, 2018.

[71] W. Haiss, N. T. Thanh, J. Aveyard, and D. G. Fernig, "Determination of size and concentration of gold nanoparticles from UV− Vis spectra," *Analytical chemistry,* vol. 79, no. 11, pp. 4215-4221, 2007.

[72] F. H. Niesen, H. Berglund, and M. Vedadi, "The use of differential scanning fluorimetry to detect ligand interactions that promote protein stability," *Nature protocols,* vol. 2, no. 9, p. 2212, 2007.

[73] A. S. Basu, "Digital assays part I: partitioning statistics and digital PCR," *SLAS TECHNOLOGY: Translating Life Sciences Innovation,* vol. 22, no. 4, pp. 369-386, 2017.

[74] B. Vogelstein and K. W. Kinzler, "Digital pcr," *Proceedings of the National Academy of Sciences,* vol. 96, no. 16, pp. 9236-9241, 1999.

[75] C. M. Hindson *et al.*, "Absolute quantification by droplet digital PCR versus analog real-time PCR," *Nature methods,* vol. 10, no. 10, p. 1003, 2013.

[76] B. J. Hindson *et al.*, "High-throughput droplet digital PCR system for absolute quantitation of DNA copy number," *Analytical chemistry,* vol. 83, no. 22, pp. 8604-8610, 2011.

[77] D. M. Rissin *et al.*, "Single-molecule enzyme-linked immunosorbent assay detects serum proteins at subfemtomolar concentrations," *Nature biotechnology,* vol. 28, no. 6, p. 595, 2010.

[78] K. Leirs *et al.*, "Bioassay development for ultrasensitive detection of influenza a nucleoprotein using digital ELISA," *Analytical chemistry,* vol. 88, no. 17, pp. 8450-8458, 2016.

[79] L. Cohen and D. R. Walt, "Single-Molecule Arrays for Protein and Nucleic Acid Analysis," (in English), *Annual Review of Analytical Chemistry, Vol 10,* vol. 10, pp. 345-363, 2017.

[80] W. H. Guan, L. B. Chen, T. D. Rane, and T. H. Wang, "Droplet Digital Enzyme-Linked Oligonucleotide Hybridization Assay for Absolute RNA Quantification," (in English), *Scientific Reports,* vol. 5, p. 13795, Sep 3 2015.

[81] P. Rowghanian and A. Y. Grosberg, "Electrophoretic capture of a DNA chain into a nanopore," *Physical Review E,* vol. 87, no. 4, p. 042722, 2013.

[82] S. K. Nomidis, J. Hooyberghs, G. Maglia, and E. Carlon, "DNA capture into the ClyA nanopore: diffusion-limited versus reaction-limited processes," *J Phys Condens Matter,* vol. 30, no. 30, p. 304001, Aug 1 2018.

[83] M. Wanunu, W. Morrison, Y. Rabin, A. Y. Grosberg, and A. Meller, "Electrostatic focusing of unlabelled DNA into nanoscale pores using a salt gradient," *Nature nanotechnology,* vol. 5, no. 2, p. 160, 2010.

[84] B. McNally, M. Wanunu, and A. Meller, "Electromechanical unzipping of individual DNA molecules using synthetic sub-2 nm pores," *Nano letters,* vol. 8, no. 10, pp. 3418-3422, 2008.

[85] B. M. Venkatesan and R. Bashir, "Nanopore sensors for nucleic acid analysis," *Nature nanotechnology,* vol. 6, no. 10, p. 615, 2011.

[86] K. Liu *et al.*, "Detecting topological variations of DNA at single-molecule level," *Nature communications,* vol. 10, no. 1, p. 3, 2019.

[87] N. Varongchayakul, J. S. Hersey, A. Squires, A. Meller, and M. W. Grinstaff, "A Solid‐State Hard Microfluidic–Nanopore Biosensor with Multilayer Fluidics and On‐Chip Bioassay/Purification Chamber," *Advanced Functional Materials,* vol. 28, no. 50, p. 1804182, 2018.

[88] C. Plesa *et al.*, "Direct observation of DNA knots using a solid-state nanopore," *Nature nanotechnology,* vol. 11, no. 12, p. 1093, 2016.

[89] K. J. Freedman, L. M. Otto, A. P. Ivanov, A. Barik, S.-H. Oh, and J. B. Edel, "Nanopore sensing at ultra-low concentrations using single-molecule dielectrophoretic trapping," *Nature communications,* vol. 7, p. 10217, 2016.

[90] F. Piguet, H. Ouldali, M. Pastoriza-Gallego, P. Manivet, J. Pelta, and A. Oukhaled, "Identification of single amino acid differences in uniformly charged homopolymeric peptides with aerolysin nanopore," *Nature communications,* vol. 9, no. 1, p. 966, 2018.

[91] L. Harrington, L. T. Alexander, S. Knapp, and H. Bayley, "Single-Molecule Protein Phosphorylation and Dephosphorylation by Nanopore Enzymology," *ACS nano,* vol. 13, no. 1, pp. 633-641, 2018.

[92] Z. Long, S. Zhan, P. Gao, Y. Wang, X. Lou, and F. Xia, "Recent advances in solid nanopore/channel analysis," *Analytical chemistry,* vol. 90, no. 1, pp. 577-588, 2017.

[93] X. Xu *et al.*, "Highly robust nanopore-based dual-signal-output ion detection system for achieving three successive calibration curves," *Analytical chemistry,* vol. 88, no. 4, pp. 2386-2391, 2016.

[94] A. Y. Grosberg and Y. Rabin, "DNA capture into a nanopore: interplay of diffusion and electrohydrodynamics," *The Journal of chemical physics,* vol. 133, no. 16, p. 10B617, 2010.

[95] T. Albrecht, "Single-Molecule Analysis with Solid-State Nanopores," *Annual Review of Analytical Chemistry,* vol. 12, pp. 5.1–5.17, 2019.

[96] M. Wanunu, J. Sutin, B. McNally, A. Chow, and A. Meller, "DNA translocation governed by interactions with solid-state nanopores," *Biophysical journal,* vol. 95, no. 10, pp. 4716-4725, 2008.

[97] L.-Q. Gu, M. Wanunu, M. X. Wang, L. McReynolds, and Y. Wang, "Detection of miRNAs with a nanopore single-molecule counter," *Expert review of molecular diagnostics,* vol. 12, no. 6, pp. 573-584, 2012.

[98] K. J. Freedman *et al.*, "Nonequilibrium capture rates induce protein accumulation and enhanced adsorption to solid-state nanopores," *ACS nano,* vol. 8, no. 12, pp. 12238-12249, 2014.

[99] M. Wanunu, T. Dadosh, V. Ray, J. Jin, L. McReynolds, and M. Drndić, "Rapid electronic detection of probe-specific microRNAs using thin nanopore sensors," *Nature nanotechnology,* vol. 5, no. 11, p. 807, 2010.

[100] A. Meller and D. Branton, "Single molecule measurements of DNA transport through a nanopore," *Electrophoresis,* vol. 23, no. 16, pp. 2583-2591, 2002.

[101] D. V. Verschueren, M. P. Jonsson, and C. Dekker, "Temperature dependence of DNA translocations through solid-state nanopores," *Nanotechnology,* vol. 26, no. 23, p. 234004, 2015.

[102] S. E. Henrickson, M. Misakian, B. Robertson, and J. J. Kasianowicz, "Driven DNA transport into an asymmetric nanometer-scale pore," *Physical Review Letters,* vol. 85, no. 14, p. 3057, 2000.

[103] D. Fologea, J. Uplinger, B. Thomas, D. S. McNabb, and J. Li, "Slowing DNA translocation in a solid-state nanopore," *Nano letters,* vol. 5, no. 9, pp. 1734-1737, 2005.

[104] Z. Tang, B. Lu, Q. Zhao, J. Wang, K. Luo, and D. Yu, "Surface Modification of Solid‐State Nanopores for Sticky‐Free Translocation of Single‐Stranded DNA," *Small,* vol. 10, no. 21, pp. 4332-4339, 2014.

[105] G. Ando, C. Hyun, J. Li, and T. Mitsui, "Directly observing the motion of DNA molecules near solid-state nanopores," *ACS nano,* vol. 6, no. 11, pp. 10090-10097, 2012.

[106] N. Laohakunakorn, V. V. Thacker, M. Muthukumar, and U. F. Keyser, "Electroosmotic Flow Reversal Outside Glass Nanopores," (in English), *Nano Letters,* vol. 15, no. 1, pp. 695-702, Jan 2015.

[107] Y.-H. Sen and R. Karnik, "Investigating the translocation of λ-DNA molecules through PDMS nanopores," *Analytical and bioanalytical chemistry,* vol. 394, no. 2, pp. 437-446, 2009.
[108] V. Patil and H. Kulkarni, "Comparison of confidence intervals for the Poisson mean: some new aspects," *REVSTAT-Statistical Journal,* vol. 10, no. 2, pp. 211-227, 2012.
[109] P. Chen, J. Gu, E. Brandin, Y.-R. Kim, Q. Wang, and D. Branton, "Probing single dna molecule transport using fabricated nanopores," *Nano letters,* vol. 4, no. 11, pp. 2293-2298, 2004.
[110] M. Gershow and J. A. Golovchenko, "Recapturing and trapping single molecules with a solid-state nanopore," *Nature nanotechnology,* vol. 2, no. 12, p. 775, 2007.
[111] P. Terejánszky, I. Makra, P. t. Fürjes, and R. b. E. Gyurcsányi, "Calibration-less sizing and quantitation of polymeric nanoparticles and viruses with quartz nanopipets," *Analytical chemistry,* vol. 86, no. 10, pp. 4688-4697, 2014.
[112] M. Van den Hout, A. R. Hall, M. Y. Wu, H. W. Zandbergen, C. Dekker, and N. H. Dekker, "Controlling nanopore size, shape and stability," *Nanotechnology,* vol. 21, no. 11, p. 115304, 2010.
[113] C. M. Frament and J. R. Dwyer, "Conductance-based determination of solid-state nanopore size and shape: an exploration of performance limits," *The journal of physical chemistry C,* vol. 116, no. 44, pp. 23315-23321, 2012.
[114] K. W. Pratt, W. Koch, Y. C. Wu, and P. Berezansky, "Molality-based primary standards of electrolytic conductivity (IUPAC Technical Report)," *Pure and applied chemistry,* vol. 73, no. 11, pp. 1783-1793, 2001.
[115] D. Long, J.-L. Viovy, and A. Ajdari, "Simultaneous action of electric fields and nonelectric forces on a polyelectrolyte: motion and deformation," *Physical review letters,* vol. 76, no. 20, p. 3858, 1996.
[116] A. E. Nkodo *et al.*, "Diffusion coefficient of DNA molecules during free solution electrophoresis," *Electrophoresis,* vol. 22, no. 12, pp. 2424-2432, 2001.
[117] B. M. Olivera, P. Baine, and N. Davidson, "Electrophoresis of the nucleic acids," *Biopolymers: Original Research on Biomolecules,* vol. 2, no. 3, pp. 245-257, 1964.
[118] S. Takeuchi, J. Kim, Y. Yamamoto, and H. H. Hogue, "Development of a high-quantum-efficiency single-photon counting system," *Applied Physics Letters,* vol. 74, no. 8, pp. 1063-1065, 1999.
[119] R. Smeets, S. W. Kowalczyk, A. Hall, N. Dekker, and C. Dekker, "Translocation of RecA-coated double-stranded DNA through solid-state nanopores," *Nano letters,* vol. 9, no. 9, pp. 3089-3095, 2009.
[120] Z. Tang, G. Choi, R. Nouri, and W. Guan, "Loop-Mediated Isothermal Amplification-Coupled Glass Nanopore Counting Toward Sensitive and Specific Nucleic Acid Testing," *Nano letters,* vol. 19, no. 11, pp. 7927-7934, 2019.
[121] S. Garaj, W. Hubbard, A. Reina, J. Kong, D. Branton, and J. Golovchenko, "Graphene as a subnanometre trans-electrode membrane," *Nature,* vol. 467, no. 7312, pp. 190-193, 2010.
[122] B. N. Miles, A. P. Ivanov, K. A. Wilson, F. Doğan, D. Japrung, and J. B. Edel, "Single molecule sensing with solid-state nanopores: novel materials, methods, and applications," *Chemical Society Reviews,* vol. 42, no. 1, pp. 15-28, 2013.
[123] U. F. Keyser, "Enhancing nanopore sensing with DNA nanotechnology," *Nature nanotechnology,* vol. 11, no. 2, p. 106, 2016.
[124] S. M. Iqbal, D. Akin, and R. Bashir, "Solid-state nanopore channels with DNA selectivity," *Nature nanotechnology,* vol. 2, no. 4, p. 243, 2007.

[125] R. Wei, V. Gatterdam, R. Wieneke, R. Tampé, and U. Rant, "Stochastic sensing of proteins with receptor-modified solid-state nanopores," *Nature nanotechnology,* vol. 7, no. 4, p. 257, 2012.

[126] J. Y. Sze, A. P. Ivanov, A. E. Cass, and J. B. Edel, "Single molecule multiplexed nanopore protein screening in human serum using aptamer modified DNA carriers," *Nature communications,* vol. 8, no. 1, pp. 1-10, 2017.

[127] J. Kong, J. Zhu, and U. F. Keyser, "Single molecule based SNP detection using designed DNA carriers and solid-state nanopores," *Chemical Communications,* vol. 53, no. 2, pp. 436-439, 2017.

[128] N. A. Bell and U. F. Keyser, "Specific protein detection using designed DNA carriers and nanopores," *Journal of the American Chemical Society,* vol. 137, no. 5, pp. 2035-2041, 2015.

[129] L. Cong *et al.*, "Multiplex genome engineering using CRISPR/Cas systems," *Science,* vol. 339, no. 6121, pp. 819-823, 2013.

[130] P. Qin *et al.*, "Rapid and fully microfluidic Ebola virus detection with CRISPR-Cas13a," *ACS sensors,* vol. 4, no. 4, pp. 1048-1054, 2019.

[131] W. Yang *et al.*, "Detection of CRISPR-dCas9 on DNA with solid-state nanopores," *Nano letters,* vol. 18, no. 10, pp. 6469-6474, 2018.

[132] N. E. Weckman *et al.*, "Multiplexed DNA identification using site specific dCas9 barcodes and nanopore sensing," *ACS sensors,* vol. 4, no. 8, pp. 2065-2072, 2019.

[133] R. D. Bulushev, S. Marion, E. Petrova, S. J. Davis, S. J. Maerkl, and A. Radenovic, "Single Molecule Localization and Discrimination of DNA–Protein Complexes by Controlled Translocation Through Nanocapillaries," *Nano letters,* vol. 16, no. 12, pp. 7882-7890, 2016.

[134] Y. Li, S. Li, J. Wang, and G. Liu, "CRISPR/Cas systems towards next-generation biosensing," *Trends in biotechnology,* vol. 37, no. 7, pp. 730-743, 2019.

[135] Q. He *et al.*, "High-throughput and all-solution phase African Swine Fever Virus (ASFV) detection using CRISPR-Cas12a and fluorescence based point-of-care system," *Biosensors and Bioelectronics,* vol. 154, p. 112068, 2020.

[136] J. S. Gootenberg, O. O. Abudayyeh, M. J. Kellner, J. Joung, J. J. Collins, and F. Zhang, "Multiplexed and portable nucleic acid detection platform with Cas13, Cas12a, and Csm6," *Science,* vol. 360, no. 6387, pp. 439-444, 2018.

[137] J. S. Gootenberg *et al.*, "Nucleic acid detection with CRISPR-Cas13a/C2c2," *Science,* vol. 356, no. 6336, pp. 438-442, 2017.

[138] S.-Y. Li, Q.-X. Cheng, J.-K. Liu, X.-Q. Nie, G.-P. Zhao, and J. Wang, "CRISPR-Cas12a has both cis-and trans-cleavage activities on single-stranded DNA," *Cell research,* vol. 28, no. 4, pp. 491-493, 2018.

[139] J. S. Chen *et al.*, "CRISPR-Cas12a target binding unleashes indiscriminate single-stranded DNase activity," *Science,* vol. 360, no. 6387, pp. 436-439, 2018.

[140] B. Wang *et al.*, "Cas12aVDet: a CRISPR/Cas12a-based platform for rapid and visual nucleic acid detection," *Analytical chemistry,* vol. 91, no. 19, pp. 12156-12161, 2019.

[141] C. Rouzioux and V. Avettand-Fenoël, "Total HIV DNA: a global marker of HIV persistence," *Retrovirology,* vol. 15, no. 1, p. 30, 2018.

[142] S.-Y. Li *et al.*, "CRISPR-Cas12a-assisted nucleic acid detection," *Cell discovery,* vol. 4, no. 1, pp. 1-4, 2018.

[143] R. Nouri, Z. Tang, and W. Guan, "Quantitative Analysis of Factors Affecting the Event Rate in Glass Nanopore Sensors," *ACS sensors,* vol. 4, no. 11, pp. 3007-3013, 2019.

[144] J. Zhao, L. Chang, and L. Wang, "Nucleic acid testing and molecular characterization of HIV infections," *European Journal of Clinical Microbiology & Infectious Diseases,* vol. 38, no. 5, pp. 829-842, 2019.

[145] D. Schlatzer, A. A. Haqqani, X. Li, C. Dobrowolski, M. R. Chance, and J. C. Tilton, "A targeted mass spectrometry assay for detection of HIV gag protein following induction of latent viral reservoirs," *Analytical chemistry,* vol. 89, no. 10, pp. 5325-5332, 2017.

[146] A. A. Waheed and E. O. Freed, "HIV type 1 Gag as a target for antiviral therapy," *AIDS research and human retroviruses,* vol. 28, no. 1, pp. 54-75, 2012.

[147] M. Huang, X. Zhou, H. Wang, and D. Xing, "Clustered regularly interspaced short palindromic repeats/Cas9 triggered isothermal amplification for site-specific nucleic acid detection," *Analytical chemistry,* vol. 90, no. 3, pp. 2193-2200, 2018.

[148] R. T. Fuchs, J. Curcuru, M. Mabuchi, P. Yourik, and G. B. Robb, "Cas12a trans-cleavage can be modulated in vitro and is active on ssDNA, dsDNA, and RNA," *bioRxiv,* p. 600890, 2019.

[149] N. Ermann, N. Hanikel, V. Wang, K. Chen, N. E. Weckman, and U. F. Keyser, "Promoting single-file DNA translocations through nanopores using electro-osmotic flow," *The Journal of chemical physics,* vol. 149, no. 16, p. 163311, 2018.

[150] I. Strohkendl, F. A. Saifuddin, J. R. Rybarski, I. J. Finkelstein, and R. Russell, "Kinetic basis for DNA target specificity of CRISPR-Cas12a," *Molecular cell,* vol. 71, no. 5, pp. 816-824. e3, 2018.

[151] V. Patil and H. Kulkarni, "Comparison of confidence intervals for the Poisson mean: some new aspects," *REVSTAT–Statistical Journal,* vol. 10, no. 2, pp. 211-227, 2012.

[152] J.-F. Mercier and G. W. Slater, "An exactly solvable Ogston model of gel electrophoresis. 7. Diffusion and mobility of hard spherical particles in three-dimensional gels," *Macromolecules,* vol. 34, no. 10, pp. 3437-3445, 2001.

[153] G. W. Slater and H. L. Guo, "Ogston gel electrophoretic sieving: How is the fractional volume available to a particle related to its mobility and diffusion coefficient (s)?," *Electrophoresis,* vol. 16, no. 1, pp. 11-15, 1995.

[154] P. Zhou *et al.*, "A pneumonia outbreak associated with a new coronavirus of probable bat origin," *nature,* vol. 579, no. 7798, pp. 270-273, 2020.

[155] N. Zhu *et al.*, "A novel coronavirus from patients with pneumonia in China, 2019," *New England journal of medicine,* vol. 382, pp. 727-733, 2019.

[156] R. Lu *et al.*, "Genomic characterisation and epidemiology of 2019 novel coronavirus: implications for virus origins and receptor binding," *The lancet,* vol. 395, no. 10224, pp. 565-574, 2020.

[157] M. Chiara *et al.*, "Next generation sequencing of SARS-CoV-2 genomes: challenges, applications and opportunities," *Briefings in Bioinformatics,* vol. 22, no. 2, pp. 616-630, 2021.

[158] M.-M. Aynaud *et al.*, "A multiplexed, next generation sequencing platform for high-throughput detection of SARS-CoV-2," *Nature communications,* vol. 12, no. 1, pp. 1-10, 2021.

[159] R. C. Bhoyar *et al.*, "High throughput detection and genetic epidemiology of SARS-CoV-2 using COVIDSeq next-generation sequencing," *PloS one,* vol. 16, no. 2, p. e0247115, 2021.

[160] J. V. Dzimianski, N. Lorig-Roach, S. M. O'Rourke, D. L. Alexander, J. M. Kimmey, and R. M. DuBois, "Rapid and sensitive detection of SARS-CoV-2 antibodies by biolayer interferometry," *Scientific reports,* vol. 10, no. 1, pp. 1-12, 2020.

[161] Q.-B. Meng *et al.*, "Clinical application of combined detection of SARS-CoV-2-specific antibody and nucleic acid," *World journal of clinical cases,* vol. 8, no. 19, p. 4360, 2020.

[162] A. Petherick, "Developing antibody tests for SARS-CoV-2," *The Lancet,* vol. 395, no. 10230, pp. 1101-1102, 2020.
[163] B. Udugama *et al.*, "Diagnosing COVID-19: the disease and tools for detection," *ACS nano,* vol. 14, no. 4, pp. 3822-3835, 2020.
[164] P. Jokela *et al.*, "SARS-CoV-2 sample-to-answer nucleic acid testing in a tertiary care emergency department: evaluation and utility," *Journal of Clinical Virology,* vol. 131, p. 104614, 2020.
[165] J. A. Doudna and E. Charpentier, "The new frontier of genome engineering with CRISPR-Cas9," *Science,* vol. 346, no. 6213, 2014.
[166] O. O. Abudayyeh, J. S. Gootenberg, M. J. Kellner, and F. Zhang, "Nucleic acid detection of plant genes using CRISPR-Cas13," *The CRISPR Journal,* vol. 2, no. 3, pp. 165-171, 2019.
[167] R. Bruch *et al.*, "CRISPR/Cas13a ‐ powered electrochemical microfluidic biosensor for nucleic acid amplification ‐ free miRNA diagnostics," *Advanced Materials,* vol. 31, no. 51, p. 1905311, 2019.
[168] N. Shao, X. Han, Y. Song, P. Zhang, and L. Qin, "CRISPR-Cas12a Coupled with Platinum Nanoreporter for Visual Quantification of SNVs on a Volumetric Bar-Chart Chip," *Analytical chemistry,* vol. 91, no. 19, pp. 12384-12391, 2019.
[169] L. Li *et al.*, "HOLMESv2: a CRISPR-Cas12b-assisted platform for nucleic acid detection and DNA methylation quantitation," *ACS synthetic biology,* vol. 8, no. 10, pp. 2228-2237, 2019.
[170] M. J. Kellner, J. G. Koob, J. S. Gootenberg, O. O. Abudayyeh, and F. Zhang, "SHERLOCK: nucleic acid detection with CRISPR nucleases," *Nature protocols,* vol. 14, no. 10, pp. 2986-3012, 2019.
[171] C. Yuan *et al.*, "Universal and Naked-Eye Gene Detection Platform Based on the Clustered Regularly Interspaced Short Palindromic Repeats/Cas12a/13a System," *Analytical Chemistry,* vol. 92, no. 5, pp. 4029-4037, 2020.
[172] J. N. Rauch *et al.*, "A scalable, easy-to-deploy protocol for Cas13-based detection of SARS-CoV-2 genetic material," *Journal of clinical microbiology,* vol. 59, no. 4, pp. e02402-20, 2021.
[173] C. Qian, H. Wu, Y. Shi, J. Wu, and H. Chen, "Dehydrated CRISPR-mediated DNA analysis for visualized animal-borne virus sensing in the unprocessed blood sample," *Sensors and Actuators B: Chemical,* vol. 305, p. 127440, 2020.
[174] C. c. Chenot, R. l. Robiette, and S. Collin, "First evidence of the cysteine and glutathione conjugates of 3-sulfanylpentan-1-ol in hop (Humulus lupulus L.)," *Journal of agricultural and food chemistry,* vol. 67, no. 14, pp. 4002-4010, 2019.
[175] T. J. Sullivan, A. K. Dhar, R. Cruz-Flores, and A. G. Bodnar, "Rapid, CRISPR-based, field-deployable detection of white spot syndrome virus in shrimp," *Scientific reports,* vol. 9, no. 1, pp. 1-7, 2019.
[176] O. O. Abudayyeh *et al.*, "C2c2 is a single-component programmable RNA-guided RNA-targeting CRISPR effector," *Science,* vol. 353, no. 6299, p. 5573, 2016.
[177] M. Patchsung *et al.*, "Clinical validation of a Cas13-based assay for the detection of SARS-CoV-2 RNA," *Nature Biomedical Engineering,* vol. 4, no. 12, pp. 1140-1149, 2020.
[178] L. B. Harrington *et al.*, "Programmed DNA destruction by miniature CRISPR-Cas14 enzymes," *Science,* vol. 362, no. 6416, pp. 839-842, 2018.
[179] R. Nouri, Z. Tang, M. Dong, T. Liu, A. Kshirsagar, and W. Guan, "CRISPR-based detection of SARS-CoV-2: A review from sample to result," *Biosensors and Bioelectronics,* vol. 178, p. 113012, 2021.

[180] J. P. Broughton *et al.*, "CRISPR–Cas12-based detection of SARS-CoV-2," *Nature Biotechnology,* vol. 38, no. 7, pp. 870-874, 2020/07/01 2020.
[181] Z. Ali *et al.*, "iSCAN: An RT-LAMP-coupled CRISPR-Cas12 module for rapid, sensitive detection of SARS-CoV-2," *Virus research,* vol. 288, p. 198129, 2020.
[182] X. Ding *et al.*, "Ultrasensitive and visual detection of SARS-CoV-2 using all-in-one dual CRISPR-Cas12a assay," *Nature communications,* vol. 11, no. 1, pp. 1-10, 2020.
[183] L. Guo *et al.*, "SARS-CoV-2 detection with CRISPR diagnostics," *Cell Discovery,* vol. 6, no. 1, pp. 1-4, 2020.
[184] J. Arizti-Sanz *et al.*, "Streamlined inactivation, amplification, and Cas13-based detection of SARS-CoV-2," *Nature communications,* vol. 11, no. 1, pp. 1-9, 2020.
[185] T. R. Abbott *et al.*, "Development of CRISPR as an antiviral strategy to combat SARS-CoV-2 and influenza," *Cell,* vol. 181, no. 4, pp. 865-876. e12, 2020.
[186] R. Wang *et al.*, "opvCRISPR: One-pot visual RT-LAMP-CRISPR platform for SARS-cov-2 detection," *Biosensors and Bioelectronics,* vol. 172, p. 112766, 2021.
[187] B. Ning *et al.*, "A smartphone-read ultrasensitive and quantitative saliva test for COVID-19," *Science advances,* vol. 7, no. 2, p. eabe3703, 2021.
[188] J. E. van Dongen, J. T. Berendsen, R. D. Steenbergen, R. M. Wolthuis, J. C. Eijkel, and L. I. Segerink, "Point-of-care CRISPR/Cas nucleic acid detection: recent advances, challenges and opportunities," *Biosensors and Bioelectronics,* vol. 166, p. 112445, 2020.
[189] Y. Dai *et al.*, "Exploring the Trans‐Cleavage Activity of CRISPR‐Cas12a (cpf1) for the Development of a Universal Electrochemical Biosensor," *Angewandte Chemie,* vol. 131, no. 48, pp. 17560-17566, 2019.
[190] W. Xu, T. Jin, Y. Dai, and C. C. Liu, "Surpassing the detection limit and accuracy of the electrochemical DNA sensor through the application of CRISPR Cas systems," *Biosensors and Bioelectronics,* vol. 155, p. 112100, 2020.
[191] D. Zhang *et al.*, "CRISPR/Cas12a-Mediated interfacial cleaving of hairpin DNA reporter for electrochemical nucleic acid sensing," *ACS sensors,* vol. 5, no. 2, pp. 557-562, 2020.
[192] R. Hajian *et al.*, "Detection of unamplified target genes via CRISPR–Cas9 immobilized on a graphene field-effect transistor," *Nature biomedical engineering,* vol. 3, no. 6, pp. 427-437, 2019.
[193] R. Nouri, Y. Jiang, X. L. Lian, and W. Guan, "Sequence-specific recognition of HIV-1 DNA with solid-state CRISPR-Cas12a-assisted nanopores (SCAN)," *ACS sensors,* vol. 5, no. 5, pp. 1273-1280, 2020.
[194] D. Fologea, E. Brandin, J. Uplinger, D. Branton, and J. Li, "DNA conformation and base number simultaneously determined in a nanopore," *Electrophoresis,* vol. 28, no. 18, pp. 3186-3192, 2007.
[195] D. Fologea, M. Gershow, B. Ledden, D. S. McNabb, J. A. Golovchenko, and J. Li, "Detecting single stranded DNA with a solid state nanopore," *Nano letters,* vol. 5, no. 10, pp. 1905-1909, 2005.
[196] S. W. Kowalczyk, A. Y. Grosberg, Y. Rabin, and C. Dekker, "Modeling the conductance and DNA blockade of solid-state nanopores," *Nanotechnology,* vol. 22, no. 31, p. 315101, 2011.
[197] I. Makra and R. E. Gyurcsányi, "Electrochemical sensing with nanopores: A mini review," *Electrochemistry communications,* vol. 43, pp. 55-59, 2014.
[198] X. Lu *et al.*, "US CDC real-time reverse transcription PCR panel for detection of severe acute respiratory syndrome coronavirus 2," *Emerging infectious diseases,* vol. 26, no. 8, p. 1654, 2020.

[199] T. Duke, J. L. Viovy, and A. N. Semenov, "Electrophoretic mobility of DNA in gels. I. New biased reptation theory including fluctuations," *Biopolymers: Original Research on Biomolecules,* vol. 34, no. 2, pp. 239-247, 1994.

[200] A. Ramachandran and J. G. Santiago, "CRISPR Enzyme Kinetics for Molecular Diagnostics," *Analytical Chemistry,* vol. 93, no. 20, pp. 7456–7464, 2021.

[201] S. M. Alonso Villela, H. Kraiem, B. Bouhaouala‐Zahar, C. Bideaux, C. A. Aceves Lara, and L. Fillaudeau, "A protocol for recombinant protein quantification by densitometry," *MicrobiologyOpen,* vol. 9, no. 6, pp. 1175-1182, 2020.

[202] B. McKenzie, G. Kay, K. H. Matthews, R. M. Knott, and D. Cairns, "The hen's egg chorioallantoic membrane (HET-CAM) test to predict the ophthalmic irritation potential of a cysteamine-containing gel: Quantification using Photoshop® and ImageJ," *International journal of pharmaceutics,* vol. 490, no. 1-2, pp. 1-8, 2015.

[203] K. Benschop, R. Molenkamp, A. van der Ham, K. Wolthers, and M. Beld, "Rapid detection of human parechoviruses in clinical samples by real-time PCR," *Journal of Clinical Virology,* vol. 41, no. 2, pp. 69-74, 2008.

[204] C. A. Holstein, M. Griffin, J. Hong, and P. D. Sampson, "Statistical method for determining and comparing limits of detection of bioassays," *Analytical chemistry,* vol. 87, no. 19, pp. 9795-9801, 2015.

[205] A. Forootan, R. Sjöback, J. Björkman, B. Sjögreen, L. Linz, and M. Kubista, "Methods to determine limit of detection and limit of quantification in quantitative real-time PCR (qPCR)," *Biomolecular detection and quantification,* vol. 12, pp. 1-6, 2017.

[206] A. C. Komor, A. H. Badran, and D. R. Liu, "CRISPR-based technologies for the manipulation of eukaryotic genomes," *Cell,* vol. 168, no. 1-2, pp. 20-36, 2017.

[207] K. Pardee *et al.*, "Rapid, low-cost detection of Zika virus using programmable biomolecular components," *Cell,* vol. 165, no. 5, pp. 1255-1266, 2016.

[208] W. Zhou, L. Hu, L. Ying, Z. Zhao, P. K. Chu, and X.-F. Yu, "A CRISPR–Cas9-triggered strand displacement amplification method for ultrasensitive DNA detection," *Nature communications,* vol. 9, no. 1, pp. 1-11, 2018.

[209] J. Quan *et al.*, "FLASH: a next-generation CRISPR diagnostic for multiplexed detection of antimicrobial resistance sequences," *Nucleic acids research,* vol. 47, no. 14, pp. e83-e83, 2019.

[210] T. Wang, Y. Liu, H. H. Sun, B. C. Yin, and B. C. Ye, "An RNA‐guided Cas9 nickase‐based method for universal isothermal DNA amplification," *Angewandte Chemie,* vol. 131, no. 16, pp. 5436-5440, 2019.

[211] C. Myhrvold *et al.*, "Field-deployable viral diagnostics using CRISPR-Cas13," *Science,* vol. 360, no. 6387, pp. 444-448, 2018.

[212] T. Zhou, R. Huang, M. Huang, J. Shen, Y. Shan, and D. Xing, "CRISPR/Cas13a powered portable electrochemiluminescence chip for ultrasensitive and specific MiRNA detection," *Advanced Science,* vol. 7, no. 13, p. 1903661, 2020.

[213] M. M. Kaminski, O. O. Abudayyeh, J. S. Gootenberg, F. Zhang, and J. J. Collins, "CRISPR-based diagnostics," *Nature Biomedical Engineering,* vol. 5, no. 7, pp. 643-656, 2021.

[214] X. Wang, X. Shang, and X. Huang, "Next-generation pathogen diagnosis with CRISPR/Cas-based detection methods," *Emerging microbes & infections,* vol. 9, no. 1, pp. 1682-1691, 2020.

[215] M. Wang, R. Zhang, and J. Li, "CRISPR/cas systems redefine nucleic acid detection: principles and methods," *Biosensors and Bioelectronics,* vol. 165, p. 112430, 2020.

[216] A. Ramachandran and J. G. Santiago, "CRISPR Enzyme Kinetics for Molecular Diagnostics," *Analytical Chemistry,* vol. 93, no. 20, pp. 7456-7464, 2021.
[217] W. X. Yan *et al.*, "Cas13d is a compact RNA-targeting type VI CRISPR effector positively modulated by a WYL-domain-containing accessory protein," *Molecular cell,* vol. 70, no. 2, pp. 327-339. e5, 2018.
[218] X. Ding, K. Yin, Z. Li, M. M. Sfeir, and C. Liu, "Sensitive quantitative detection of SARS-CoV-2 in clinical samples using digital warm-start CRISPR assay," *Biosensors and Bioelectronics,* vol. 184, p. 113218, 2021.
[219] A. Lau, C. Ren, and L. P. Lee, "Critical review on where CRISPR meets molecular diagnostics," *Progress in Biomedical Engineering,* vol. 3, no. 1, p. 012001, 2020/12/22 2020.
[220] B. Zetsche *et al.*, "Cpf1 is a single RNA-guided endonuclease of a class 2 CRISPR-Cas system," *Cell,* vol. 163, no. 3, pp. 759-771, 2015.
[221] O. O. Abudayyeh and J. S. Gootenberg, "CRISPR diagnostics," *Science,* vol. 372, no. 6545, pp. 914-915, 2021.
[222] B. P. English *et al.*, "Ever-fluctuating single enzyme molecules: Michaelis-Menten equation revisited," *Nature chemical biology,* vol. 2, no. 2, pp. 87-94, 2006.
[223] R. Nouri, Y. Jiang, Z. Tang, X. L. Lian, and W. Guan, "Detection of SARS-CoV-2 with Solid-State CRISPR-Cas12a-Assisted Nanopores," *Nano letters,* vol. 21, no. 19, pp. 8393-8400, 2021.
[224] M. A. English *et al.*, "Programmable CRISPR-responsive smart materials," *Science,* vol. 365, no. 6455, pp. 780-785, 2019.
[225] J. Joung *et al.*, "Detection of SARS-CoV-2 with SHERLOCK one-pot testing," *New England Journal of Medicine,* vol. 383, no. 15, pp. 1492-1494, 2020.
[226] V. L. D. Thi *et al.*, "A colorimetric RT-LAMP assay and LAMP-sequencing for detecting SARS-CoV-2 RNA in clinical samples," *Science Translational Medicine,* vol. 12, no. 556, p. eabc7075, 2020.
[227] M. Higgins *et al.*, "PrimedRPA: Primer design for recombinase polymerase amplification assays," *Bioinformatics,* vol. 35, no. 4, pp. 682-684, 2019.
[228] N. Tomita, Y. Mori, H. Kanda, and T. Notomi, "Loop-mediated isothermal amplification (LAMP) of gene sequences and simple visual detection of products," *Nature protocols,* vol. 3, no. 5, pp. 877-882, 2008.
[229] D. McDowell, "The polymerase chain reaction patents: going, going,… still going," *Journal of the Royal Society of Medicine,* vol. 99, no. 2, pp. 62-64, 2006.
[230] C. Bezier, G. Anthoine, and A. Charki, "Reliability of real-time RT-PCR tests to detect SARS-Cov-2: A literature review," *International Journal of Metrology and Quality Engineering,* vol. 11, 2020.
[231] G. A. Obande and K. K. B. Singh, "Current and future perspectives on isothermal nucleic acid amplification technologies for diagnosing infections," *Infection and drug resistance,* vol. 13, p. 455, 2020.
[232] A. T. Keizerweerd, A. Chandra, and M. P. Grisham, "Development of a reverse transcription loop-mediated isothermal amplification (RT-LAMP) assay for the detection of Sugarcane mosaic virus and Sorghum mosaic virus in sugarcane," *Journal of virological methods,* vol. 212, pp. 23-29, 2015.
[233] W. E. Huang *et al.*, "RT‐LAMP for rapid diagnosis of coronavirus SARS‐CoV‐2," *Microbial biotechnology,* vol. 13, no. 4, pp. 950-961, 2020.

[234] J.-j. Li, C. Xiong, Y. Liu, J.-s. Liang, and X.-w. Zhou, "Loop-mediated isothermal amplification (LAMP): emergence as an alternative technology for herbal medicine identification," *Frontiers in plant science,* vol. 7, p. 1956, 2016.

[235] J. Li, J. Macdonald, and F. von Stetten, "a comprehensive summary of a decade development of the recombinase polymerase amplification," *Analyst,* vol. 144, no. 1, pp. 31-67, 2018.

[236] P. Hardinge and J. A. Murray, "Lack of specificity associated with using molecular beacons in loop mediated amplification assays," *BMC biotechnology,* vol. 19, no. 1, pp. 1-15, 2019.

[237] S. Lee, V. S. L. Khoo, C. A. D. Medriano, T. Lee, S.-Y. Park, and S. Bae, "Rapid and in-situ detection of fecal indicator bacteria in water using simple DNA extraction and portable loop-mediated isothermal amplification (LAMP) PCR methods," *Water research,* vol. 160, pp. 371-379, 2019.

[238] Y.-D. Wu *et al.*, "Recombinase polymerase amplification (RPA) combined with lateral flow (LF) strip for equipment-free detection of Cryptosporidium spp. oocysts in dairy cattle feces," *Parasitology research,* vol. 115, no. 9, pp. 3551-3555, 2016.

[239] L. Liu *et al.*, "Visual and equipment-free reverse transcription recombinase polymerase amplification method for rapid detection of foot-and-mouth disease virus," *BMC veterinary research,* vol. 14, no. 1, pp. 1-8, 2018.

[240] L. Liu *et al.*, "Equipment-free recombinase polymerase amplification assay using body heat for visual and rapid point-of-need detection of canine parvovirus 2," *Molecular and cellular probes,* vol. 39, pp. 41-46, 2018.

[241] L. T. Nguyen, B. M. Smith, and P. K. Jain, "Enhancement of trans-cleavage activity of Cas12a with engineered crRNA enables amplified nucleic acid detection," *Nature communications,* vol. 11, no. 1, pp. 1-13, 2020.

[242] H. Yue *et al.*, "Droplet Cas12a Assay Enables DNA Quantification from Unamplified Samples at the Single-Molecule Level," *Nano Letters,* vol. 21, no. 11, pp. 4643-4653, 2021.

[243] J. C. Cofsky, D. Karandur, C. J. Huang, I. P. Witte, J. Kuriyan, and J. A. Doudna, "CRISPR-Cas12a exploits R-loop asymmetry to form double-strand breaks," *Elife,* vol. 9, p. e55143, 2020.

[244] I. M. Slaymaker *et al.*, "High-resolution structure of Cas13b and biochemical characterization of RNA targeting and cleavage," *Cell reports,* vol. 26, no. 13, pp. 3741-3751. e5, 2019.

[245] Y. Shan, X. Zhou, R. Huang, and D. Xing, "High-fidelity and rapid quantification of miRNA combining crRNA programmability and CRISPR/Cas13a trans-cleavage activity," *Analytical chemistry,* vol. 91, no. 8, pp. 5278-5285, 2019.

[246] P. Fozouni *et al.*, "Amplification-free detection of SARS-CoV-2 with CRISPR-Cas13a and mobile phone microscopy," *Cell,* vol. 184, no. 2, pp. 323-333. e9, 2021.

[247] T. Yu, S. Zhang, R. Matei, W. Marx, C. L. Beisel, and Q. Wei, "Coupling smartphone and CRISPR–Cas12a for digital and multiplexed nucleic acid detection," *AIChE Journal,* vol. 67, no. 12, p. e17365, 2021.

[248] S. Son *et al.*, "Sensitive and multiplexed RNA detection with Cas13 droplets and kinetic barcoding," *medRxiv,* 2021.

[249] W. Guan, L. Chen, T. D. Rane, and T.-H. Wang, "Droplet digital enzyme-linked oligonucleotide hybridization assay for absolute RNA quantification," *Scientific reports,* vol. 5, no. 1, pp. 1-9, 2015.

[250] T. Tian *et al.*, "An ultralocalized Cas13a assay enables universal and nucleic acid amplification-free single-molecule RNA diagnostics," *ACS nano,* vol. 15, no. 1, pp. 1167-1178, 2020.

[251] R. Hall Sedlak and K. R. Jerome, "The potential advantages of digital PCR for clinical virology diagnostics," *Expert review of molecular diagnostics,* vol. 14, no. 4, pp. 501-507, 2014.

[252] J. Kuypers and K. R. Jerome, "Applications of digital PCR for clinical microbiology," *Journal of clinical microbiology,* vol. 55, no. 6, pp. 1621-1628, 2017.

[253] M. H. Jazayeri, T. Aghaie, A. Avan, A. Vatankhah, and M. R. S. Ghaffari, "Colorimetric detection based on gold nano particles (GNPs): An easy, fast, inexpensive, low-cost and short time method in detection of analytes (protein, DNA, and ion)," *Sensing and bio-sensing research,* vol. 20, pp. 1-8, 2018.

[254] Y.-C. Syu, W.-E. Hsu, and C.-T. Lin, "Field-effect transistor biosensing: Devices and clinical applications," *ECS Journal of Solid State Science and Technology,* vol. 7, no. 7, p. Q3196, 2018.

[255] K. Y. Goud *et al.,* "Electrochemical diagnostics of infectious viral diseases: trends and challenges," *Biosensors and Bioelectronics,* vol. 180, p. 113112, 2021.

[256] F. Katzmeier *et al.,* "A low-cost fluorescence reader for in vitro transcription and nucleic acid detection with Cas13a," *PloS one,* vol. 14, no. 12, p. e0220091, 2019.

[257] L. Zhang, K. Zhang, G. Liu, M. Liu, Y. Liu, and J. Li, "Label-free nanopore proximity bioassay for platelet-derived growth factor detection," *Analytical chemistry,* vol. 87, no. 11, pp. 5677-5682, 2015.

[258] N. Ravi, D. L. Cortade, E. Ng, and S. X. Wang, "Diagnostics for SARS-CoV-2 detection: A comprehensive review of the FDA-EUA COVID-19 testing landscape," *Biosensors and Bioelectronics,* vol. 165, p. 112454, 2020.

[259] J. Qian *et al.,* "A portable CRISPR Cas12a based lateral flow platform for sensitive detection of Staphylococcus aureus with double insurance," *Food Control,* vol. 132, p. 108485, 2022.

[260] K. Yin, X. Ding, Z. Li, M. M. Sfeir, E. Ballesteros, and C. Liu, "Autonomous lab-on-paper for multiplexed, CRISPR-based diagnostics of SARS-CoV-2," *Lab on a Chip,* vol. 21, pp. 2730-2737, 2021.

[261] X. Cheng *et al.,* "CRISPR/Cas12a-Modulated fluorescence resonance energy transfer with nanomaterials for nucleic acid sensing," *Sensors and Actuators B: Chemical,* vol. 331, p. 129458, 2021.

[262] J. F. Bogers, N. F. Berghuis, R. W. Busker, A. van Booma, A. Paauw, and H. C. van Leeuwen, "Bright fluorescent nucleic acid detection with CRISPR-Cas12a and poly (thymine) templated copper nanoparticles," *Biology Methods and Protocols,* vol. 6, no. 1, p. bpaa020, 2021.

[263] X. Fu *et al.,* "Exploring the trans-cleavage activity of CRISPR/Cas12a on gold nanoparticles for stable and sensitive biosensing," *Analytical Chemistry,* vol. 93, no. 11, pp. 4967-4974, 2021.

[264] J.-H. Choi, J. Lim, M. Shin, S.-H. Paek, and J.-W. Choi, "CRISPR-Cas12a-based nucleic acid amplification-free DNA biosensor via Au nanoparticle-assisted metal-enhanced fluorescence and colorimetric analysis," *Nano Letters,* vol. 21, no. 1, pp. 693-699, 2020.

[265] Y. Lee *et al.,* "Fabrication of ultrasensitive electrochemical biosensor for dengue fever viral RNA Based on CRISPR/Cpf1 reaction," *Sensors and Actuators B: Chemical,* vol. 326, p. 128677, 2021.

[266] W. S. Zhang *et al.,* "Reverse Transcription Recombinase Polymerase Amplification Coupled with CRISPR-Cas12a for Facile and Highly Sensitive Colorimetric SARS-CoV-2 Detection," *Analytical chemistry,* vol. 93, no. 8, pp. 4126-4133, 2021.

[267] Q. Meng *et al.*, "Detection of the SARS‐CoV‐2 D614G mutation using engineered Cas12a guide RNA," *Biotechnology Journal*, vol. 16, no. 6, p. 2100040, 2021.
[268] F. Li *et al.*, "An ultrasensitive CRISPR/Cas12a based electrochemical biosensor for Listeria monocytogenes detection," *Biosensors and Bioelectronics*, vol. 179, p. 113073, 2021.
[269] Y. Jiang *et al.*, "Detection of SARS-CoV-2 by CRISPR/Cas12a-Enhanced Colorimetry," *ACS sensors*, vol. 6, no. 3, pp. 1086-1093, 2021.
[270] C. M. Ackerman *et al.*, "Massively multiplexed nucleic acid detection with Cas13," *Nature*, vol. 582, no. 7811, pp. 277-282, 2020.
[271] F. Teng *et al.*, "CDetection: CRISPR-Cas12b-based DNA detection with sub-attomolar sensitivity and single-base specificity," *Genome biology*, vol. 20, no. 1, pp. 1-7, 2019.
[272] A. Ramachandran *et al.*, "Electric field-driven microfluidics for rapid CRISPR-based diagnostics and its application to detection of SARS-CoV-2," *Proceedings of the National Academy of Sciences*, vol. 117, no. 47, pp. 29518-29525, 2020.
[273] J. S. Park, K. Hsieh, L. Chen, A. Kaushik, A. Y. Trick, and T. H. Wang, "Digital CRISPR/Cas‐Assisted assay for rapid and sensitive detection of SARS‐CoV‐2," *Advanced Science*, vol. 8, no. 5, p. 2003564, 2021.
[274] X. Wu *et al.*, "Digital CRISPR-based method for the rapid detection and absolute quantification of nucleic acids," *Biomaterials*, vol. 274, p. 120876, 2021.
[275] M. M. Kaminski *et al.*, "A CRISPR-based assay for the detection of opportunistic infections post-transplantation and for the monitoring of transplant rejection," *Nature biomedical engineering*, vol. 4, no. 6, pp. 601-609, 2020.
[276] A. East-Seletsky *et al.*, "Two distinct RNase activities of CRISPR-C2c2 enable guide-RNA processing and RNA detection," *Nature*, vol. 538, no. 7624, pp. 270-273, 2016.
[277] J.-H. Tsou, Q. Leng, and F. Jiang, "A CRISPR test for detection of circulating nuclei acids," *Translational oncology*, vol. 12, no. 12, pp. 1566-1573, 2019.
[278] O. Mukama *et al.*, "An ultrasensitive and specific point-of-care CRISPR/Cas12 based lateral flow biosensor for the rapid detection of nucleic acids," *Biosensors and Bioelectronics*, vol. 159, p. 112143, 2020.
[279] C. Lucia, P.-B. Federico, and G. C. Alejandra, "An ultrasensitive, rapid, and portable coronavirus SARS-CoV-2 sequence detection method based on CRISPR-Cas12," *bioRxiv*, 2020.
[280] J. Bai *et al.*, "Cas12a-based on-site and rapid nucleic acid detection of African swine fever," *Frontiers in Microbiology*, vol. 10, p. 2830, 2019.
[281] K. Yin, X. Ding, Z. Li, H. Zhao, K. Cooper, and C. Liu, "Dynamic aqueous multiphase reaction system for one-pot CRISPR-Cas12a-based ultrasensitive and quantitative molecular diagnosis," *Analytical chemistry*, vol. 92, no. 12, pp. 8561-8568, 2020.
[282] C. Qian, R. Wang, H. Wu, F. Zhang, J. Wu, and L. Wang, "Uracil-mediated new photospacer-adjacent motif of Cas12a to realize visualized DNA detection at the single-copy level free from contamination," *Analytical chemistry*, vol. 91, no. 17, pp. 11362-11366, 2019.
[283] H. de Puig *et al.*, "Minimally instrumented SHERLOCK (miSHERLOCK) for CRISPR-based point-of-care diagnosis of SARS-CoV-2 and emerging variants," *Science Advances*, vol. 7, no. 32, p. eabh2944, 2021.
[284] Y. Zhang *et al.*, "Sensitive and rapid on-site detection of SARS-CoV-2 using a gold nanoparticle-based high-throughput platform coupled with CRISPR/Cas12-assisted RT-LAMP," *Sensors and Actuators B: Chemical*, vol. 345, p. 130411, 2021.

[285] A. Garcia-Venzor *et al.*, "SARS-CoV-2 Direct Detection Without RNA Isolation With Loop-Mediated Isothermal Amplification (LAMP) and CRISPR-Cas12," *Frontiers in Medicine*, vol. 8, p. 125, 2021.
[286] P. Piot, M. Bartos, P. D. Ghys, N. Walker, and B. Schwartländer, "The global impact of HIV/AIDS," *Nature*, vol. 410, no. 6831, pp. 968-973, 2001.
[287] UNAIDS, "2021 fact sheet," *Global HIV & AIDS statistics*, pp. Available at https://www.unaids.org/en/resources/fact-sheet, 2021.
[288] J. D. Stekler *et al.*, "HIV testing in a high-incidence population: is antibody testing alone good enough?," *Clinical infectious diseases*, vol. 49, no. 3, pp. 444-453, 2009.
[289] J. B. Peter and J. S. Sevall, "Molecular-based methods for quantifying HIV viral load," *AIDS patient care and STDs*, vol. 18, no. 2, pp. 75-79, 2004.
[290] B. R. Cobb, J. E. Vaks, T. Do, and R. A. Vilchez, "Evolution in the sensitivity of quantitative HIV-1 viral load tests," *Journal of clinical virology*, vol. 52, pp. S77-S82, 2011.
[291] M. S. Saag *et al.*, "HIV viral load markers in clinical practice," *Nature medicine*, vol. 2, no. 6, pp. 625-629, 1996.
[292] M. S. De Souza *et al.*, "Impact of nucleic acid testing relative to antigen/antibody combination immunoassay on the detection of acute HIV infection," *Aids*, vol. 29, no. 7, pp. 793-800, 2015.
[293] M. S. Malnati *et al.*, "A universal real-time PCR assay for the quantification of group-M HIV-1 proviral load," *Nature protocols*, vol. 3, no. 7, pp. 1240-1248, 2008.
[294] S. Wang, F. Xu, and U. Demirci, "Advances in developing HIV-1 viral load assays for resource-limited settings," *Biotechnology advances*, vol. 28, no. 6, pp. 770-781, 2010.
[295] E. Guichet *et al.*, "Comparison of different nucleic acid preparation methods to improve specific HIV-1 RNA isolation for viral load testing on dried blood spots," *Journal of virological methods*, vol. 251, pp. 75-79, 2018.
[296] R. Nouri, M. Dong, A. J. Politza, and W. Guan, "Figure of Merit for CRISPR-Based Nucleic Acid-Sensing Systems: Improvement Strategies and Performance Comparison," *ACS sensors*, vol. 7, no. 3, pp. 900-911, 2022.
[297] X. Luo *et al.*, "Digital CRISPR/Cas12b-based platform enabled absolute quantification of viral RNA," *Analytica Chimica Acta*, vol. 1192, p. 339336, 2022.
[298] Z. Yu, L. Xu, W. Lyu, and F. Shen, "Parallel Multistep Digital Analysis SlipChip Demonstrated with the Quantification of Nucleic Acid by Digital LAMP-CRISPR," *Lab on a Chip*, 2022.
[299] X. Wu, C. Chan, S. L. Springs, Y. H. Lee, T. K. Lu, and H. Yu, "A warm-start digital CRISPR/Cas-based method for the quantitative detection of nucleic acids," *Analytica Chimica Acta*, vol. 1196, p. 339494, 2022.
[300] F. X. Liu *et al.*, "Isothermal Background-Free Nucleic Acid Quantification by a One-Pot Cas13a Assay Using Droplet Microfluidics," *Analytical Chemistry*, vol. 94, no. 15, pp. 5883-5892, 2022.
[301] H. Shinoda *et al.*, "Amplification-free RNA detection with CRISPR–Cas13," *Communications biology*, vol. 4, no. 1, pp. 1-7, 2021.
[302] H. Shinoda *et al.*, "Automated amplification-free digital RNA detection platform for rapid and sensitive SARS-CoV-2 diagnosis," *Communications Biology*, vol. 5, no. 1, pp. 1-8, 2022.
[303] M. Z. Khan, I. Amin, A. Hameed, and S. Mansoor, "CRISPR–Cas13a: prospects for plant virus resistance," *Trends in biotechnology*, vol. 36, no. 12, pp. 1207-1210, 2018.
[304] O. O. Abudayyeh *et al.*, "C2c2 is a single-component programmable RNA-guided RNA-targeting CRISPR effector," *Science*, vol. 353, no. 6299, p. aaf5573, 2016.

[305] S. Palmer *et al.*, "New real-time reverse transcriptase-initiated PCR assay with single-copy sensitivity for human immunodeficiency virus type 1 RNA in plasma," *Journal of clinical microbiology*, vol. 41, no. 10, pp. 4531-4536, 2003.

[306] J. P. Ortega, M. Del, R. B. Rojas, and M. J. Somodevilla, "Research issues on k-means algorithm: An experimental trial using matlab," in *CEUR workshop proceedings: semantic web and new technologies*, 2009, pp. 83-96.

[307] T. Ono, T. Ichiki, and H. Noji, "Digital enzyme assay using attoliter droplet array," *Analyst*, vol. 143, no. 20, pp. 4923-4929, 2018.

[308] M. E. Hunter, R. M. Dorazio, J. S. Butterfield, G. Meigs‐Friend, L. G. Nico, and J. A. Ferrante, "Detection limits of quantitative and digital PCR assays and their influence in presence–absence surveys of environmental DNA," *Molecular ecology resources*, vol. 17, no. 2, pp. 221-229, 2017.

[309] C. A. Milbury *et al.*, "Determining lower limits of detection of digital PCR assays for cancer-related gene mutations," *Biomolecular detection and quantification*, vol. 1, no. 1, pp. 8-22, 2014.

[310] M. C. Strain *et al.*, "Highly precise measurement of HIV DNA by droplet digital PCR," *PloS one*, vol. 8, no. 4, p. e55943, 2013.

[311] A. S. Basu, "Digital assays part I: partitioning statistics and digital PCR," *SLAS technology*, vol. 22, no. 4, pp. 369-386, 2017.

VITA
Reza Nouri

Education

- Ph.D. candidate in Electrical Engineering
  The Pennsylvania State University, University Park, Pennsylvania, USA
- Master in Mechanical Engineering
  University of Tehran, Tehran, Iran
- Bachelor in Mechanical Engineering
  Iran University of Science and Technology, Tehran, Iran

Journal Publication(4/13)

1. **Nouri, R**., Jiang, Y., Tang, Z., Lian, X. L., & Guan, W. (2021). Detection of SARS-CoV-2 with Solid-State CRISPR-Cas12a-Assisted Nanopores. Nano letters, 21(19), 8393-8400.
2. **Nouri, R**., & Guan, W. (2021). Nanofluidic charged-coupled devices for controlled DNA transport and separation. Nanotechnology, 32(34), 345501.
3. **Nouri, R**., Tang, Z., Dong, M., Liu, T., Kshirsagar, A., & Guan, W. (2021). CRISPR-based detection of SARS-CoV-2: A review from sample to result. Biosensors and Bioelectronics, 113012.
4. **Nouri, R**., Jiang, Y., Lian, X. L., & Guan, W. (2020). Sequence-specific recognition of HIV-1 DNA with solid-state CRISPR-Cas12a-assisted nanopores (SCAN). ACS sensors, 5(5), 1273-1280.

Conference Presentation (3 of 7)

- Published in IEEE SENSORS Conference 2019, "Calibration-Free Electrical Quantification of Single Molecules Using Nanopore Digital Counting."
- Attended Biomedical Engineering Society Annual Meeting (BMES), 2019. Presented "Calibration-Free Electrical Quantification of Single Molecules Using Nanopore Digital Counting."
- Transducer, 2019. "Microfluidic deformability-activated sorting of single particles."

Award

- University of Tehran partial scholarship for Master of Science in mechanical engineering
- Top 0.8% in Iranian Master of Science Entrance exam among more than 20,000 participants
- IUST full scholarship for Bachelor of Science in mechanical engineering
- Top 0.3% in National Public Universities Entrance exam among more than 400,000 participants